

ABSTRACT

INSTABILITIES OF VOLATILE FILMS AND DROPS

by
Nebojsa Murisic

We report on instabilities during spreading of volatile liquids, with emphasis on the novel instability observed when isopropyl alcohol (IPA) is deposited on a monocrystalline silicon (Si) wafer. This instability is characterized by emission of drops ahead of the expanding front, with each drop followed by smaller, satellite droplets, forming the structures which we nickname “octopi” due to their appearance. A less volatile liquid, or a substrate of larger heat conductivity, suppress this instability. In addition, we examine the spreading of drops of water (DIW)-IPA mixtures on both Si wafers and plain glass slides, and describe the variety of contact line instabilities which appear. We find that the decrease of IPA concentration in mixtures leads to transition from “octopi” to mushroom-like instabilities. Through manipulation of our experimental set up, we also find that the mechanism responsible for these instabilities appears to be mostly insensitive to both the external application of convection to the gas phase, and the doping of the gas phase with vapor in order to create the saturated environment.

In order to better understand the “octopi” instability, we develop a theoretical model for evaporation of a pure liquid drop on a thermally conductive solid substrate. This model includes all relevant physical effects, including evaporation, thermal conductivity in both liquid and solid, (thermocapillary) Marangoni effect, vapor recoil, disjoining pressure, and gravity. The crucial ingredient in this problem is the evaporation model, since it influences both the motion of the drop contact line, and the temperature profiles along the liquid-solid and liquid-gas interfaces. We consider two evaporation models: the equilibrium “lens” model and the non-equilibrium one-sided (NEOS) model. Along with the assumption of equilibrium at the liquid-gas interface,

the “lens” model also assumes that evaporation proceeds in a (vapor) diffusion-limited regime, therefore bringing the focus to the gas phase, where the problem of vapor mass diffusion is to be solved, which invokes analogy with the problem of lens-shaped conductor from electrostatics. On the other hand, NEOS model assumes non-equilibrium at the liquid-gas interface and a reaction-limited regime of evaporation; the liquid and gas phases are decoupled using the one-sided assumption, and hence, the problem is to be solved in the liquid phase only. We use lubrication approximation and derive a single governing equation for the evolution of drop thickness, which includes both models. An experimental procedure is described next, which we use in order to estimate the volatility parameter corresponding to each model. We also describe the numerical code, which we use to solve the governing equation for drop thickness, and show how this equation can be used to predict which evaporation model is more appropriate for a particular physical problem.

Next, we perform linear stability analysis (LSA) of perturbed thin film configuration. We find excellent agreement between our numerical results and LSA predictions. Furthermore, these results indicate that the IPA/Si configuration is the most unstable one, in direct agreement with experimental results. We perform numerical simulations in the simplified 2d geometry (cross section of the drop) for both planar and radial symmetry and show that our theoretical model reproduces the main features of the experiment, namely, the formation of “octopus”-like features ahead of the contact line of an evaporating drop. Finally, we perform quasi-3d numerical simulations of evaporating drops, where stability to azimuthal perturbations of the contact line is examined. We recover the “octopi” instability for IPA/Si configuration, similarly as seen in the experiments.

INSTABILITIES OF VOLATILE FILMS AND DROPS

by
Nebojsa Murisic

A Dissertation
Submitted to the Faculty of
New Jersey Institute of Technology and
Rutgers, The State University of New Jersey – Newark
in Partial Fulfillment of the Requirements for the Degree of
Doctor of Philosophy in Mathematical Sciences

Department of Mathematical Sciences
Department of Mathematics and Computer Science, Rutgers-Newark

May 2008

Copyright © 2008 by Nebojsa Murisic
ALL RIGHTS RESERVED

APPROVAL PAGE

INSTABILITIES OF VOLATILE FILMS AND DROPS

Nebojsa Murisic

Dr. Lou Kondic, Dissertation Advisor
Associate Professor of Mathematical Sciences, NJIT

Date

Dr. Demetrios T. Papageorgiou, Committee Member
Professor of Mathematical Sciences, NJIT

Date

Dr. Michael S. Siegel, Committee Member
Professor of Mathematical Sciences, NJIT

Date

Dr. Pushpendra Singh, Committee Member
Professor of Mechanical Engineering, NJIT

Date

Dr. Yuan N. Young, Committee Member
Assistant Professor of Mathematical Sciences, NJIT

Date

BIOGRAPHICAL SKETCH

Author: Nebojsa Murisic
Degree: Doctor of Philosophy
Date: April 2008
Date of Birth: January 6, 1980
Place of Birth: Subotica, Serbia

Undergraduate and Graduate Education:

- Doctor of Philosophy in Mathematical Sciences,
New Jersey Institute of Technology, Newark, NJ, May 2008
- Bachelor of Science in Electrical Engineering,
Lamar University, Beaumont, TX, May 2003

Major: Applied Mathematics

Presentations and Publications:

- N. Murisic, L. Kondic, “On Modeling Evaporation: Volatile Drops”, (in preparation, *J. Fluid. Mech.*).
- N. Murisic, L. Kondic, “How Do Drops Evaporate?”, (submitted to *Phys. Rev. Lett.*).
- N. Murisic, L. Kondic, “Octopus-shaped Instabilities of Evaporating Drops”, (in press, *Proceedings of the 6th International Congress on Industrial and Applied Mathematics (ICIAM 07), Zurich, Switzerland, July 16-20, 2007*).
- L. Kondic, N. Murisic, “On Modeling Evaporation”, (in press, *Proceedings of the 5th Conference on Applied Mathematics and Scientific Computing (ApplMath 07), Brijuni Islands, Croatia, July 9-13, 2007*).
- N. Murisic, L. Kondic, “Octopus-shaped Instabilities of Evaporating Drops: Experiments and Theory”, poster presentation, *Provost Research Day*, NJIT, Newark, NJ, April 9, 2008.
- N. Murisic, L. Kondic, “How Do Drops Evaporate?”, contributed talk, *60th Annual Meeting of the Division of Fluid Dynamics*, American Physical Society, Salt Lake City, UT, November 18-20, 2007.

- N. Murisic, L. Kondic, Y. Gotkis, “Curiously Shaped Instabilities at the Fronts of Volatile Drops”, video entry, *Gallery of Fluid Motion, 60th Annual Meeting of the Division of Fluid Dynamics*, American Physical Society, Salt Lake City, UT, November 18-20, 2007.
- N. Murisic, L. Kondic, “Octopus-shaped Instabilities of Evaporating Drops: Experiments and Theory”, poster presentation, *SIAM Conference on Mathematics for Industry: Challenges and Frontiers (MI07)*, Philadelphia, PA, October 9, 2007.
- N. Murisic, L. Kondic, “Octopus-shaped Instabilities of Evaporating Drops: Experiments and Theory”, poster presentation, *EUROMECH 490 Workshop: Dynamics and Stability of Thin Liquid Films and Slender Jets*, Imperial College, London, UK, September 19-21, 2007.
- A. Oron, L. Kondic, N. Murisic, “Interfacial Problems with Phase Change”, contributed talk, *Pan-American Advanced Studies Institute on Interfacial Fluid Dynamics: From Theory to Applications (PASI 2007)*, Mar del Plata, Argentina, August 6-17, 2007.
- N. Murisic, L. Kondic, “Octopus-shaped Instabilities of Evaporating Drops: Experiments and Theory”, poster presentation, *Pan-American Advanced Studies Institute on Interfacial Fluid Dynamics: From Theory to Applications (PASI 2007)*, Mar del Plata, Argentina, August 6-17, 2007.
- N. Murisic, L. Kondic, “Octopus-shaped Instabilities of Evaporating Drops”, contributed talk, *6th International Congress on Industrial and Applied Mathematics (ICIAM 07)*, Zurich, Switzerland, July 16-20, 2007.
- N. Murisic, L. Kondic, “Octopus-shaped Instabilities of Evaporating Drops”, poster presentation, *Frontiers in Applied and Computational Mathematics (FACM 2007)*, NJIT, Newark, NJ, May 19-21, 2007.
- N. Murisic, L. Kondic, “Curiously shaped Instabilities at the Fronts of Evaporating Drops”, poster presentation, *Provost Research Day*, NJIT, Newark, NJ, April 2007.
- Y. Gotkis, I. Ivanov, N. Murisic, L. Kondic, “Dynamic Structure Formation at the Fronts of Volatile Liquid Drops”, *Phys. Rev. Lett.*, **93**, 186101, 2006.
- N. Murisic, L. Kondic, Y. Gotkis, “Octopus-shaped Instabilities of Evaporating Droplets”, contributed talk, *59th Annual Meeting of the Division of Fluid Dynamics*, American Physical Society, Tampa, FL, November 19-21, 2007.
- N. Murisic, L. Kondic, “Octopus-shaped Instabilities of Evaporating Drops”, poster presentation, *Frontiers in Applied and Computational Mathematics (FACM 2006)*, NJIT, Newark, NJ, May 19-21, 2006.

- N. Murisic, L. Kondic, “Instabilities of Evaporating Drops”, presentation, *Colloquium Session of the Physics Department*, Universidad Nacional del Centro de la Provincia de Buenos Aires (UNCPBA), Tandil, Argentina, April 22, 2006.
- N. Murisic, L. Kondic, “Instabilities of Volatile Droplets”, poster presentation, *Graduate Student Association (GSA) Research Day*, NJIT, Newark, NJ, February 2006.

*Dedicated to my father, Ljubomir, my mother, Nevenka, and my sister, Bojana
for their endless love and support*

ACKNOWLEDGMENT

Special thanks are due to Dr. Yehiel Gotkis (KLA-Tencor), for bringing the “octopi” problem to our attention, and hence, providing the inspiration and motivation for my research. I also thank him for the experimental results he shared with us, as well as for detailed descriptions of his findings. My advisor and myself are very grateful for the materials and supplies which Dr. Gotkis provided – these were very valuable in allowing us to carry out exciting experiments in our Capstone Laboratory. Most of all, I am thankful for contagious enthusiasm and excitement with which he talked about the “octopi”. I am also grateful to Dr. Javier Diez (UNCPBA), for useful discussions regarding my project, and especially for the helpful advice concerning development of the implemented numerical method. I thank Dr. Pierre Colinet (ULB) for sharing his expertise in intricacies of the evaporation process. In addition, I would like to acknowledge the kindness of Dr. Omar Matar (Imperial College London), Dr. Demetrios Papageorgiou and Dr. Thomas Witelski (Duke), who have helped in ascertaining the next chapter of my career as a researcher; also, I would like to express my gratitude to Dr. Demetrios Papageorgiou, Dr. Michael Siegel, Dr. Pushpendra Singh, and Dr. Yuan Young for their patience when it came down to preparing this thesis, for their probing questions and suggestions. I acknowledge the support by the NSF grant No. 0511514 which provided most of the equipment that we used to carry out our experiments.

I am especially indebted to my advisor, Dr. Lou Kondic, who has been the greatest ally one could hope for. The role he has played for the past 5 years and the gratitude he deserves are impossible to describe in these few lines. He has demonstrated utmost patience as I have modestly tried to mature intellectually. I thank him for his advice and suggestions regarding issues, both scientific and personal; I am grateful for the long discussions regarding the project, for his prompt replies to

my questions, and remedies for my concerns and doubts; I appreciate the late hours, even weekends, which he has been willing to spend at NJIT when I had difficulties with the simulations, or when I was excited to report on my findings; he has taught me how to think like a researcher, and when things appeared bleak and results were disappointing, he has been able to time and time again supply the ‘way out’, always based on lucid arguments which would get me back on the track, and restore the belief in me that “the things have to work out”. I am grateful for the opportunities he has given to me, the conferences he encouraged me to attend, and the talks he helped me prepare, as well as the people he introduced me to – just a mention of his name has always been sufficient to ensure kindest treatment. The interaction with him over the past years has made me realize which path I would like to take in the future, and for this I thank him the most.

There are many people who have made my stay at NJIT overwhelmingly rewarding. I would like to take this opportunity to express my gratitude to the following individuals: to Arnaud Goulet, for 27 Rocco Street, discussions on topics ranging from Scorpions to his recipes for passing the doctoral qualifying exams, his Linux wizardry, and all the encouragement he has given to me during those early days; to Yuriy Mileyko, who sacrificed countless hours of his free time to answer my (also countless) qualifying exam questions – his help has truly been invaluable; to Filippo Posta for his friendship, for all the lunches and ‘snacks’ we have had together over the past 3 years, for humorous remarks which would cut the tension during those long hours we spent making Latex ‘write-ups’ or debugging FORTRAN codes; to Dr. Daljit Ahluwalia, for the letter I received on February 23, 2003, saying that I had been accepted into the PhD. program at NJIT, and invaluable lessons he has given to all of us regarding hard work, dedication, discipline and striving toward success; and to Ms. Susan Sutton and Mrs. Padma Gulati, for their excellent administrative support.

I am glad to have met Jovana Vlajic in that Spring of 2004. Without her support, friendship and love, my journey through the graduate school would not have been possible. I thank her for her care and understanding, for her optimism and kind advice with which she always managed to lift my spirits when the times were tough, for all the carefree moments, filled with joy, and those long strolls along Hoboken's Riverfront in the summer evenings, which we spent in endless discussions, admiring the most incredible view I can imagine – the lights of mid-town Manhattan. We have realized together that New York City is the greatest place to be. I know I will be back soon.

Even though they are “across that lonesome ocean”, the support, encouragement and love which my parents have always bestowed upon me have truly been priceless. I thank them for being my chief teachers, for drawing my attention to mechanics at an early age, encouraging my curiosity toward the nature and its fascinating processes, and for making selfless sacrifices so that I could be where I am now. I thank my sister from the bottom of my heart for her support and her love. Her visits will always remain in my memory as the happiest times; I look forward to seeing her again. I dedicate this thesis to my parents and my sister.

TABLE OF CONTENTS

Chapter	Page
1 INTRODUCTION AND MOTIVATION	1
2 THEORETICAL FORMULATION: MODELING EVAPORATION	5
2.1 Review of Commonly Used Evaporation Models	6
2.2 Mathematical Model	14
2.3 The Two Evaporation Models	18
2.3.1 “Lens” Evaporation Model	19
2.3.2 NEOS Evaporation Model	22
2.4 The Scales	23
2.5 The Lubrication Approximation	27
3 COMPUTATIONAL METHODS FOR EVAPORATIVE FILMS AND DROPS	32
3.1 Numerical Codes for 2d Geometry	33
3.1.1 Spatial Discretization	33
3.1.2 Boundary Conditions	36
3.1.3 Time Discretization	37
3.1.4 Error Control	39
3.1.5 Extension to Cylindrical Geometry	40
3.1.6 Code Validation	41
3.2 Quasi-3d Numerical Code	43
4 EVAPORATIVE DROPS: EXPERIMENTS AND NUMERICAL SIMULA- TIONS	51
4.1 The Experimental Procedure	51
4.2 From Experimental Data to Volatility Coefficients	54
4.3 Numerical Simulations, Comparison with the Experimental Results and Discussion	59
4.3.1 DIW Configurations	60
4.3.2 IPA Configurations	69

TABLE OF CONTENTS
(Continued)

Chapter	Page
5 INSTABILITIES OF EVAPORATING FILMS AND DROPS	79
5.1 Octopus-shaped Instabilities: Initial Experiments	79
5.2 Literature Review	83
5.3 Experiments Carried Out at NJIT	84
5.4 Theory and Computations	93
5.4.1 Linear Stability Analysis	93
5.4.2 Verification of the Linear Stability Analysis Predictions	100
5.4.3 Numerical Simulations for Volatile 2d Planar and Radial Drops	106
5.4.4 Numerical Simulations for Volatile 3d Drops	109
5.4.5 Azimuthal Perturbations of 3d Drops	110
6 CONCLUSIONS AND FUTURE WORK	118
REFERENCES	125

LIST OF TABLES

Table	Page
2.1 Table of Parameter Values for IPA and DIW ([45])	26

LIST OF FIGURES

Figure	Page
2.1	The physical configuration: evaporating drop on a horizontal solid surface. 14
2.2	The spherical cap approximation. 20
3.1	The comparison of numerical results for spreading of 2d planar and radial drops against the Barenblatt solution (Eq. (3.27)). 43
3.2	Spreading of a non-volatile circular drop (numerical results). (a) $t = 0$; (b) $t = 0.3$; (c) $t = 0.7$; (d) $t = 1$. Note that the circular symmetry of the drop is preserved as the spreading proceeds. 47
3.3	Spreading of an initially elliptic drop (numerical results). The initial condition ($t = 0$) is shown in (a); the final state ($t = 0.01$) is shown in (d); the circular symmetry is already achieved at $t = 0.003$ in (b). 48
3.4	Coalescence of non-volatile sessile drops (numerical results). (a) $t = 0$: the initial condition; (b) $t = 0.0033$: the spreading stage; (c) $t = 0.0066$: the configuration during coalescence; (d) $t = 0.01$: after coalescence. 49
4.1	The goniometer: camera, syringe and the deposition platform. 51
4.2	Snapshots of evaporating DIW drop on Si substrate, as recorded by the experimental setup at 56s (top left) , 256s (top right), 440s (bottom left), and 536s (bottom right). 53
4.3	Evolution of volume and radius of a drop of DIW on a Si substrate. 54
4.4	Time variation of volatility coefficients for the DIW/Si and DIW/Cu configurations for the first 106.7s. Stars indicate calculated values, dashed lines indicate corresponding average value. (a) DIW/Si, “lens” model: $\chi = (1.3 \pm 0.2) \cdot 10^{-2}$; (b) DIW/Si, NEOS model: $\alpha = (0.8 \pm 0.1) \cdot 10^{-6}$; (c) DIW/Cu, “lens” model: $\chi = (1.5 \pm 0.4) \cdot 10^{-2}$; (d) DIW/Cu, NEOS model: $\alpha = (0.8 \pm 0.2) \cdot 10^{-6}$ 58
4.5	Comparison of numerical and experimental results for evaporating drop of DIW on Si substrate. “Lens 1” refers to case when λ from [15] is used; “Lens 2” when λ from [33] is used. (a) Evolution of drop volume; (b) Evolution of contact line position. 61

LIST OF FIGURES
(Continued)

Figure	Page	
4.6	Numerical results for evaporating drop of DIW on Si substrate: evolution of drop profile during time interval $[0, 106.7s]$. The initial condition is indicated by a dashed line, while the profile at $t = 106.7s$ is indicated by a full line. (a) “Lens” evaporation model; (b) NEOS evaporation model.	63
4.7	Numerical results for DIW/Si configuration: the temperature of liquid-gas interface at $t = 106.7s$ for “lens” and NEOS evaporation models.	63
4.8	DIW/Si configuration: mass flux J as a function of radial coordinate r at $t = 106.7s$. Full lines represent J , dotted lines represent corresponding drop profile $t = 106.7s$. Note that vertical axes correspond to J only. (a) “Lens” evaporation model; (b) NEOS evaporation model.	64
4.9	Numerical results for DIW/Si configuration: the temperature of liquid-solid interface at $t = 106.7s$. (a) “Lens” evaporation model; (b) NEOS evaporation model.	66
4.10	Influence of convection on experimentally measured evaporation fluxes J^{tot} and evaporation rates J^{rate} for DIW/Si configuration during the time interval $[0, 350s]$. Stars indicate experimental measurements, dashed lines indicate corresponding average values. (a) convection-free: $J^{tot} = 0.4 \pm 0.1g/(m^2s)$; (b) convection-free: $J^{rate} = 5.1 \pm 1.4\mu g/s$; (c) convected: $J^{tot} = 0.7 \pm 0.4g/(m^2s)$; (d) convected: $J^{rate} = 9.5 \pm 5.9\mu g/s$	67
4.11	Numerical results for DIW/Cu configuration using “lens” evaporation model for the time interval $[0, 106.7s]$. (a) Contact line position R and volume V of the drop as functions of time; (b) Evolution of drop thickness; (c) Liquid-gas interface temperature at $t = 106.7s$; (d) Liquid-solid interface temperature at $t = 106.7s$	68
4.12	Comparison of numerical results for evaporating drop of IPA on Si substrate for “lens” and NEOS evaporation model. Time interval: $[0, 106.7s]$. (a) Evolution of drop volume; (b) Evolution of contact line position.	70
4.13	Numerical results for IPA drops: Maximum extent of spreading R_{max} as a function of initial drop volume V_0 . Line “Slope 0.4” corresponds to $R_{max} = 3V_0^{0.4}$	71
4.14	The contact line position R as a function of time for IPA/Si configuration using the two evaporation models. The initial condition is a $7.9\mu l$ hemisphere. $R_{max} = 6.72mm$ is achieved in $27s$ for “lens” model.	72

LIST OF FIGURES
(Continued)

Figure	Page
4.15 IPA/Si: evolution of drop profile during time interval $[0, 106.7s]$. The initial condition is indicated by a dashed line, while the profile at $t = 106.7s$ is indicated by a full line. (a) “Lens” evaporation model; (b) NEOS evaporation model.	72
4.16 IPA/Si: the temperature of liquid-gas interface at $t = 106.7s$ for “lens” and NEOS evaporation model.	73
4.17 IPA/Si: the temperature of liquid-solid interface at $t = 106.7s$. (a) “Lens” evaporation model; (b) NEOS evaporation model.	73
4.18 Volume evolution for IPA/Si configuration with and without Marangoni forces for time interval $[0, 106.7s]$. (a) “Lens” model; (b) NEOS model.	74
4.19 Radius evolution for IPA/Si configuration with and without Marangoni forces for time interval $[0, 106.7s]$. (a) “Lens” model; (b) NEOS model.	75
4.20 IPA/Si: the evolution of the drop thickness for time interval $[0, 10.67s]$ for “lens” evaporation model.	76
4.21 Liquid-gas interface temperature for IPA/Si configuration with and without Marangoni forces. (a) “Lens” evaporation model at $t = 106.7s$; (b) NEOS evaporation model at $t = 86.7s$ (\approx dryout time for NEOS model with $M = 0$).	76
4.22 Numerical results for IPA/Cu configuration using “lens” evaporation model for the time interval $[0, 106.7s]$. (a) Contact line position R and volume V of the drop as functions of time; (b) Evolution of drop thickness; (c) Liquid-gas interface temperature at $t = 106.7s$; (d) Liquid-solid interface temperature at $t = 106.7s$	77
5.1 Formation of “octopi” during spreading of IPA on Si surface ([24]). The bands on the right-hand side are due to Newton interference fringes. White arrows indicate the path of the satellites. On the scale shown ($\approx 200 \times 300 \mu m$) the azimuthal curvature of the (mother) drop is invisible. The insets show uniformity of the “octopi” (top inset) and synchronous pulse-like emission of satellites (bottom inset).	80
5.2 Spreading of 1:1 mix of DIW and IPA ([24]). Drop size is approximately $5mm$. The darker color indicates increased fluid thickness. Time progresses left to right and top to bottom, with the interval between the images $\approx 1.5s$. The bottom row illustrates the merge of individual cells just prior to wave generation (close to image 10). Note formation of radial ridges during early stages of instability development.	81
5.3 The microscope/high-speed camera set-up.	85

LIST OF FIGURES
(Continued)

Figure	Page
5.4	2.5mm x 1.75mm viewing window: spreading of a drop of 70% IPA mixture on a glass slide. 86
5.5	0.6mm x 0.4mm view: three distinct stages in spreading of a drop of 91% IPA mixture on a glass slide. The time progress is shown left to right and top to bottom. 86
5.6	0.6mm x 0.4mm view: the spreading of a drop of pure IPA on a glass slide. The time progress is shown left to right and top to bottom. 88
5.7	2.5mm x 1.75mm viewing window: spreading of a drop of 70% IPA mixture on a glass slide, with externally induced convection in the gas phase. 89
5.8	2.5mm x 1.75mm viewing window: spreading of a drop of 70% IPA mixture on a Si wafer. 90
5.9	0.6mm x 0.4mm viewing window: spreading of a drop of pure IPA mixture on a Si wafer. Notice the “octopus” shaped instabilities similar to the ones in Figure 5.1. 91
5.10	0.6mm x 0.4mm viewing window: spreading of a drop of pure IPA mixture on a Si wafer in an enclosed environment (saturated gas phase). 92
5.11	Growth rates versus k^2 for four considered configurations. 98
5.12	Growth rates versus k^2 for IPA/Si configuration with heated solid for several different values of T_{heater} . The configuration is stable when $T_{heater} = 375K$. As T_{heater} is increased, the transition to unstable regime is achieved. 99
5.13	Time evolution of perturbed thin films for DIW/Cu and DIW/Si configurations. Dashed lines indicate the initial conditions, the full lines indicate the final profile, while dotted lines indicate the film profiles for times between $t = 0$ and the final time t_{final} . (a) DIW/Cu, $k = 0.08$: stable ($t_{final} = 2$); (b) DIW/Cu, $k = 0.63$: stable ($t_{final} = 10^{-3}$); (c) DIW/Si, $k = 0.3 > k_c$: stable ($t_{final} = 2$); (d) DIW/Si, $k = 0.2 < k_c$: unstable ($t_{final} = 1$). 100
5.14	Time evolution of perturbed thin films for IPA/Cu and IPA/Si configurations. Dashed lines indicate the initial conditions, the full lines indicate the final profile, while dotted lines indicate the film profiles for times between $t = 0$ and the final time t_{final} . (a) IPA/Cu, $k = 0.4 > k_c$: stable ($t_{final} = 0.73$); (b) IPA/Cu, $k = 0.3 < k_c$: unstable ($t_{final} = 0.75$); (c) IPA/Si, $k = 0.48 > k_c$: stable ($t_{final} = 0.75$); (d) IPA/Si, $k = 0.38 < k_c$: unstable ($t_{final} = 0.75$). 101

LIST OF FIGURES
(Continued)

Figure	Page	
5.15	Maximum growth rate of perturbation: the comparison of numerical results and LSA prediction for IPA/Si configuration; $k_{max} = 0.297$, $\omega_{max} = 3.148$, $\bar{h} = 1 - \mathcal{W} = 0.85$, and $\delta = 10^{-3}$	102
5.16	The longer-time evolution, thin film ‘rupture’ and subsequent dewetting: IPA/Si thin film configuration disturbed by a small perturbation ($\delta = 10^{-3}$) with $k = k_{max}$; $t_{final} = 30$	103
5.17	Time evolution of perturbed thin films for IPA/Cu and IPA/Si configurations for heated solid case, where $T_{heater} = 415K$. Dashed lines indicate the initial conditions, the full lines indicate the final profile, while dotted lines indicate the film profiles for times between $t = 0$ and the final time t_{final} . (a) IPA/Si, $k = 0.45 > k_c$: stable ($t_{final} = 0.6$); (b) IPA/Si, $k = 0.35 < k_c$: unstable ($t_{final} = 0.75$).	103
5.18	Time evolution of IPA/Si thin film disturbed by perturbation with $k = 0.48 > k_c$. Time evolves left to right, and top to bottom: (a) $t = 0$; (b) $t = 0.15$; (c) $t = 0.3$; (d) $t = 0.45$; (e) $t = 0.6$; (f) $t = 0.75$. The configuration is stable.	104
5.19	Time evolution of IPA/Si thin film disturbed by perturbation with $k = 0.38 < k_c$. Time evolves left to right, and top to bottom: (a) $t = 0$; (b) $t = 0.15$; (c) $t = 0.3$; (d) $t = 0.45$; (e) $t = 0.6$; (f) $t = 0.75$. The configuration is unstable.	105
5.20	Planar drop profiles at $t = 1$ for 4 considered configurations (IC is not shown). Notice the instability which occurs ahead of the contact line for IPA/Si configuration.	106
5.21	IPA/Si: numerical results for a 2d radial drop using “lens” evaporation model. (a) Evolution of drop thickness from $t = 0$ (dashed line) to $t = 5$ (solid line): note stretching of the contact line region; (b) Temperature profile at the liquid-gas interface at $t = 5$: notice the temperature maximum.	107
5.22	IPA/Si: numerical results for a 2d radial drop using NEOS evaporation model. (a) Evolution of drop thickness from $t = 0$ (dashed line) to $t = 0.7$ (solid line): notice the instability which occurs ahead of the contact line and resembles the “octopus”-shaped instability; (b) Temperature profile at the liquid-gas interface at $t = 0.7$	108
5.23	IPA/Si: evolution of a 3d drop using “lens” evaporation model. (a) $t = 0$: the initial condition; (b) $t = 1.5$: the onset of the spreading motion; (c) $t = 3.5$: the stretching of the contact line region is evident; (d) $t = 5$: the final state.	109

LIST OF FIGURES
(Continued)

Figure	Page
5.24 IPA/Si: evolution of a 3d drop using NEOS evaporation model. (a) $t = 0$: the initial condition; (b) $t = 0.1$: receding motion; (c) $t = 0.3$: the ‘ring’ appears; (d) $t = 0.7$: the final state – full blown ‘ring’ ahead of the contact line.	110
5.25 Evolution of azimuthal perturbation for IPA/Si configuration using “lens” model. (a) $t = 0$: the contact line region is perturbed using an azimuthal perturbation with $k = 8$ (2 full wavelengths are visible); (b) $t = 0.1$: the perturbation decays, and is not visible in (c) at $t = 0.3$; (d) $t = 0.5$: the spreading proceeds in a manner similar to that seen in Figure 5.23. The configuration is stable.	111
5.26 IPA/Si configuration using “lens” model: evolution of azimuthal perturbations. (a) $t = 0$: the contact line region is perturbed using an azimuthal perturbation with $k = 12$ (3 full wavelengths are visible), which decays ($t = 0.1$ in (b)), until it is no longer visible at $t = 0.2$ in (c); (d) $t = 0.5$: the spreading proceeds in a manner similar to that seen in Figure 5.23. The configuration is stable.	112
5.27 Evolution of azimuthal perturbation for IPA/Si configuration using “lens” model. (a) $t = 0$: the contact line region is perturbed using an azimuthal perturbation with $k = 64$ (16 full wavelengths are visible); (b) the decay is so rapid that the perturbation is no longer visible at $t = 0.05$. The spreading proceeds in a manner similar to that seen in Figure 5.23 ($t = 0.5$ in (d)). The configuration is stable.	112
5.28 Evolution of azimuthal perturbation for IPA/Si configuration using NEOS model. The contact line region is perturbed at $t = 0$ (a), using an azimuthal perturbation with $k = 8$ (2 full wavelengths are visible in (a)). The drop recedes and the ‘ring’ seen in Figure 5.24 begins to take shape immediately ($t = 0.07$ in (b)); the ‘ring’ rapidly destabilizes and its dissolution into drops ensues ($t = 0.21$ in (c)); eventually, the ‘ring’ collapses into individual drops ($t = 0.7$ in (d)). The configuration is unstable; note the resemblance of the instability to the “octopi” seen in experiments.	113
5.29 Evolution of the azimuthal perturbation for IPA/Si configuration using NEOS model with $M = 0$ (Marangoni forces are neglected). (a) $t = 0$: the contact line region is perturbed using an azimuthal perturbation with $k = 8$ as in Figure 5.28; (b) $t = 0.07$: the drop spreads and the perturbation decays rapidly; (c) $t = 0.21$ and (d) $t = 0.7$: the spreading continues – there is no ‘ring’ ahead of the contact line. The configuration is stable.	114

LIST OF FIGURES
(Continued)

Figure	Page
5.30 Evolution of azimuthal perturbation for IPA/Si configuration using NEOS model. (a) $t = 0$: the contact line region is perturbed with azimuthal perturbation with $k = 12$ (3 full wavelengths are visible); (b) $t = 0.07$: the drop recedes and the ‘ring’ forms; (c) $t = 0.21$: the ‘ring’ destabilizes; (d) $t = 0.7$: finally, the ‘ring’ collapses into individual drops. The configuration is unstable.	116
5.31 Evolution of azimuthal perturbation for IPA/Si configuration using NEOS model. (a) $t = 0$: the contact line region is perturbed with azimuthal perturbation with $k = 64$ (16 full wavelengths are visible); (b) $t = 0.07$: the drop recedes, the perturbation decays, and the ‘ring’ forms; (c) $t = 0.21$: the ‘ring’ becomes larger as the receding motion continues; (d) $t = 0.7$: the ‘ring’ remains intact. The configuration is stable.	116

CHAPTER 1

INTRODUCTION AND MOTIVATION

The instabilities of evaporating drops and thin films have been attracting attention of researchers for quite some time. Lately, the significant rise of interest in this field is primarily a consequence of variety of new applications, for which the use of thin films and drops, and their stability in particular, is critical. Recent developments in semiconductor industry have brought with them a new generation of highly sensitive nano-devices. Volatile thin films and drops have found their way into many processes which are crucial for efficient fabrication and proper operation of these devices ([40, 46]). In particular, drying films and drops play an essential role in processes such as analysis of DNA/RNA microarrays ([6]), fabrication of electronic devices by ink-jet printing technique ([40]), in operation of microlens ([40]), and in immersion lithography ([21, 65]), among others. The stability of evaporating thin films and drops has been studied to a great extent in the past, but there are important issues for which the explanation is still lacking. With the advancement of highly-sensitive new technologies, these issues become ever more significant. It is therefore of great interest to better understand why and under what circumstances these evaporating thin films and drops become unstable. New types of instabilities, with their fascinating appearance and richness of structure have further fueled the interest of scientific community. It is apparent therefore that more complete understanding of the evolution of thin films and drops, including drying, would result in further applications in nano-device fabrication, innovative lab-on-a-chip technology and many other fields.

This project centers on instabilities occurring during the spreading and evaporation of volatile films and drops. In particular, it treats a novel instability which occurs during spreading of isopropyl alcohol (IPA) on monocrystalline silicon (Si)

wafers. This instability is characterized by emission of liquid droplets ahead of the front of deposited drop. Each of these droplets is followed by a cloud of smaller, satellite drops which follow the trail of the initially emitted ones, and form the structures which are given a nickname “octopi” due to their appearance. These structures are experimentally observed only for spreading of IPA on Si, while less volatile liquid, or a substrate characterized by larger heat conductivity suppress this type of instability. Depending on volatility, the configurations in which less volatile mixture is deposited, and allowed to dry upon Si wafer, experience instabilities manifested through appearance of either festoon-like structures, fingers or ridges.

The problems involving volatile drops and/or films have been considered previously by many authors, and variety of mathematical models have been derived. The main difference between these models is the manner in which evaporation process is treated. We argue that without appropriate evaporation model, proper understanding of described instabilities seems unlikely. The focus here is not solely on developing a mathematical model which would govern evolution of volatile drops and films, but also on connection to experiments, such as the one introduced above, and other related ones, which are to be described in this thesis. The important ingredients necessary for achievement of agreement between theory and experiments are hence the careful examination of the experimental set-up and results, which in turn yield correct identification of relevant physical effects and appropriate choice of parameter values. Correct identification of relevant physical effects will ensure the completeness of the mathematical model which is to be derived; the appropriate choice of parameter values will ensure meaningful comparison to experimental results; it will also help in pinning down the physical effects responsible for certain features of the solution, and, provided this whole approach is successful, of particular experimental result. It is therefore expected that the model is to include wide range of physical effects, while the values of parameters to be used are strictly the ones corresponding

to particular liquid/solid configuration and experimental setting. The resulting evolution equations are expected to be highly nonlinear and quite complex, and so, in order to compare to experimental observations, the numerical simulation are used for solving these equations. Linear stability analysis is employed in order to shed light on sensitivity of solution to particular physical effects.

This thesis is organized as follows. First, we examine various evaporation models. We describe several approaches for simplifying this complex problem, and focus on the two commonly used evaporation models: the diffusion-limited equilibrium model and the one-sided non-equilibrium model. Next, we derive a mathematical model, which includes all the relevant physical effects, including vapor recoil, Marangoni effects, Van der Waals intermolecular forces, and thermal effects in two phases (liquid and solid). The derivation of the governing equation for evolution of liquid thickness is carried out in such a way that both evaporation models can be used, and is appropriate for both the volatile drops and films. We proceed by presenting computational methods for solving this governing equation in simplified 2d and 3d geometries. The necessary components for the two evaporation models are volatility parameters, which are estimated experimentally. Thus, we also describe the experimental techniques and methods which we use for this purpose, and present the results. Next, we perform numerical simulations for the two evaporation models and indicate which model is more appropriate in some specific situations. We also examine the influence of Marangoni forces on mobility of the contact line and the rate of mass loss. The next step is the description of the experimental techniques and results related to “octopus”-shaped instabilities. We present both the results obtained by our collaborators from industry, involving mostly pure IPA drops, and our own results for both the pure IPA drops and variety of IPA-water (DIW) mixtures. In particular, we examine the influence of IPA concentration in mixtures on the shape and size of the instabilities. In addition, we study the sensitivity of the

instability mechanism to the externally applied convection in the gas phase, as well as saturation of the gas phase with the vapor. We focus on pure liquids, and proceed by performing linear stability analysis (LSA) of the governing equation for the case of volatile film and comparing these results to the results of numerical simulations. After concluding that the IPA/Si configuration is most unstable, in agreement with the experimental data, we continue by presenting the results of numerical simulations for volatile drops. We first focus on 2d planar and radial geometries and show that our model successfully captures the basic instability mechanism: the occurrence of “octopus”-shaped instabilities ahead of the drop contact line. This is followed by consideration of the quasi-3d problem, where we apply small azimuthal perturbations of the contact line and examine the stability. We show numerical results which again indicate that the IPA/Si configuration is most unstable. Furthermore, the instabilities which we obtain in our numerical results are remarkably similar to “octopi” seen in experiments. We conclude with summary and discussion.

CHAPTER 2

THEORETICAL FORMULATION: MODELING EVAPORATION

The phenomenon of drying liquid films and drops has been engaging scientific minds for centuries. A renewed interest among both scientists and engineers has been evident in past decade, and is largely due to the rapid advances in semiconductor technologies, and micro- and nano-fluidics. Evaporative sessile drops are particularly interesting because of nonuniform drop thickness and the presence of contact lines, which lead to possibility of nonuniform evaporation along the liquid-gas interface. The resulting temperature gradients and related Marangoni forces induce flow inside the drop and lead to a number of interesting effects. These effects are essential in a number of problems, including the so-called coffee-stain phenomenon which involves deposition of solid particles close to a contact line ([14]), and its numerous applications ([6, 40]). In addition, evaporation is crucial for variety of other processes, including coating, fluid transport and cleaning of semiconductor wafer surfaces ([24]). Therefore, the benefits of a thorough understanding of evaporation phenomenon are obvious.

At this stage, the primary focus of our attention is the problem of evaporating drop, although the discussion in this chapter, for most part, applies also to evaporating thin films. We start with a review of various evaporation models used in literature, and describe the complex nature of the evaporation problem. Next, we discuss several different strategies one can use in order to reduce the complexity of the problem. We focus on two commonly used and fairly simple evaporation models: the equilibrium diffusion-limited and the non-equilibrium one-sided model. Finally, we develop a mathematical model based on Navier-Stokes equations and lubrication approximation, which includes all relevant physical effects. The resulting

evolution equation for liquid thickness is derived in such a way that it can include both evaporation models.

2.1 Review of Commonly Used Evaporation Models

The simplicity of the physical system in which a drop of pure liquid placed on a solid surface evaporates is all but obvious. Yet, much is still unclear, and even such seemingly trivial systems as drying water droplets are not well understood. The experimental work has been performed by numerous authors (see e.g [8, 9, 13, 14, 33]). Theoretical models describing the phenomenon of drying drops and thin films have appeared over the years in variety of flavors ([7, 8, 10, 14, 19, 20, 29, 33, 41, 48, 57, 70]). The most important difference among these models is the manner in which evaporation is introduced into the problem. In addition to usual difficulties in describing motion of contact lines, evaporation induces complex interplay between thermal and hydrodynamic effects. It is an endothermic process and as such it inevitably causes cooling of the liquid-gas interface. Evidently, evaporation rate varies locally along this interface ([14]), causing convection of liquid due to thermocapillary effects. In turn, convection alters transport of heat in the liquid and in such a way it affects the evaporation rate ([29]). Using appropriate model for evaporation is therefore the paramount objective if one is to achieve agreement between theory and experiments. In what follows, we discuss commonly used models.

The problem of an evaporating drop involves three phases: solid, liquid and gas. Solving the full problem in all three phases would be much too complex, since it involves the Navier-Stokes equations for both liquid and gas, energy equations for all three phases, along with the equation for vapor mass fraction. In what follows, we refer to the model including ‘full’ treatment of liquid and gas phase as two-sided model. Before reviewing commonly used assumptions under which the two-sided model can be reduced to less complex models, it is worthwhile to dedicate some

thought to the state of the liquid-gas interface and the composition of the gas phase. As it turns out, the manner in which liquid-gas interface and the gas phase itself are treated is critical in determining which simplification path is to be taken.

In thermodynamic sense, the liquid-gas interface can be considered to be either in equilibrium ([8, 9, 14, 15, 19, 26, 28, 29, 31, 33, 34, 48, 61]), or in non-equilibrium ([2, 3, 7, 10, 24, 30, 57, 70]). As far as the composition of the gas phase is concerned, we can either assume that the gas phase is composed of vapor itself ([7, 24, 57]), or a mixture of vapor and inert gas (e.g. air; see: [8, 9, 10, 14, 19, 29, 48, 70]). If we first assume that the drop is in contact with its vapor only (no inert gas), and that the interface is at thermodynamic equilibrium, the temperature and the pressure in the gas are simply related through Clausius-Clapeyron law ([39])

$$\ln \left[\frac{p_{sat}}{p_0} \right] = \frac{DH_{vap}}{R} \left[\frac{1}{T_0} - \frac{1}{T_{sat}} \right], \quad (2.1)$$

where DH_{vap} and R are the enthalpy of vaporization and universal gas constant, and p_{sat} and T_{sat} are saturation pressure and temperature. Further, the dynamic viscosity of vapor is small, making pressure fluctuation in the gas phase limited, and so, temperature fluctuations at the interface are small as well. Therefore, Marangoni effects should not be expected for a drop in contact with its vapor only, unless non-equilibrium is assumed at the interface ([29]). On the other hand, if the gas phase is composed of vapor and inert gas, even though fluctuations of total pressure in the gas are small, the fluctuations of partial pressure of vapor can be relatively large. These large fluctuations, even under equilibrium assumption, may lead to significant temperature fluctuations at the interface, making Marangoni effects possible ([29]). Under non-equilibrium assumption at the interface, the mass flux J can be related to interface quantities (pressure and temperature) through Hertz-Knudsen relation, which has origins in kinetic theory of gases ([10])

$$J = \alpha \sqrt{\frac{M}{2\pi RT_{sat}}} [p_{sat}(T_i) - p_v(T_i)], \quad (2.2)$$

where $p_{sat}(T_i)$ is saturation pressure at the interface temperature T_i , and $p_v(T_i)$ is vapor pressure just beyond the interface. The parameters α , M , and R are the accommodation coefficient, molecular weight of vapor molecule and universal gas constant respectively. Eq. (2.2) assumes continuity of temperature across the interface. To conclude, any model which is to include Marangoni effects must either consider a gas phase consisting of vapor/inert gas mixture (where equilibrium at the liquid-gas interface could be assumed), or it must allow for non-equilibrium, if gas phase is assumed to consist of vapor only.

In order to reduce the complexity of the two-sided model, it is recognized that thermal conductivity of vapor is much smaller than that of liquid ([7, 57, 70]); this, in turn, eliminates the energy equation for gas phase from consideration. We can further simplify, by assuming that the gas phase is convection-free, and that the viscous stresses in gas phase are negligible when compared to viscous stresses in liquid ([7, 48, 57]). As a consequence of these simplifications, the full two-sided model reduces to the system of equations for the liquid phase (Navier-Stokes equations and energy equation), and the equation for diffusion of vapor in the gas phase. Various models which consider the problem in the liquid phase coupled with the vapor diffusion problem in the gas phase are referred to as 1.5-sided models ([19, 29, 48]). We note that the vapor diffusion problem is coupled to the problem in the liquid through boundary conditions at the interface between the two phases.

The 1.5-sided models are still rather complex, and further simplifications are often implemented. One commonly used model, to which from this point on we refer as “lens” model, is formulated as follows. Consider diffusion equation for the vapor mass fraction c , with D being vapor mass diffusivity ([15, 33, 58]), along with appro-

appropriate boundary conditions. Scaling of the vapor mass diffusion problem is achieved using an appropriate time-scale, t_{scale} , and a length-scale, such as the extent of the gas phase l . For $t_{scale} \gg t_{diff-vap}$, where $t_{diff-vap} = l^2/D$ is vapor diffusion time-scale, the transient term in the diffusion equation for the vapor mass fraction can be dropped and the problem reduces to the Laplace's equation: $\Delta c = 0$. The typical value of D for diffusion of water vapor into the air is $2.5 \cdot 10^{-5} m^2/s$. Using $d_0 = 0.5 mm$ as a typical drop thickness and assuming that $l \sim d_0$, yields $t_{diff-vap} \sim O(10^{-2})s$. For the sake of comparison, a time-scale on which microliter water drops evaporate is $\sim O(10^3)s$. This indicates that, except in the case of a very thick gas phase, the reduction of diffusion equation for vapor mass fraction to Laplace's equation is plausible. Physical interpretation of this mathematical simplification is that the evaporation rapidly attains steady state and that the vapor mass fraction field adjusts quickly to the changes of the shape of the liquid-gas interface ([33, 58]). We note that an 'evaporation time-scale' introduced in [58], corresponding to time-scale for molecular transport across liquid-gas interface, is much shorter ($\sim 10^{-10}s$). Based on the comparison of this short evaporation time-scale and previously introduced vapor mass diffusion time-scale, it is concluded in [58] that the evaporation process is limited by mass diffusion of vapor. Under certain assumptions, discussed in Section 2.3, this approach leads to the evaporative flux of from $J \sim h^{-\psi}$, where h is drop thickness, and the value of exponent ψ depends on the macroscopic contact angle Θ . We note that J diverges at the contact line ($h \rightarrow 0$). The analogy between evaporating drop and lens-shaped conductor at a fixed potential has been suggested in [14, 15]. In their work, they considered volatile drops of water with pinned contact line, and focused on solute deposition patterns (the coffee-stain problem). In [33], it is shown how mass flux J , associated evaporation rate, and the expression for ψ can be found from numerically calculated vapor mass fraction field. In particular, the dependence of ψ on contact angle Θ is resolved by fitting the approximate expression for mass flux J (obtained

through considering the “lens” problem) to their numerical solution for J . This work was accompanied by subsequent resolution of the hydrodynamic flow inside the drop ([34]), inclusion of thermocapillary Marangoni effects and resolution of temperature fields in both the liquid and the solid phase ([31]), and further experimental results ([32]). The “lens” evaporation model was subsequently extended to problems where contact line is allowed to move freely. These problems involved volatile drops of water, alkanes, PDMS oligomers and their mixtures on variety of surfaces on which the complete wetting can be assumed ([8, 9, 25, 26, 27, 28, 59, 60, 61]). A regularization procedure was employed in [26, 28] in order to relieve the singularity in the mass flux which occurs at the contact line. The work presented in [13, 15] was further extended to a problem involving solute deposition patterns for water drops and the peculiarities of de-pinning process ([58]). Water drops evaporating on a heated solid, the resulting temperature gradients and flow along the liquid-gas interface were examined in [22]. Finally, the recent work by [64] focuses on a wedge-shaped region in the close proximity of the contact line. It involves the application of the “lens” evaporation model and the use of asymptotic techniques in order to show how thermal properties of solid and liquid, and the value of macroscopic contact angle qualitatively influence the temperature gradient at the liquid-gas interface, and hence the direction of liquid flow.

Another approach to simplify the model is to decouple the gas and the liquid phase, and consider the liquid phase only. If it is assumed that the gas phase is comprised of vapor only, it is necessary to consider the interface at non-equilibrium, in order to maintain the possibility of thermocapillary Marangoni effects at the liquid-gas interface (e.g. see [2, 7, 57]). The decoupling is achieved formally by recognizing that thermal conductivity, dynamic viscosity and density of vapor are small when compared to their liquid counterparts. Such approach is generally referred to in the literature as the one-sided model ([7, 10]). If the gas phase is a mixture of vapor and

inert gas, the decoupling is achieved through assumption that vapor mass diffusion time-scale is much shorter than evaporation time-scale. This non-equilibrium one-sided model (NEOS) has been successfully used in theoretical exploration of stability of volatile thin films on heated solid substrates ([7]), and has since been extended to variety of problems. Perhaps the most comprehensive account of the applications of NEOS model has been compiled in [57], where NEOS model has been applied to evaporation of thin films on non-heated and differentially heated solid substrates, to coating flows of volatile films on cylindrically shaped objects, and problems in which physical parameters including viscosity of liquid may be temperature dependent, among others. The NEOS model has also been used for modeling evaporation of drops: in [3, 30], where the focus was on examining the effects of evaporation on macroscopic contact angle; in [2], where disjoining pressure effects were used in order to derive the thickness of stable adsorbed film, beyond which the liquid does not evaporate. We have previously utilized it for studying curiously-shaped instabilities appearing at the fronts of alcohol drops ([24]). More recently, an extension of work by [7] to a problem of stability of volatile thin films can be found in [69], where additional effect of energy transport within the liquid-gas interface is considered and the details of film rupture are examined. One-sided approach was used in [51] as well, where the focus was on studying stationary meniscus of a volatile perfectly wetting system, which, when temperature difference is applied, assumes non-zero apparent contact angle. Under certain assumptions, discussed in Section 2.3, the use of NEOS model leads to the evaporative flux of from $J \sim 1/(h + \text{const.})$. We note that in this case J is bounded at the contact line ($h \rightarrow 0$), in contrast to the expression for J which corresponds to “lens” model.

The one-sided model in general introduces a Biot number, characterizing the evaporation regime ([10]). For 1.5-sided model, non-local ‘modified’ Biot number Bi can be defined ([48]). In case when vapor mass fraction field can be considered quasi-

stationary, non-local contribution to Bi can be neglected, and reduction to one-sided model is achieved. In a particular case when NEOS model is assumed to be valid, the Biot number is defined as

$$Bi = \frac{K p_T L d_0}{\rho_v k}, \quad (2.3)$$

where $K = \alpha \rho_v (T_i) / \sqrt{2\pi R_g T_{sat}}$ and $p_T = L p_{sat} / (R_g T_{sat}^2)$. Here, L is latent heat of vaporization, d_0 is liquid thickness, ρ_v is vapor density and k is liquid heat conductivity. The limit $Bi \rightarrow 0$ implies that liquid-gas interface temperature tends to the temperature of the solid substrate, since the liquid heat conduction is rapid and it replenishes quickly the heat lost at the interface. The evaporation proceeds in a reaction-limited regime, while the liquid-gas interface is at non-equilibrium. On the other hand, the limit $Bi \rightarrow \infty$ indicates that the evaporation process is much quicker than diffusion of heat through the liquid, and hence it leads to a (liquid heat) diffusion-limited regime, while the liquid-gas interface is at equilibrium. Among other quantities, Bi depends on the accommodation coefficient α , which describes probability of phase change, and hence determines the volatility of liquid. Unfortunately, the value of α is not well known. Review of literature reveals that the values of α in the range $O(10^{-6}) - O(1)$ have been used ([7, 10, 24, 29, 39, 57, 67, 70]). Theoretical predictions suggest that $\alpha \in [10^{-2}, 1]$ for water ([47]). However, these estimates have been found to grossly overestimate the volatility, and have repeatedly failed to agree with experimental measurements. In fact, values of α as small as 10^{-6} have been experimentally measured (e.g., see [5, 16, 47]). Vulnerability of water, in particular, to unintentional contamination by surfactants has been identified as one of the main reasons for such mismatch between theory and experiments ([16]). We note that the range $[10^{-6}, 1]$ for α allows for a transition between $Bi \gg 1$ ((liquid heat) diffusion-limited regime, and interface at equilibrium) and $Bi \ll 1$ (reaction-limited regime, and interface at

non-equilibrium). For example, for $\alpha = 10^{-6}$, $p_{sat} = 3.2MPa$ ([45]), and $T_i = 295K$ ([24]), we find $Bi = 0.025 \ll 1$. We note that one can also consider Bi as the ratio of the heat diffusion time-scale in the liquid, $t_{diff-liq}$, to the evaporation time-scale t_{eva} . Using $t_{diff-liq} = d_0^2/\kappa$, where $\kappa = k/(\rho c_p)$ is thermal diffusivity of liquid, and c_p its heat capacity, we find that $t_{diff-liq} \approx 2s$ for water ($c_p = 4180J/(kgK)$). Using this value of $t_{diff-liq}$ and $Bi = 0.025$, we obtain $t_{eva} \approx 70s$. The definition of evaporation time-scale from [24], $t_{eva} = (\rho d_0 2L)/(k\Delta T)$, where ΔT is appropriate temperature scale, gives a consistent value of $t_{eva} \approx 30s$ for (more volatile) isopropyl alcohol.

Next, let us compare t_{eva} , $t_{diff-liq}$, and $t_{diff-vap}$. As mentioned above, for $l \sim d_0$, $t_{diff-vap} \approx 2.5 \cdot 10^{-2}s$, which is significantly shorter than $t_{diff-liq}$, and even more importantly, much shorter than t_{eva} . Therefore, it is safe to conclude that in this case, vapor is indeed diffused rapidly away from the liquid-gas interface and that we can safely neglect the gas phase and use the NEOS model.

On the other hand, if we assume that relevant l is much larger, e.g. $l = 2.5cm$, $t_{diff-vap} \approx 60s$, which is comparable to t_{eva} . At this point, the evaporation rate is clearly being influenced by mass diffusion of vapor, and the use of NEOS model is not appropriate.

The arguments given above, show that the choice of relevant thickness of the gas phase is an important factor in determining the evaporation regime. Unfortunately, for volatile systems which evaporate in open atmosphere, it is not easy to determine the relevant thickness of the gas phase.

Before proceeding further, we note that the comparison of the t_{eva} , $t_{diff-liq}$, and $t_{diff-vap}$ may be used to establish that “lens” evaporation model implies equilibrium at the interface. If we assume that the thermal properties of the liquid are fixed (i.e. $t_{diff-liq} \approx 2s$) while $Bi \gg 1$ (e.g. $Bi \approx 800$ as in [10]), we obtain $t_{eva} \approx 2 \cdot 10^{-3}s$, and the interface is at equilibrium. Since this t_{eva} is significantly smaller than $t_{diff-vap}$ for any reasonable l , evaporation is also limited by mass diffusion of vapor, which is

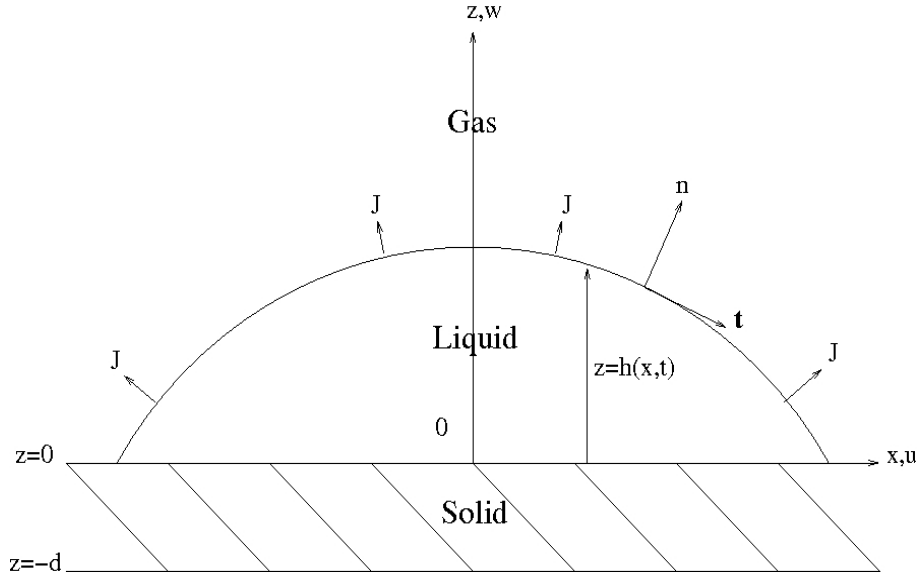


Figure 2.1 The physical configuration: evaporating drop on a horizontal solid surface.

typical for “lens” evaporation model. Therefore, we conclude that the interface in “lens” evaporation model is expected to be at equilibrium.

To summarize, the choice of relevant model for evaporation depends on the values of quantities that cannot be estimated precisely, such as the relevant gas phase thickness, l , or for which a range of results exists, such as the accommodation coefficient α . Chapter 4 concentrates on comparison between two relevant models (“lens” and NEOS) by using parameters extracted directly from experiments. To the best of our knowledge, such a comparison has not been carried out yet. We proceed by developing the mathematical model, in which the critical ingredient, evaporative flux, is left undetermined, so that this approach is appropriate for both evaporation models.

2.2 Mathematical Model

The main building blocks of the model are as follows ([24]): (i) The spreading drop is characterized by a small aspect ratio so that lubrication approximation is appropriate; (ii) Marangoni forces, so that the dependence of surface tension on temperature is included; (iii) Thermal and vapor recoil effects are included ([7, 57]); (iv) the solid-liquid

interaction is modeled using disjoining pressure approach. A large body of literature discussed the details of relevant microscopic physics in the vicinity of the contact line ([12, 35]). Here, we choose a simple model with both attractive and repulsive terms which are often considered to result from van der Waals (vdW) intermolecular forces, leading to a stable equilibrium liquid layer (precursor film).

Our theoretical model is based on Navier-Stokes equations, accompanied by the energy equations, and in general, by the equation for diffusion of vapor into surrounding gas. We derive the model in simplified geometry (2d Cartesian), but later generalize the final equation to radial geometry, as well as quasi-3d geometry. Figure 2.1 shows physical setup with $h(x, t)$ as drop thickness, and x, z as the coordinates along, and normal to the substrate, respectively. The bottom of the solid layer is at $z = -d$, the liquid-solid interface is at $z = 0$, while the liquid-gas interface is at $z = h(x, t)$. Here, $\mathbf{n} = (1 + h_x^2)^{-1/2}(-h_x, 1)$ and $\mathbf{t} = (1 + h_x^2)^{-1/2}(1, h_x)$ are the outward unit normal and unit tangent vectors, respectively.

The Navier-Stokes equations for an incompressible viscous fluid subject to a body force $\nabla\phi$ are given as ([7])

$$\rho(\mathbf{v}_t + \mathbf{v} \cdot \nabla \mathbf{v}) = -\nabla p - \nabla \phi + \mu \nabla^2 \mathbf{v}, \quad (2.4)$$

where p is pressure in the liquid, and $\mathbf{v} = (u, w)$ is the liquid velocity vector, with x - and z - direction components given by u and w respectively. Here, ρ is liquid density, while μ is dynamic viscosity, and $\phi(h)$ is a potential function, which represents gravity and disjoining pressure effects. We note that the latter can instead be included into the normal stress boundary condition at liquid-gas interface (e.g. see [2]). The continuity equation is

$$\nabla \cdot \mathbf{v} = 0. \quad (2.5)$$

Navier-Stokes equations are accompanied by the energy equation for the liquid

$$T_t + \mathbf{v} \cdot \nabla T = \kappa \nabla^2 T, \quad (2.6)$$

where T is liquid temperature. The energy equation for the solid is given as

$$[T_s]_t = \kappa_s \nabla^2 [T_s], \quad (2.7)$$

where T_s denotes solid temperature and κ_s is solid heat diffusivity. Appropriately modified Navier-Stokes equations, continuity, and energy equations hold for the gas layer, in addition to an equation for vapor mass fraction.

Next, we introduce boundary conditions. The temperature at the bottom of the solid layer is prescribed as $T_s(-d, t) = T_0$, where T_0 is the reference (room) temperature. At the liquid-solid boundary ($z = 0$) we assume no-slip and no-penetration boundary condition: $\mathbf{v} = 0$, along with continuity of temperature and matching heat fluxes between the liquid and the solid: $T(0, t) = T_s(0, t)$ and $-kT_z(0, t) = -k_s [T_s]_z(0, t)$.

More care is required when treating the boundary conditions at the liquid-gas interface $z = h(x, t)$. The mass balance gives

$$J = \rho(\mathbf{v} - \mathbf{v}_i) \cdot \mathbf{n} = \rho_v(\mathbf{v}_v - \mathbf{v}_i) \cdot \mathbf{n}, \quad (2.8)$$

where ρ_v and \mathbf{v}_v correspond to vapor, \mathbf{v}_i is the interface velocity, and $J = J(x, t)$ is the mass flux. The energy balance gives

$$\begin{aligned} k \nabla T \cdot \mathbf{n} - k_v \nabla T_v \cdot \mathbf{n} + 2\mu(\mathbf{v} - \mathbf{v}_i) \cdot (\boldsymbol{\tau} \cdot \mathbf{n}) - 2\mu_v(\mathbf{v}_v - \mathbf{v}_i) \cdot (\boldsymbol{\tau}_v \cdot \mathbf{n}) = \\ -J \left(L + \frac{1}{2} [(\mathbf{v}_v - \mathbf{v}_i) \cdot \mathbf{n}]^2 - \frac{1}{2} [(\mathbf{v} - \mathbf{v}_i) \cdot \mathbf{n}]^2 \right), \end{aligned} \quad (2.9)$$

where τ is the rate of deformation tensor in the liquid

$$\tau = \begin{vmatrix} u_x & \frac{1}{2}(u_z + w_x) \\ \frac{1}{2}(u_z + w_x) & -u_x \end{vmatrix}.$$

Eq. (2.9) states that the energy available at the interface is used for phase transition and impinging kinetic energy to the vapor molecules. The normal stress balance is given by

$$(\nabla \cdot \mathbf{n}) \sigma(T) + (\mathbf{T} - \mathbf{T}_v) \cdot \mathbf{n} \cdot \mathbf{n} = J(\mathbf{v} - \mathbf{v}_v) \cdot \mathbf{n}, \quad (2.10)$$

where $\mathbf{T} = -p\mathbf{I} + 2\mu\tau$ is the stress tensor in the liquid, and \mathbf{I} is the identity tensor. The first term on the left-hand side of Eq. (2.10) is proportional to the product of surface tension, σ , and the mean curvature, while the remaining terms represent the jump in normal stress. The sole term on the right-hand side of Eq. (2.10) represents the vapor recoil effect. The shear stress balance gives

$$-\nabla\sigma \cdot \mathbf{t} + (\mathbf{T} - \mathbf{T}_v) \cdot \mathbf{n} \cdot \mathbf{t} = J(\mathbf{v} - \mathbf{v}_v) \cdot \mathbf{t}. \quad (2.11)$$

Eq. (2.11) balances the jump in shear stress with the surface tension gradient. We assume that surface tension is a function of the liquid temperature $\sigma(T) = \sigma_0 - \gamma(T - T_0)$, and note that $\gamma = -d\sigma/dT$ is positive for most liquids.

In order to close the system, we need one more boundary condition at the liquid-gas interface. Depending on the equilibrium state of the liquid-gas interface and the assumptions about the gas phase, as discussed in Introduction, we consider two possible closures for the system. These depend on considered evaporative flux model, discussed next. The assumption that ‘‘lens’’ model is appropriate (evaporation proceeds in a vapor mass diffusion-limited regime with interface at equilibrium)

requires consideration of vapor mass fraction problem in the gas phase, and leads to an expression for mass flux J in terms of drop thickness h ($J \sim h^{-\psi}$). If, on the other hand, we assume that NEOS model is applicable, we neglect the gas phase and obtain additional boundary condition which relates mass flux J and temperature of the liquid-gas interface T_i , and allows to close the system. The details behind derivation of both the expression for J (“lens” model) and the additional boundary condition (NEOS model) are described next.

2.3 The Two Evaporation Models

In previous sections, we described the physical reasoning behind the theoretical model for evaporating drop and the most important steps in the process of deriving the governing system of equations. As it was described in the Introduction, the two most commonly used evaporation models are, in fact, mutually exclusive. In [20], the dependence of evaporation regime on the environment (e.g., drop surrounded by liquid bath, or covered by a lid with an opening above the top of the drop) for water drops was studied. It was argued that depending on evaporation regime, either “lens” or NEOS evaporation model can be used, which was supported solely by the results of extensive numerical simulations. Unfortunately, the technical challenges of non-invasive measurements of vapor concentration in the vicinity of the liquid-gas interface are difficult to overcome. Therefore, a governing equation for the evolution of the drop thickness is derived and used as a test bed for validity checks of the two evaporation models against the experimental results. We devote following paragraphs to details behind these two evaporation models and the manner in which they are to be included into governing system of equations (Eqs. (2.4)-(2.11)).

2.3.1 “Lens” Evaporation Model

It has been discussed in Introduction that the “lens” model is consistent with the liquid-gas interface being at equilibrium, while the evaporation process is limited by diffusion of vapor into surrounding gas. The problem for vapor mass diffusion is reduced to the Laplace’s equation for vapor mass fraction c , accompanied by the boundary condition at the liquid-vapor interface (constant saturation concentration at the evaporating interface) and some far-field condition for concentration, such as ambient concentration. If the drop is assumed to be a spherical cap, this boundary value problem has an electrostatic equivalent: the problem of finding an electric field exterior to a lens-shaped conductor at a fixed potential, where vapor mass fraction c is equivalent to electrostatic potential, while mass flux J is equivalent to electric field ([14]). Additional requirement, necessary in order to successfully map the evaporation problem to the electrostatic problem, is that there should be no evaporation beyond the contact line of the drop. Solving this electrostatic problem analytically involves the use of toroidal coordinates and special functions ([15, 58]), and the resulting expression for electric field (and hence mass flux J) is fairly complex ([33]), but can be well approximated by

$$J(r) \propto \frac{1}{(R^2 - r^2)^\lambda}, \quad (2.12)$$

where R is the radius of the drop, and $r = \sqrt{x^2 + y^2}$ is the radial distance from the drop center. Regarding the exponent λ , [15] gives λ as $\lambda = (\pi - 2\Theta) / (2\pi - 2\Theta)$ (see also [36]). On the other hand, in [33], the validity of the expression for λ from [15] is disputed; their claim is that the λ given in [15], would be correct only if J were given as $J(r) = \text{const.}/(R - r)^\lambda$. The alternate expression for λ which would correspond to the exponent in Eq. (2.12) is derived in [33] in a following fashion: i) it is assumed that the approximation for J in a form of Eq. (2.12) holds; ii) the problem of solving for

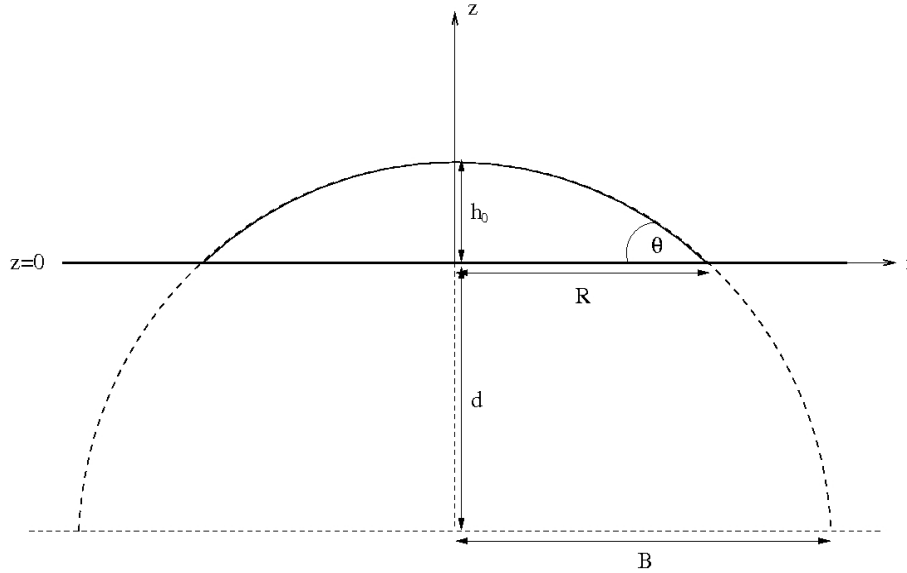


Figure 2.2 The spherical cap approximation.

vapor mass fraction field in the gas phase, exterior to the drop, consists of Laplace's equation for vapor mass fraction c , and the appropriate boundary conditions; iii) the problem in ii) is solved numerically using finite element methods, keeping in mind that the drop surface (the boundary of the problem domain) changes shape as the drop evaporates; iv) once the vapor mass fraction field is resolved numerically, the relation $J = D\nabla c$, valid at the liquid-gas interface, is used to find J ; v) in order to find λ , the expression for J given in Eq. (2.12) is fitted to the numerical solution. The resulting expression for λ as a function of the contact angle Θ is given by $\lambda = 1/2 - \pi/\Theta$. When complete wetting is considered ($\Theta = 0$), the two expressions for λ are equivalent. We note that the numerical results in [33] depend on the choice of relevant thickness of gas phase l . We have shown in Introduction how this choice can affect the regime in which evaporation proceeds. It is therefore possible that the use of different value of l may result in different expression for λ than the one listed in [33]. Unable to decide whether the expression for λ from [15], or the expression from [33] is more appropriate, we will use both.

In what follows, we assume that the surface of the drop is well approximated by a spherical cap, as shown in Figure 2.2, so that we can write the thickness of the drop h in terms of r as $h = \sqrt{R^2 + d^2 - r^2} - d$, where $d = (R^2 - h_0^2) / (2h_0)$ and h_0 is the thickness at the center of the drop ($r = 0$); also note that $B = d + h_0$. In view of lubrication approximation (see Section 2.5), we assume that $h_0/R \ll 1$. In order to simplify the derivation, R and h_0 are treated as constants. This can be justified in part by the fact that the evaporation process, and therefore the changes in drop's shape, are slow.

Next, the Eq. (2.12) is scaled, using $J_{sc} = (k\Delta T)/(d_0L)$ (the value of mass flux for linear temperature profile across flat liquid layer ([7, 57])) and d_0 as scales for mass flux and length respectively. We note that $\Delta T = T_0 - T_{sat}$, where T_{sat} is the saturation temperature at a given vapor pressure. Upon substituting the expression for r in terms of h , we obtain the following expression for mass flux J , now as a function of drop thickness h

$$J(h) = \frac{J_{vol}}{d_0^{2\lambda} (h ((R/d_0)^2 - 1 + h))^\lambda}, \quad (2.13)$$

where J_{vol} is an evaporation coefficient. For small values of contact angle Θ , the dominant term in brackets of Eq. (2.13) is $(R/d_0)^2$, and so Eq. (2.13) reduces to

$$J(h) = \frac{\chi}{h^\psi}, \quad (2.14)$$

where $\psi = \lambda$. For larger values of contact angle Θ ($R \sim d_0$), the dominant term in brackets of Eq. (2.13) becomes h . The expression for J given by Eq. (2.14) is still valid in this case, but with $\psi = 2\lambda$. The dimensionless volatility parameter χ is defined as $\chi = J_{exp}/(d_0^\psi J_{sc})$, where $J_{exp} = J_{vol}/d_0^{2\lambda}$ will be determined experimentally.

Finally, we note that in Eq. (2.14) J diverges as $h \rightarrow 0$. While it is clear that the evaporation rate at the contact line, where h is small, should be larger than at the top of the drop ([13, 14, 15]), this divergence is non-physical. Methods to regularize the expression for mass flux J were suggested by [28] and [66]. We overcome this difficulty by considering a disjoining pressure model, which describes long-range intermolecular (vdW) forces in the liquid, and introduces a thin precursor film of thickness b . This approach regularizes the expression for J , since at small film thicknesses evaporation stops due to attracting vdW forces (see Chapter 4).

2.3.2 NEOS Evaporation Model

The foundations of NEOS evaporation model have been described in Introduction. This model corresponds to a limit of small Biot number Bi – reaction-limited evaporation, interface at non-equilibrium. Decoupling of liquid and gas phase allows to solve the problem in the liquid phase only and ignore the vapor. Since the liquid-gas interface is assumed to be at non-equilibrium, mass flux J satisfies Hertz-Knudsen type relation (Eq. (2.2)). Clausius-Clapeyron law (Eq. (2.1)) can be used to relate temperature and pressure at the interface, and this provides us with the required boundary condition at the liquid-gas interface, necessary to close the system. This boundary condition is an expression for mass flux J in terms of temperature at the liquid-gas interface T_i

$$J = (T_i - T_{sat}) \left(\frac{\alpha \rho_v L}{T_{sat}^{\frac{3}{2}}} \right) (2\pi R_g)^{-\frac{1}{2}}. \quad (2.15)$$

Next, the Eq. (2.15) is scaled, using J_{sc} as scale for mass flux; the temperature difference $T - T_{sat}$ is scaled against ΔT (see Section 2.4). Finally, we obtain a boundary condition

$$J = \frac{T}{\mathcal{K}}, \quad (2.16)$$

which relates mass flux and liquid temperature at the the liquid-gas interface ($z = h$). The non-equilibrium parameter \mathcal{K} is given by

$$\mathcal{K} = \frac{(2\pi R_g)^{1/2} k T_{sat}^{3/2}}{\alpha d_0 \rho_v L^2}. \quad (2.17)$$

Note that under ideal gas assumption, parameter \mathcal{K} relates to Biot number Bi , given by Eq. (2.3), as $\mathcal{K} = 1/Bi$. Under certain set of assumption (discussed in Sections 2.4 and 2.5), Eq. (2.16) leads to an expression for mass flux J as a function of drop thickness h of form $J \propto 1/(h + \mathcal{K} + const.)$. Hence, mass flux J is largest close to the contact line and smallest at the top of the drop, but unlike J given by Eq. (2.14) it remains finite as $h \rightarrow 0$. The values of α for water listed by various authors vary across several orders of magnitude: from $\alpha = 1$ in [67] and [70], $\alpha = 0.83$ in [7], and $\alpha = 0.1$ ([10]), to experimental measurements of $\alpha = 10^{-6} - 10^{-4}$ ([5, 16, 47]). The theoretical predictions for α have been found to overestimate the volatility. This particularly applies to water, due to its vulnerability to contamination by surfactants. Since it is unclear which value to use, we carry out experiments to determine the appropriate value of α . These experiments are discussed in Chapter 4.

2.4 The Scales

At this point, it is convenient to introduce the scales and nondimensionalize the equations and the boundary conditions described in Section 2.2. Scaling has already been applied in Section 2.3 in order to obtain Eqs. (2.14) and (2.16). The choice of scales is as follows (all parameters are for liquid unless otherwise noted, e.g., see [24]): the length-scale is typical drop thickness, $d_0 = 0.5mm$; d_0^2/ν , ν/d_0 , and $\rho\nu^2/d_0^2$ are

viscous scales for time, velocity, and pressure respectively; the scale for ϕ is $\rho\nu^2/d_0^2$; the temperature and the mass flux scales have been introduced above.

For most liquids and vapors, it is safe to assume that thermal conductivity, dynamic viscosity and density of vapor are small when compared to their liquid counterparts ([7, 10]). Hence we apply limits $\rho_v/\rho \rightarrow 0$, $\mu_v/\mu \rightarrow 0$, and $k_v/k \rightarrow 0$ to Eqs. (2.4) - (2.11). The application of these limits results in elimination of Navier-Stokes and energy equations for gas phase and simplification of boundary conditions given by Eqs. (2.8) - (2.11). For “lens” evaporation model, the system is reduced to the liquid problem coupled with the vapor mass fraction problem. For NEOS evaporation model, the system is reduced to a single fluid problem (only liquid).

In addition, we assume that there is no slip at the liquid-gas interface, leading to: $(\mathbf{v} - \mathbf{v}_v) \cdot \mathbf{t} = 0$. Note that ρ_v is retained in Eq. (2.8), where it multiplies \mathbf{v}_v , which can be large. This is done in the spirit similar to Boussinesq approximation ([7]). In addition, it is assumed that $p_v = 0$, and that $\nabla T_v \cdot \mathbf{n}$, $\tau \cdot \mathbf{n} \cdot \mathbf{n}$, and $\tau_v \cdot \mathbf{n} \cdot \mathbf{n}$ are all bounded.

Finally, Eqs. (2.4) - (2.7) are reduced to (in component form)

$$u_t + uu_x + wu_z = -(p_x + \phi_x) + u_{xx} + u_{zz} \quad (2.18)$$

$$w_t + ww_x + ww_z = -p_z + w_{xx} + w_{zz} \quad (2.19)$$

$$u_x + w_z = 0 \quad (2.20)$$

$$P(T_t + uT_x + wT_z) = T_{xx} + T_{zz} \quad (2.21)$$

$$P_s [T_s]_t = [T_s]_{xx} + [T_s]_{zz}, \quad (2.22)$$

where $P = \nu/\kappa$ is the Prandtl number, and similarly $P_s = \nu/\kappa_s$. The boundary condition at the bottom of the solid substrate ($z = -d/d_0$) is now given by $T_s = 1$. The boundary conditions at $z = 0$ remain the same: $u = w = 0$, $T = T_s$ and $kT_z = k_s [T_s]_z$. At the liquid-gas interface ($z = h(x, t)$), mass balance, energy balance, and normal and shear stress balance are given as follows

$$EJ = (1 + h_x^2)^{-\frac{1}{2}} (w - uh_x - h_t) \quad (2.23)$$

$$(1 + h_x^2)^{-\frac{1}{2}} (T_x h_x - T_z) = J + \left(\frac{9E^2 \nu^2}{8D^2 L d_0^2} \right) J^3 \quad (2.24)$$

$$p - \frac{3E^2 J^2}{2D} - \frac{2 [u_x (h_x^2 - 1) - h_x (u_z + w_x)]}{(1 + h_x^2)} = \frac{3Sh_{xx} (1 - CT)}{(1 + h_x^2)^{\frac{3}{2}}} \quad (2.25)$$

$$-\frac{2M}{P} (1 + h_x^2)^{\frac{1}{2}} (T_x + h_x T_z) = (1 - h_x^2) (u_z + w_x) - 4h_x u_x. \quad (2.26)$$

If “lens” evaporation model is used, we also have expression for mass flux J in terms of h , given by Eq. (2.14). On the other hand, for NEOS evaporation model, we have additional boundary condition at $z = h$ given by Eq. (2.16). We also note that $\phi(h)$ from Eq. (2.18) is given by

$$\phi(h) = -3A \left[\left(\frac{b}{h} \right)^n - \left(\frac{b}{h} \right)^m \right] - 3Gh, \quad (2.27)$$

Table 2.1 Table of Parameter Values for IPA and DIW ([45])

Parameter	IPA	DIW
$T_{sat}(K)$	248	250
$\rho_v(kg/m^3)$	2.0	0.9
$\rho(kg/m^3)$	790	998
$\gamma(N/Km)$	$0.25 \cdot 10^{-3}$	$0.18 \cdot 10^{-3}$
$\sigma_0(N/m)$	$2.1 \cdot 10^{-2}$	$7.2 \cdot 10^{-2}$
$L(J/kg)$	$0.79 \cdot 10^6$	$2.44 \cdot 10^6$
$R_g(J/kgK)$	138.35	461.92
$\mu(kg/ms)$	$2.04 \cdot 10^{-3}$	$0.9 \cdot 10^{-3}$
$k(W/Km)$	$1.35 \cdot 10^{-1}$	$6.05 \cdot 10^{-1}$
$k_s(W/Km)$ (Si)	1.35	1.35
$k_s(W/Km)$ (Cu)	390	390

where the first term represents disjoining pressure effects (through (n, m) -type potential, e.g. see [68]), while the second term is due to gravity.

The nondimensional parameters appearing here are defined as follows ([7]): evaporation number $E = k\Delta T/(\rho\nu L)$, nondimensional surface tension $S = \sigma_0 d_0/(3\rho\nu^2)$, thermocapillary Marangoni number $M = \gamma\Delta T d_0/(2\rho\nu\kappa)$, $D = 3\rho_v/(2\rho)$, and $C = \gamma\Delta T/\sigma_0$, such that $SC = 2M/(3P)$. In addition, $A = \Omega d_0\rho/(3\mu^2 Nb)$ and $G = -d_0^3\rho^2 g/(3\mu^2)$. Here, $b = d_{prec}/d_0$, where d_{prec} is the precursor film thickness. Note that $\Omega = \sigma_0(1 - \cos\Theta)$, and $N = (n - m)/((n - 1)(m - 1))$, where $(n, m) = (3, 2)$ is used ([68]).

The Table 2.1 lists values of the most important material parameters. We concentrate on two types of pure liquids: IPA (isopropyl alcohol) and DIW (de-ionized water), and two types of solid substrates: silicon (Si) and copper (Cu). The values

for T_{sat} are obtained from Clausius-Clapeyron law (Eq. (2.1)). We make use of the tabulated values for DH_{vap} , p_{sat} , and R ([45]), while T_0 and p_0 are room temperature (298K) and pressure (1atm) respectively. The values of volatility parameters α and χ are obtained through experiments, discussed in Section 4.

2.5 The Lubrication Approximation

Next, we employ the lubrication approximation to simplify the problem. We rescale the independent variables and expand the dependent variables in asymptotic series in small parameter ϵ (wavenumber); upon substituting these expansions into our system Eqs. (2.18 - 2.26), we solve for p , u , and w . The original coordinates x , z and t become ξ , ζ and θ respectively, where $\xi = \epsilon x$, $\zeta = z$ and $\theta = \epsilon t$. It is assumed that u , J , T , and T_s are all $O(1)$. This implies that w is $O(\epsilon)$, in order for Eq. (2.20) to be valid. In addition, we assume that p and ϕ are both $O(1/\epsilon)$ ([7]). Therefore, the dependent variables are expanded as follows: $u = u_0 + \epsilon u_1 + \dots$, $J = J_0 + \epsilon J_1 + \dots$, $T = T_0 + \epsilon T_1 + \dots$, $T_s = T_{s0} + \epsilon T_{s1} + \dots$, $w = \epsilon w_0 + \epsilon^2 w_1 + \dots$, $p = \epsilon^{-1} p_0 + p_1 + \dots$, and $\phi = \epsilon^{-1} \phi_0 + \phi_1 + \dots$. The film thickness is the unknown ($h = h(\xi, \theta)$), and it is assumed to be $O(1)$. Next, we assume that D is $O(\epsilon^3)$, E is $O(\epsilon)$, M , A and G are all $O(\epsilon^{-1})$, and S is $O(\epsilon^{-3})$. Both \mathcal{K} and P are assumed to be $O(1)$. As a result, all of the physical effects that have been discussed thus far are retained. Formally, we write: $D = \hat{D}\epsilon^3$, $E = \hat{E}\epsilon$, $M = \hat{M}\epsilon^{-1}$, $A = \hat{A}\epsilon^{-1}$, $G = \hat{G}\epsilon^{-1}$, and $S = \hat{S}\epsilon^{-3}$, where \hat{D} , \hat{E} , \hat{M} , \hat{A} , \hat{G} and \hat{S} are all $O(1)$. We note that these assumptions lead to $\hat{S}C = 2\epsilon^2\hat{M}/(3P)$. As a result, when the shear stress is balanced by the Marangoni forces in Eq. (2.26), the normal stress balance (Eq. (2.25)) is free of thermocapillary effects at leading order.

To the leading order in ϵ , Eqs. (2.18 - 2.22) become (subscript '0' is dropped for simplicity)

$$u_{\zeta\zeta} = p_{\xi} + \phi_{\xi}, \quad -p_{\zeta} = 0, \quad u_{\xi} + w_{\zeta} = 0, \quad T_{\zeta\zeta} = 0, \quad [T_s]_{\zeta\zeta} = 0. \quad (2.28a, b, c, d, e)$$

The boundary condition at $\zeta = -d/d_0$ (the bottom of the solid layer) remains unchanged ($T_s = 1$), and so do the boundary conditions at $\zeta = 0$ (liquid-solid interface)

$$u = w = 0, \quad T_s = T, \quad -kT_{\zeta} = -k_s [T_s]_{\zeta}. \quad (2.29a, b, c)$$

Finally, Eqs. (2.23 - 2.26) reduce to the following boundary conditions at the liquid-gas interface ($\zeta = h(\xi, \theta)$)

$$\hat{E}J = w - uh_{\xi} - h_{\theta}, \quad J + T_{\zeta} = 0, \quad (2.30a, b)$$

$$p = \frac{3}{2} \frac{\hat{E}^2}{\hat{D}} J^2 - 3\hat{S}h_{\xi\xi}, \quad u_{\zeta} + 2\frac{\hat{M}}{P}(T_{\xi} + T_{\zeta}h_{\xi}) = 0. \quad (2.31a, b)$$

In addition to these boundary conditions, Eq. (2.14) provides expression for $J(h)$ when “lens” evaporation model is used. On the other hand, if NEOS evaporation model is used, Eq. (2.16) gives additional boundary condition at $\zeta = h(\xi, \theta)$.

The Governing Equation for the Liquid Thickness

First, the energy equations for the liquid and solid (Eqs. (2.28d) and (2.28e)) are solved subject to the boundary condition at $\zeta = -d/d_0$ ($T_s = 1$), the boundary conditions at $\zeta = 0$ (Eqs. (2.29b) and (2.29c)) and $\zeta = h$ (Eq. (2.30b)), and either Eq. (2.14) or Eq. (2.16). This yields the expressions for the liquid and solid temperature in terms of the mass flux $J(h)$

$$T = 1 - (\zeta + \mathcal{W})J, \quad T_s = 1 - \left(\zeta + \frac{k}{k_s} \mathcal{W} \right) J, \quad (2.32a, b)$$

where \mathcal{W} describes thermal effects in the solid and is given as $\mathcal{W} = kd/(k_s d_0)$. We use $d = 0.75\text{mm}$ as relevant solid thickness and note that $\mathcal{W} \sim O(1)$ for all considered liquid/solid configurations. When “lens” evaporation model is used, the expression for $J(h)$ is given by Eq. (2.14). If NEOS evaporation model is considered, we obtain ([24])

$$J = \frac{1}{h + \mathcal{K} + \mathcal{W}}. \quad (2.33)$$

Note that $\mathcal{K} + \mathcal{W}$ is dominant in the denominator of Eq. (2.33). Therefore, as $h \rightarrow 0$ (close to contact line of the drop), J given by Eq. (2.33) remains bounded. Furthermore, for DIW, $\mathcal{K} + \mathcal{W} \sim O(10)$, so that J given by Eq. (2.33) has only a weak dependence on h . On the other hand, J given by Eq. (2.14) diverges as $h \rightarrow 0$. We will see in Section 3 that this feature of J for “lens” evaporation model affects the temperature profiles at both the liquid-gas and liquid-solid interfaces.

We proceed by considering Eq. (2.28b), which suggests that $p \neq p(\zeta)$. Using the boundary condition at $\zeta = h$ given by Eq. (2.31a), we obtain the expression for pressure p

$$p = \frac{3}{2} \frac{\hat{E}^2}{\hat{D}} J^2 - 3\hat{S}h_{\xi\xi}. \quad (2.34)$$

This expression for p and the expression for $\phi(h)$ given by Eq. (2.27), are substituted into Eq. (2.28a). The velocity u is obtained by integrating twice with respect to ζ and making use of Eq. (2.32a), and boundary conditions given by Eqs. (2.29a) and (2.31b). The expression for u is then substituted into Eq. (2.28c) in order to solve for w , which is obtained by integrating Eq. (2.28c) with respect to ζ and making use

of the boundary condition given by Eq. (2.29a). The final step is the substitution of expressions for u , w , J , \hat{D} , \hat{E} , \hat{M} , \hat{A} , \hat{G} and \hat{S} into mass balance boundary condition given by Eq. (2.30b). This leads to a single nondimensional nonlinear partial differential equation for the thickness of the drop h as a function of time and in-plane coordinate x ([24])

$$\begin{aligned} \frac{\partial h}{\partial t} + EJ + S(h^3 h_{xxx})_x - \frac{E^2}{D} [h^3 J J_x]_x + \frac{M}{P} [h^2 (h + \mathcal{W}) J_x]_x \\ + \frac{M}{P} [h^2 J h_x]_x + A \left[h^3 \left(\left(\frac{b}{h} \right)^3 - \left(\frac{b}{h} \right)^2 \right) \right]_{x,x} + G [h^3 h_x]_x = 0. \end{aligned} \quad (2.35)$$

Eq. (2.35) is written in Cartesian coordinates and it is the governing equation for evaporation of a planar drop (cross-section of a cylindrical drop) or a film. In order to include effects of azimuthal curvature and consider the cross-section of a circular drop, we rewrite Eq. (2.35) in polar coordinates for $h = h(r, t)$

$$\begin{aligned} \frac{\partial h}{\partial t} + EJ + \frac{S}{r} \left[r h^3 \left(h_{rrr} + \frac{1}{r} h_{rr} - \frac{1}{r^2} h_r \right) \right]_r - \frac{E^2}{rD} [r h^3 J J_r]_r \\ + \frac{M}{rP} [r h^2 (h + \mathcal{W}) J_r]_r + \frac{M}{rP} [r h^2 J h_r]_r \\ + \frac{A}{r} \left[r h^3 \left(\left(\frac{b}{h} \right)^3 - \left(\frac{b}{h} \right)^2 \right) \right]_{r,r} + \frac{G}{r} [r h^3 h_r]_r = 0. \end{aligned} \quad (2.36)$$

Following a procedure similar to the one used in the derivation of Eq. (2.35), we derive the evolution equation for 3d problem. The governing equation for evolution of liquid thickness h as a function of time and in-plane coordinates x and y is given as

$$\begin{aligned} \frac{\partial h}{\partial t} + EJ + \nabla \cdot [S h^3 \nabla (\nabla^2 h)] - \nabla \cdot \left[\frac{E^2}{D} h^3 J \nabla J \right] + \nabla \cdot \left[\frac{M}{P} h^2 (h + \mathcal{W}) \nabla J \right] \\ + \nabla \cdot \left[\frac{M}{P} h^2 J \nabla h \right] + \nabla \cdot \left[A h^3 \nabla \left(\left(\frac{b}{h} \right)^3 - \left(\frac{b}{h} \right)^2 \right) \right] + \nabla \cdot [G h^3 \nabla h] = 0. \end{aligned} \quad (2.37)$$

The consecutive terms in Eqs. (2.35) and (2.36) describe viscous dissipation, evaporation, capillary effects, vapor recoil, thermocapillary Marangoni effects (two terms), disjoining pressure effect and gravity respectively. The Eq. (2.36) is going to be solved numerically. The results of our numerical simulations are discussed in Chapters 3 and 4. We note that in addition to divergence of J for “lens” model when $h \rightarrow 0$, our numerical code breaks down for the same limit. We use a single regularization mechanism to deal with both of these difficulties: the precursor film of thickness b . The details regarding the size of b are given in Chapters 3 and 4.

The Eqs. (2.35), (2.36) and (2.37) can be used for describing evolution of thickness for thin volatile films. Clearly, thin film configuration is incompatible with the “lens” evaporation model. Therefore, only NEOS evaporation model will be considered in that case.

CHAPTER 3

COMPUTATIONAL METHODS FOR EVAPORATIVE FILMS AND DROPS

In this chapter we discuss details of the numerical code which will be used for solving Eqs. (2.35) and (2.37) for evaporative film configuration, and Eqs. (2.35), (2.36) and (2.37) for evaporating drops. The numerical simulations of evaporating drops will allow us to compare the two evaporation models with the experimental data. First, we describe a finite difference-based numerical code, which we use for solving Eq. (2.35). We present details regarding space discretization of each term in Eq. (2.35), boundary conditions, time discretization, and time step control. An extension of this code to cylindrical geometry is used for solving Eq. (2.36). Next, we describe the 3d numerical code, which is used for solving Eq. (2.37). We list only few details regarding space and time discretization for this code, and mainly focus on describing ADI scheme which is used to handle the additional complexity introduced by considering the second space coordinate, y . Finally, we conclude this chapter with code validation, where we employ several tests in order to verify the validity of our codes for non-volatile configurations.

As it has been described in Chapter 2, our theoretical model requires the use of regularization mechanism in order to relieve both the usual difficulty in describing the contact line motion, and the mass flux singularity which occurs for “lens” evaporation model when $h \rightarrow 0$. It is also apparent that Eqs. (2.35), (2.36) and (2.37) are degenerate, in a sense that diffusivity h^3 in the highest order term in each of the equations vanishes as $h \rightarrow 0$ ([18]). Therefore, our numerical method also requires a regularization mechanism. This mechanism consists of introducing a thin precursor

film which covers the numerical domain – a method which results naturally from the disjoining pressure model used to describe solid-liquid interaction.

3.1 Numerical Codes for 2d Geometry

We first focus on a numerical code for solving Eq. (2.35). We recognize that aside for the time derivative of thickness h , the highest-order term (capillary) and the evaporation term, all other terms in Eq. (2.35) are similar in structure, and can be written as

$$\frac{\partial}{\partial x} \left[C_{diff}(h) \frac{\partial}{\partial x} F(h) \right]. \quad (3.1)$$

For instance, $C_{diff} = Gh^3$ and $F = h$ for the gravity term, while for the vapor recoil term $C_{diff} = -(E^2/D)h^3J(h)$ and $F = J(h)$. In order to simplify the description of the numerical code, we consider a simplified version of Eq. (2.35)

$$\frac{\partial h}{\partial t} = -S(h^3h_{xxx})_x - G[h^3h_x]_x. \quad (3.2)$$

The approach identical to the one which we use for treating the gravity term in Eq. (3.2) will be used for treating the rest of the lower order terms in Eq. (2.35).

3.1.1 Spatial Discretization

The numerical domain is defined as $0 \leq x \leq x_{max}$. We use an uniform grid, where constant Δx is prescribed in view of precursor thickness b ($\Delta x < b$). The k th grid point is denoted by x_k , with $1 \leq k \leq N + 1$. The method which we use for spatial discretization of terms in Eq. (3.2) is second-order accurate finite-difference based method. In particular we use central differences, which leads to the following system of ordinary differential equations

$$\frac{\partial h_k}{\partial t} = -f_k, \quad (3.3)$$

where f_k is the discretization of the right-hand side of the Eq. (3.2).

First, we focus on the discretization of the capillary term, which is performed in the following manner

$$\frac{\partial}{\partial x} \left[h^3 \frac{\partial^3 h}{\partial x^3} \right] \Big|_k \approx \frac{\mathcal{S}_{k+1} s_{k+1} - \mathcal{S}_k s_k}{\Delta x}, \quad (3.4)$$

where \mathcal{S}_k is the discretization of the nonlinear diffusivity (h^3), and s_k is the discretization of the third derivative term (h_{xxx}). Both are centered in the middle of the element $[x_k, x_{k+1}]$. The discretization of nonlinear diffusivity deserves closer attention. The reason for this is following. Eq. (3.2) has an interesting property: it does not satisfy the maximum principle ([17, 18, 42]). Hence, an initially positive data may lead to a negative solution ($h < 0$). We note that even in problems where positivity of the solution is guaranteed analytically, the computations may still produce ‘false’ singularities ($h \leq 0$). The occurrence of non-positive solutions is to be avoided, since it introduces artificial instability and inaccuracy into the system. The standard finite difference scheme yields the following expression for \mathcal{S}_k

$$\mathcal{S}_k = \frac{h_k^3 + h_{k-1}^3}{2}. \quad (3.5)$$

Usually, the conventional finite difference schemes are ill-equipped for maintaining the positivity of the solution. Therefore, we use a particular positivity-preserving scheme (PPS), described in [18], which utilizes the idea of Lyapunov dissipation. In particular, one can use the so-called Lyapunov ‘entropy’ dissipation

$$\frac{d \int L_E(h) dx}{dt} = - \int |\nabla^2 h|^2 dx, \quad (3.6)$$

where $L_E(h)'' = 1/h^3$, and therefore $L_E(h) \sim 1/h$, in order to show that positive initial condition always yields a positive solution, at least for the planar case in one space dimension ([18]). Hence, we use the discretized version of Eq. (3.6) to obtain the expression for \mathcal{S}_k

$$\mathcal{S}_k = \begin{cases} \frac{h_k - h_{k-1}}{e_k - e_{k-1}} = 2 \frac{h_k^2 h_{k-1}^2}{h_k + h_{k-1}} & \text{if } h_k \neq h_{k-1}, \\ \frac{h_k^3 + h_{k-1}^3}{2} & \text{if } h_k = h_{k-1}, \end{cases} \quad (3.7)$$

where $e(h) = \int h^{-3} dh = 1/(2h^2)$. The expression for s_k is given as ([17, 18, 42])

$$s_k = \frac{h_{k+1} - 3h_k + 3h_{k-1} - h_{k-2}}{(\Delta x)^3}. \quad (3.8)$$

Next, we turn to the gravity term, which is discretized as

$$\frac{\partial}{\partial x} \left[h^3 \frac{\partial h}{\partial x} \right] \Big|_k \approx \frac{\mathcal{G}_{k+1} g_{k+1} - \mathcal{G}_k g_k}{\Delta x}. \quad (3.9)$$

Here, \mathcal{G}_k is the discretization of h^3 term, for which we use averaging instead of the positivity-preserving scheme

$$\mathcal{G}_k = \frac{h_k^3 + h_{k-1}^3}{2}. \quad (3.10)$$

The discretization of the first derivative term (h_x) is given by

$$g_k = \frac{h_k - h_{k-1}}{\Delta x}. \quad (3.11)$$

The Marangoni, vapor recoil and disjoining pressure terms in Eq. (2.35) are discretized using the same procedure as the one used for the gravity term. For example, $C_{diff} = h^3 J(h)$ is discretized as

$$h^3 J(h) \approx \frac{h_k^3 J(h_k) + h_{k-1}^3 J(h_{k-1})}{2}, \quad (3.12)$$

and $F = J(h)$ as

$$\frac{\partial J(h)}{\partial x} \approx \frac{J(h_k) - J(h_{k-1})}{\Delta x}. \quad (3.13)$$

3.1.2 Boundary Conditions

In our work, we concentrate on problems for which it is convenient to assume no-flow conditions at the boundaries of the numerical domain. These boundary conditions are of Neumann type. They are implemented by requiring that the normal component of the fluid flux $h\mathbf{v}$ vanishes at the boundaries of the numerical domain ($x_1 = 0$ and $x_{N+1} = x_{max}$). This requirement is satisfied when ([17, 18, 42])

$$\frac{\partial h}{\partial x} = \frac{\partial^3 h}{\partial x^3} = 0 \quad (3.14)$$

at both $x = x_1$ and $x = x_{N+1}$. It is obvious that the discretization scheme which we have described in Section 3.1.1 requires the use of a pair of fictitious grid points outside the numerical domain at each boundary. The boundary condition given by Eq. (3.14) provides the values of h at those ‘ghost’ points. In particular, these values are mirror images of values of h at two interior adjacent grid points

$$h_{-1} = h_3, \quad h_0 = h_2, \quad h_{N+2} = h_N, \quad h_{N+3} = h_{N-1}. \quad (3.15a, b, c, d)$$

The boundary conditions given by Eq. (3.15) ensure no net flux through the boundaries of the numerical domain, which implies that the total liquid volume

$$V_{total} = \int_0^{x_{max}} h(x, t) dx = \sum_{k=1}^{N+1} h_k^n \Delta x \quad (3.16)$$

remains constant in time for non-volatile case. In practice, the requirement of constancy of liquid volume serves as a valuable tool for estimating the accuracy of the solution ([17, 18, 42]). The numerical results which we present in this chapter (non-volatile configuration only), preserve V_{total} with a relative error less than 10^{-11} .

3.1.3 Time Discretization

The time discretization of Eq. (3.2) is performed using a θ -weighted scheme

$$\frac{h_k^{n+1} - h_k^n}{\Delta t^n} = -\theta f_k^{n+1} - (1 - \theta) f_k^n, \quad (3.17)$$

where h_k^n stands for discretization of solution at time t_n , Δt^n is the time step at time t_n , and f_k^n is the discretization of the right-hand side of the Eq. (3.2) at time t_n . Here, $\theta = 0$ corresponds to the forward Euler scheme (explicit and $O(\Delta t^n)$), while $\theta = 1$ corresponds to the backward Euler scheme, (implicit and $O(\Delta t^n)$). Our approach consists of using $\theta = 1/2$ (Crank-Nicholson scheme), which is implicit and $O((\Delta t^n)^2)$. The Crank-Nicholson scheme adds to the complexity of the numerical code, with the benefits of being $O((\Delta t^n)^2)$ and numerical stability (it is unconditionally stable). We note that Eq. (3.17) yields a system of $N + 1$ algebraic equations, which are to be solved simultaneously. The difficulty is in the fact that these equations are highly non-linear, due to the nature of right-hand side terms f_k . Therefore, it is necessary to linearize these equations, and they are solved using an iterative Newton-Kantorovich's method ([17, 18, 42]).

We briefly describe this iterative process next. The solution of Eq. (3.2) at time t_{n+1} is given as

$$h_k^{n+1} = h_k^* + c_k, \quad (3.18)$$

where h_k^* is a guess for solution at time t_{n+1} , and c_k is the correction. There are several different approaches for choosing the guess h_k^* , and we use the simplest: $h_k^* = h_k^n$ (the solution at time t_n). Upon substituting Eq. (3.18) into Eq. (3.17), we obtain

$$c_k + \Delta t \theta \tilde{f}_k = h_k^n - \Delta t (1 - \theta) f_k^n - h_k^* - \Delta t \theta f_k^*, \quad (3.19)$$

where \tilde{f}_k and f_k^* are f_k 's calculated using c_k and h_k^* respectively. The linearization of the non-linear terms in Eq. (3.19) is achieved in the following manner. We expand these terms in Taylor series around the guess h_k^*

$$f_k^{n+1} = f_k^* + \left. \frac{\partial f_k}{\partial h_j} \right|_{h_j^*} c_j, \quad (3.20)$$

where summation over repeated index j is understood, and the derivative is calculated using the guess h_k^* . After substituting Eq. (3.20) into Eq. (3.19), we obtain

$$\left[\delta_{k,l} + \Delta t^n \theta \left. \frac{\partial f_k}{\partial h_l} \right|_{h_l^*} \right] c_l = R_k, \quad (3.21)$$

where $\delta_{k,l}$ is Kronecker delta, and the right-hand side is

$$R_k = h_k^n - \Delta t (1 - \theta) f_k^n - h_k^* - \Delta t \theta f_k^*. \quad (3.22)$$

The iterations proceed in the following manner. Eq. (3.21) yields $N+1$ linear algebraic equations, which are solved for the correction c_k . If $Q = \max_k(c_k) \geq Q_{tol}$, where $Q_{tol} \sim O(10^{-10})$ is prescribed tolerance for the Newton-Kantorovich's method, the

guess h_k^* is updated by c_k . A new guess now becomes $h_k^* + c_k$ and this procedure is iteratively performed until $Q < Q_{tol}$. At this stage, the Newton-Kantorovich's method has converged, and the guess used in the last iteration is taken as a candidate for the solution at new time (h_k^{n+1}). A set of checks, which are being performed on this candidate solution before it is accepted as h_k^{n+1} , are described in the next section. It is important to note that the first two terms which comprise R_k in Eq. (3.22) involve the 'old' solution h_k^n only, and in the iterative process these terms are calculated only once (at the first iteration). On the other hand, the last two terms on the right-hand side (RHS) of Eq. (3.22) are calculated using the guess h_k^* , and hence they are being re-calculated after every iteration, using the updated guess.

3.1.4 Error Control

The unconditional stability of the Crank-Nicholson scheme when applied to linear second- and fourth-order parabolic problems is well known. However, for our non-linear problem, with additional lower order terms, this is not clear. Therefore, one needs to be careful when it comes to deciding the size of time step Δt . There are several issues which need to be considered.

The first requirement is accuracy related. Once the iterative method converges, the obtained solution must satisfy the accuracy requirements. These requirements for Crank-Nicholson scheme are formulated in the following manner ([17]). Keeping in mind that the scheme is $O((\Delta t)^2)$, the relative error of the numerical solution at a grid point x_k is

$$Er_k = \frac{(\Delta t^n)^2}{h_k^n} \left| \frac{d^2 h_k^n}{dt^2} \right|. \quad (3.23)$$

The expression for maximum error is obtained from Eq. (3.23) by multiplying the expansions around h_k^n and h_k^{n-1} by the time steps which have been used before and after time t^n (Δt^{n-1} and Δt^n) respectively, and finally summing ([17])

$$Er_{max} = \max_{1 \leq k \leq N+1} \left[2 \frac{\Delta t^n}{\Delta t^{n-1}} \frac{\Delta t^{n-1} h_k^{n+1} + \Delta t^n h_k^{n-1} - (\Delta t^{n-1} + \Delta t^n) h_k^n}{(\Delta t^{n-1} + \Delta t^n) h_k^n} \right]. \quad (3.24)$$

It is required that $Er_{max} < Tol$, where $Tol \sim 10^{-3}$ is prescribed, in order for the solution h_k^{n+1} (calculated using time step Δt^n) to be acceptable. If this requirement is not satisfied, time step is halved and the iteration process is repeated.

The second requirement is concerning preservation of the positivity of the solution. Since the solution has to be strictly positive, the time step is halved and the iteration process is repeated if the h_k^{n+1} calculated using time step Δt^n is smaller than some prescribed tolerance. Finally, we recognize that the guess for solution at time t^{n+1} may not be close to the correct solution h_k^{n+1} , possibly causing previously described Newton-Kantorovich's method to fail to converge in a reasonable number of iterations, and hence, hampering the efficiency of the code. In such a case, time step is again halved and the iteration process is repeated.

We use these three criteria to dynamically determine the size of the time step. This process includes an additional time step recovery mechanism, which allows for increase of time step after prescribed number of consecutive iterations converge successfully.

3.1.5 Extension to Cylindrical Geometry

The focus of discussion in Sections 3.1.1- 3.1.4 has been on numerical code for solving Eq. (2.35) for both films and drops. Identical approach regarding spatial and time discretization, as well as boundary conditions and error control is used for deriving a numerical code for solving Eq. (2.36) for drops. The only subtlety of this code is

concerning the numerical domain and the positioning of the grid, which is required to be shifted by $\Delta r/2$ to the interior of the domain in order to avoid the consideration of the grid point $r = 0$ (origin), for which the Eq. (2.36) is ill-posed. We note that only minor modifications of the no-flux boundary conditions given by Eq. (3.16) are required, which amount to keeping track of the new grid positioning.

In particular, the modified grid is given by: $r_1 = (1/2)\Delta r$, $r_2 = (3/2)\Delta r, \dots$, $r_N = (N - 1/2)\Delta r$. Note that $r_{N+1} = (N + 1/2)\Delta r$ is outside of the numerical domain. The no-flux boundary condition is enforced by ensuring that the flux at the boundaries of the domain vanishes

$$h^3 \frac{\partial}{\partial r} \left[\frac{\partial^2 h}{\partial r^2} + \frac{1}{r} \frac{\partial h}{\partial r} \right] \Big|_{r=0} = 0, \quad h^3 \frac{\partial}{\partial r} \left[\frac{\partial^2 h}{\partial r^2} + \frac{1}{r} \frac{\partial h}{\partial r} \right] \Big|_{r=r_{max}} = 0. \quad (3.25a, b)$$

Eq. (3.25) leads to the boundary conditions

$$h_{-1} = h_2, \quad h_0 = h_1, \quad h_{N+1} = h_N, \quad h_{N+2} = \frac{(2N^2 - N - 1) h_{N-1} + 2N h_N}{2N^2 + N - 1}. \quad (3.26a, b, c, d)$$

3.1.6 Code Validation

The next step is the validation of our numerical codes for solving Eqs. (2.35) and (2.36). An obvious way to achieve this is by comparing our numerical results with an analytical solution. However, known analytical solutions correspond to scenarios which are much simpler than the ones modeled by Eqs. (2.35) and (2.36) in their full form. We therefore consider non-volatile scenario, which eliminates evaporation, Marangoni and vapor recoil terms from these equations. In addition, we also neglect disjoining pressure effects, and consider a drop configuration. This leaves us with only the fourth-order capillary term and the gravity term, and allows us to model spreading of 2d planar (Eq. (2.35)) or radial (Eq. (2.36)) drops of completely wetting liquids ($\Theta = 0$) under the influence of surface tension and gravity.

The analytical solution which we use for validation of our numerical codes is the so-called Barenblatt solution ([4]). This is a self-similar solution, which models the radial spreading of drops under influence of gravity only. We note that this solution does not assume the presence of a precursor film, and hence we expect that our numerical results approach the Barenblatt solution as thickness of the precursor film used in our applications vanishes ($b \rightarrow 0$). The numerical results presented are obtained using a precursor film of thickness $d_0 b \leq 0.625 \mu m$. This choice will be explained in more detail in Chapter 4. The Barenblatt solution gives the asymptotic flow for any choice of initial condition. Here, we consider a spherical cap initial condition, with volume of $5 \mu l$. Using length and time scales described in Chapter 2, the Barenblatt solution is given by

$$R(t) = 2.37 (t)^{1/8}, \quad (3.27)$$

where R denotes the position of the contact line of the drop. We expect that our numerical results should asymptotically approach the Barenblatt solution for $R \gg l_c$, where $l_c = \sqrt{\sigma/(\rho g)}$ is the capillary length ([18]). We also expect that for precursor thickness b which we use, our numerical results should exhibit an asymptotic behavior with exponent $1/8$ as in Eq. (3.27).

Figure 3.1 shows comparison of our numerical results for both planar and radial drops and compares them against the Barenblatt solution (Eq. (3.27)). We note that the asymptotic behavior of our numerical results in general agrees well with the Barenblatt solution. The agreement between numerical results for radial drop and Barenblatt solution are excellent: the asymptotic behavior for radial case follows exactly exponent $1/8$. This is not surprising, since this exponent is direct consequence of global volume conservation ([18]). The exponent for planar drop is bit larger than $1/8$. Furthermore, we note that even for large values of R , capillary effects may still

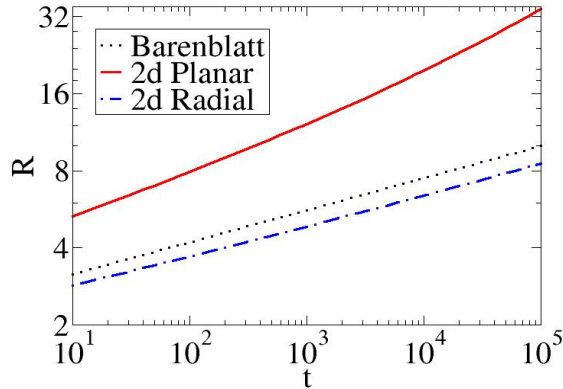


Figure 3.1 The comparison of numerical results for spreading of 2d planar and radial drops against the Barenblatt solution (Eq. (3.27)).

be quite relevant in the region close to the contact line. This is manifested especially in planar case through an increase of exponent at late times, as seen in Figure 3.1.

3.2 Quasi-3d Numerical Code

In order to develop a numerical code for solving Eq. (2.37), we use methods which are similar to those described in Section 3.1. The time discretization and error control are identical to those for 2d codes, while the space discretization and boundary conditions are extended to include an additional in-plane coordinate y . We omit those details here to avoid repetition. Instead, we focus on the alternating direction implicit (ADI) scheme, the use of which significantly reduces the complexity of the code. Our ADI scheme is based on a similar scheme developed in [71] for non-linear fourth-order parabolic problems.

We first explain in some detail the construction of the code for the case when only the fourth-order term is considered

$$\frac{\partial h}{\partial t} = -\nabla \cdot [Sh^3 \nabla (\nabla^2 h)], \quad (3.28)$$

where $h = h(x, y, t)$. We follow closely [71]. The fourth-order term now contains mixed derivatives, which further increase the complexity of the problem. Upon using θ -weighted scheme for time discretization of Eq. (3.28), we obtain the following equation

$$\begin{aligned} & [I + \theta \Delta t \nabla \cdot [\mathcal{S}_{k,l}^{n+1} \nabla \nabla^2]] h_{k,l}^{n+1} = \\ & [I - (1 - \theta) \Delta t \nabla \cdot [\mathcal{S}_{k,l}^n \nabla \nabla^2]] h_{k,l}^n, \end{aligned} \quad (3.29)$$

where we use the notation equivalent to the one in Section 3.1. We note that I is an identity operator, while superscripts n and $n + 1$ denote times t^n and t^{n+1} . The subscripts denote space discretization. Next, we make use of a factorization of the operator on the LHS of Eq. (3.29), which has been derived in [71]

$$\begin{aligned} & [I + \theta \Delta t \nabla \cdot [\mathcal{S}_{k,l}^{n+1} \nabla \nabla^2]] = \\ & [I + \theta \Delta t \partial_x [\mathcal{S}_{k,l}^{n+1} \partial_{xxx}]] [I + \theta \Delta t \partial_y [\mathcal{S}_{k,l}^{n+1} \partial_{yyy}]] + \\ & \theta \Delta t \partial_x [\mathcal{S}_{k,l}^{n+1} \partial_{xyy}] + \theta \Delta t \partial_y [\mathcal{S}_{k,l}^{n+1} \partial_{yxx}] - \\ & \theta^2 \Delta t^2 \partial_x [\mathcal{S}_{k,l}^{n+1} \partial_{xxx}] \partial_y [\mathcal{S}_{k,l}^{n+1} \partial_{yyy}], \end{aligned} \quad (3.30)$$

and write the solution at new time t^{n+1} as a sum of a guess (solution at time t^n) and the correction: $h_{k,l}^{n+1} = h_{k,l}^* + c_{k,l}$. Finally, we obtain

$$\begin{aligned} & [I + \theta \Delta t \partial_x [\mathcal{S}_{k,l}^* \partial_{xxx}]] [I + \theta \Delta t \partial_y [\mathcal{S}_{k,l}^* \partial_{yyy}]] c_{k,l} = \\ & [I - (1 - \theta) \Delta t \nabla \cdot [\mathcal{S}_{k,l}^n \nabla \nabla^2]] h_{k,l}^n - \\ & [I + \theta \Delta t \nabla \cdot [\mathcal{S}_{k,l}^* \nabla \nabla^2]] h_{k,l}^*. \end{aligned} \quad (3.31)$$

The operator on the LHS of Eq. (3.31) can now be split into two: one which operates exclusively in the x -direction and the other which operates in the y -direction only.

Hence, Eq. (3.31) can be rewritten as a 2-step process

$$\begin{aligned}
& [I + \theta \Delta t \partial_x [\mathcal{S}_{k,l}^* \partial_{xxx}]] w_{k,l} = \\
& [I - (1 - \theta) \Delta t \nabla \cdot [\mathcal{S}_{k,l}^n \nabla \nabla^2]] h_{k,l}^n - \\
& [I + \theta \Delta t \nabla \cdot [\mathcal{S}_{k,l}^* \nabla \nabla^2]] h_{k,l}^*, \tag{3.32}
\end{aligned}$$

and

$$[I + \theta \Delta t \partial_y [\mathcal{S}_{k,l}^* \partial_{yyy}]] c_{k,l} = w_{k,l}. \tag{3.33}$$

We note that both the x -step (Eq. (3.32)) and the y -step (Eq. (3.33)) require linearization of non-linear terms. For this purpose, we use Newton-Kantorovich's method, which has been described in Section 3.1. Both x - and y - steps involve this iterative procedure. Once the iterative procedure converges to $w_{k,l}$ in the x -step, the $w_{k,l}$ is used as a RHS for the y -step. Once the iterative procedure in the y -step converges to correction $c_{k,l}$, the guess $h_{k,l}^*$ is updated. This procedure continues until $Q = \max_{k,l}(c_{k,l}) < Q_{tol}$, when the candidate for solution $h_{k,l}^{n+1}$ is checked against the three criteria described in Section 3.1.4.

We use similar procedure to construct the 3d code for the case when gravity is taken into account along with the fourth-order term. The equation which we consider is the 3d equivalent of Eq. (3.2)

$$\frac{\partial h}{\partial t} = -\nabla \cdot [Sh^3 \nabla (\nabla^2 h)] - \nabla \cdot [Gh^3 \nabla h]. \tag{3.34}$$

Using a θ -weighted scheme for time discretization yields

$$\begin{aligned}
& [I + \theta \Delta t \nabla \cdot [\mathcal{S}_{k,l}^{n+1} \nabla \nabla^2 + \mathcal{G}_{k,l}^{n+1} \nabla]] h_{k,l}^{n+1} = \\
& [I - (1 - \theta) \Delta t \nabla \cdot [\mathcal{S}_{k,l}^n \nabla \nabla^2 + \mathcal{G}_{k,l}^n \nabla]] h_{k,l}^n. \tag{3.35}
\end{aligned}$$

We modify the factorization of the LHS given in Eq. (3.30) in order to allow for consideration of any lower order term (e.g. gravity)

$$\begin{aligned}
& [I + \theta \Delta t \nabla \cdot [\mathcal{S}_{k,l}^{n+1} \nabla \nabla^2 + \mathcal{G}_{k,l}^{n+1} \nabla]] = \\
& [I + \theta \Delta t \partial_x [\mathcal{S}_{k,l}^{n+1} \partial_{xxx} + \mathcal{G}_{k,l}^{n+1} \partial_x]] [I + \theta \Delta t \partial_y [\mathcal{S}_{k,l}^{n+1} \partial_{yyy} + \mathcal{G}_{k,l}^{n+1} \partial_y]] + \\
& \theta \Delta t \partial_x [\mathcal{S}_{k,l}^{n+1} \partial_{xyy}] + \theta \Delta t \partial_y [\mathcal{S}_{k,l}^{n+1} \partial_{yxx}] - \\
& \theta^2 \Delta t^2 \partial_x [\mathcal{S}_{k,l}^{n+1} \partial_{xxx} + \mathcal{G}_{k,l}^{n+1} \partial_x] \partial_y [\mathcal{S}_{k,l}^{n+1} \partial_{yyy} + \mathcal{G}_{k,l}^{n+1} \partial_y]. \tag{3.36}
\end{aligned}$$

Upon using this factorization and writing the solution at new time t^{n+1} as a sum of a guess (solution at time t^n) and the correction: $h_{k,l}^{n+1} = h_{k,l}^* + c_{k,l}$, we obtain

$$\begin{aligned}
& [I + \theta \Delta t \partial_x [\mathcal{S}_{k,l}^* \partial_{xxx} + \mathcal{G}_{k,l}^* \partial_x]] [I + \theta \Delta t \partial_y [\mathcal{S}_{k,l}^* \partial_{yyy} + \mathcal{G}_{k,l}^* \partial_y]] c_{k,l} = \\
& [I - (1 - \theta) \Delta t \nabla \cdot [\mathcal{S}_{k,l}^n \nabla \nabla^2 + \mathcal{G}_{k,l}^n \nabla]] h_{k,l}^n - \\
& [I + \theta \Delta t \nabla \cdot [\mathcal{S}_{k,l}^* \nabla \nabla^2 + \mathcal{G}_{k,l}^* \nabla]] h_{k,l}^*. \tag{3.37}
\end{aligned}$$

After splitting the operator on the LHS of Eq. (3.37) into one which operates exclusively in the x -direction and the other which operates in the y -direction only, we obtain a 2-step process

$$\begin{aligned}
& [I + \theta \Delta t \partial_x [\mathcal{S}_{k,l}^* \partial_{xxx} + \mathcal{G}_{k,l}^* \partial_x]] w_{k,l} = \\
& [I - (1 - \theta) \Delta t \nabla \cdot [\mathcal{S}_{k,l}^n \nabla \nabla^2 + \mathcal{G}_{k,l}^n \nabla]] h_{k,l}^n - \\
& [I + \theta \Delta t \nabla \cdot [\mathcal{S}_{k,l}^* \nabla \nabla^2 + \mathcal{G}_{k,l}^* \nabla]] h_{k,l}^*, \tag{3.38}
\end{aligned}$$

and

$$[I + \theta \Delta t \partial_y [\mathcal{S}_{k,l}^* \partial_{yyy} + \mathcal{G}_{k,l}^* \partial_y]] c_{k,l} = w_{k,l}. \tag{3.39}$$

We omit further details since they are identical to the ones listed for Eqs. (3.32) and (3.33).

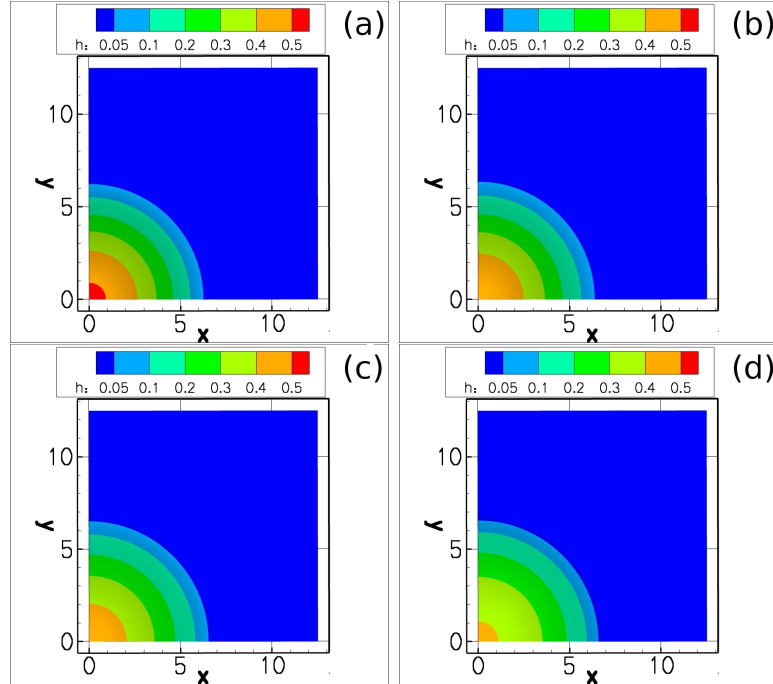


Figure 3.2 Spreading of a non-volatile circular drop (numerical results). (a) $t = 0$; (b) $t = 0.3$; (c) $t = 0.7$; (d) $t = 1$. Note that the circular symmetry of the drop is preserved as the spreading proceeds.

Finally, we note that the rest of the lower order terms in Eq. (2.37) are treated using the same approach as the one we have described here for the gravity term. We note that the factorization of the LHS of Eq. (3.35) does not allow for inclusion of terms which have no derivatives. Hence, the evaporation term is treated explicitly.

Code Validation

We validate our 3d numerical code by considering spreading of non-volatile drops. For efficiency, we use precursor films of larger thickness ($d_0 b = 10\mu m$).

The first test to which we subject our code is radial spreading of a circular drop. The initial condition is a spherical cap of volume $5\mu l$, while the contact angle is $\Theta = \pi/30$. The numerical results are shown in Figure 3.2, and they confirm that our code maintains the circular symmetry of the drop in addition to preserving mass.

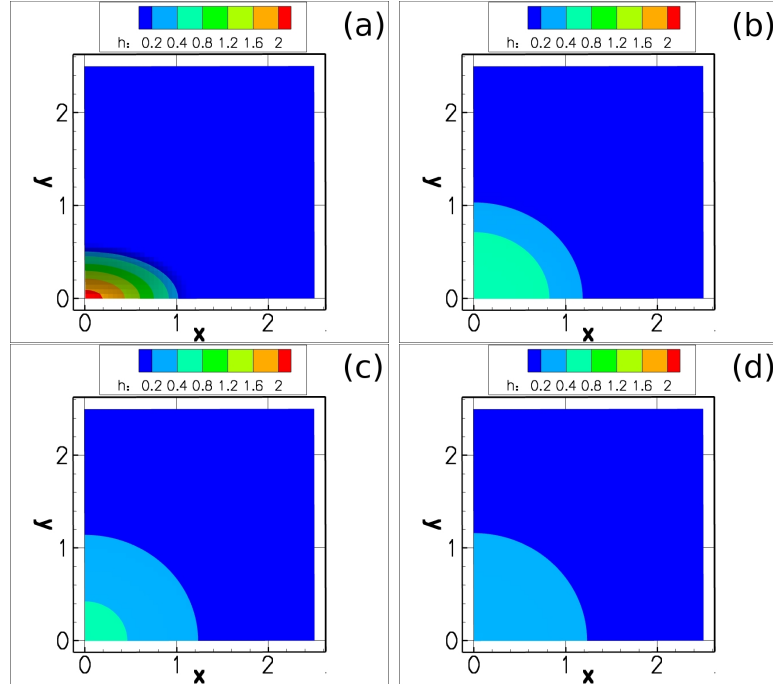


Figure 3.3 Spreading of an initially elliptic drop (numerical results). The initial condition ($t = 0$) is shown in (a); the final state ($t = 0.01$) is shown in (d); the circular symmetry is already achieved at $t = 0.003$ in (b).

Next, we examine the elliptical spreading problem, where a non-volatile drop with initially elliptical symmetry ([17]) spreads subject to gravity, surface tension and disjoining pressure. The results are shown in Figure 3.3, which indicates that, in addition to preserving mass, the code confirms the expected transition from elliptical to circular symmetry.

Finally, we use our code to simulate the coalescence of two non-volatile sessile drops, which spread simultaneously on a horizontal solid substrate. This exercise provides an excellent test for capabilities of our 3d code: it considers both the spreading process and the phenomena of coalescence. We consider a completely wetting fluid, which corresponds to choosing contact angle $\Theta = 0$. Similar test has been performed in [17]. The initial condition consists of two identical spherical caps, positioned in the numerical domain such that their respective centers are at $(0, 0)$ and $(0, y_{M+1})$.

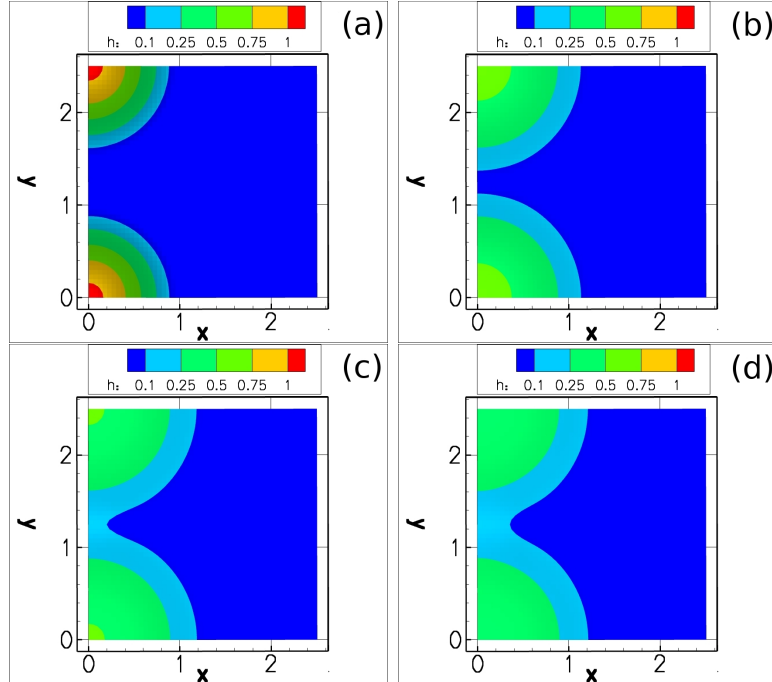


Figure 3.4 Coalescence of non-volatile sessile drops (numerical results). (a) $t = 0$: the initial condition; (b) $t = 0.0033$: the spreading stage; (c) $t = 0.0066$: the configuration during coalescence; (d) $t = 0.01$: after coalescence.

The initial radius of each drop is $R \approx 0.9$, and the size of the computational domain is chosen so that the spreading phase occurs before coalescence ($y_{M+1} > 2$).

The numerical results are shown in Figure 3.4. The spreading phase is shown in Figure 3.4(b), as it precedes the actual coalescence, which is shown in (c). The contact between two drops breaches the radial symmetry of each drop. We note that in this case, as in [17], the mirror symmetry with respect to the line $x = 0$ is preserved. In addition, the symmetry with respect to the lines $y = 0$ and $y = y_{M+1}$ is also preserved. Therefore, we can use this set-up to simulate the coalescence of an infinite array of equidistant drops, which are located along the $x = 0$ line, with centers at $\dots, -2y_{M+1}, -y_{M+1}, 0, y_{M+1}, 2y_{M+1}, \dots$. Since in that case each drop coalesces with only two neighboring drops, it is sufficient to carry out the simulations in the first quadrant only ([17]). In addition, our code can also handle the situation where two

isolated drops collide, but in that case the size of the computational domain cannot be reduced using the symmetry argument.

CHAPTER 4

EVAPORATIVE DROPS: EXPERIMENTS AND NUMERICAL SIMULATIONS

The volatility parameters are the final pieces of our modeling puzzle which we have started assembling in Chapter 2. The tools which we have developed in Chapter 3 will allow for comparison of numerical results for the two evaporation models against the experimental data. We first focus on goniometer experiments and present the techniques which we use for capturing the dynamics of volatile drops. Next, we discuss methods for calculating the volatility coefficients from the experimental data. Finally, we perform numerical simulations of Eq. (2.36) for the two evaporation models and compare these results against numerical data in order to decide which evaporation model is more appropriate in a particular physical situation.

4.1 The Experimental Procedure

The main goal of the experiments is twofold: first, they provide data regarding the rate of mass loss and allow to estimate the values of volatility parameters χ and

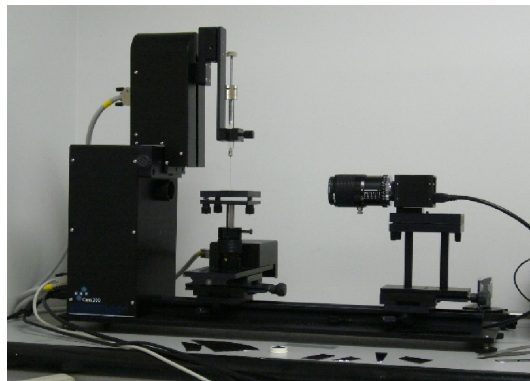


Figure 4.1 The goniometer: camera, syringe and the deposition platform.

α ; second, the experimental data regarding evolution of the drop volume and the position of the contact line will provide benchmark for the two theoretical models.

We carry out the experiments using a goniometer (KSV CAM 200), which consist of a camera, light source, static deposition platform, and a Hamilton 1001 Gas-Tight syringe, all of which are shown in Figure 4.1. The experiments are performed at room temperature and in open atmosphere, making precautionary measures to shield the experiment from possible sources of air convection. The syringe is used to deposit a drop of desired volume onto a solid substrate. We perform a series of experiments with DIW drops evaporating on Si and Cu solid substrates. Pure liquid and solids with semiconductor grade smoothness are used. The camera records series of images of drop's profile at pre-set time instants. The software analyzes each image and, using spherical cap approximation, yields height and radius of a drop. Using these data, we monitor variation of surface area and volume of the drop as evaporation proceeds. Figure 4.2 shows four such images recorded during evaporation of a $\sim 4.9\mu\text{l}$ drop of DIW on a Si substrate.

The images are recorded at time instances t_1, t_2, \dots, t_N , which are $8s$ apart. The data consists of radius of the drop $R(t_k) = R_k$, height of the drop $H(t_k) = H_k$, and the contact angle $\Theta(t_k) = \Theta_k$ for any time instant t_k , where $k = 1, \dots, N$. Figure 4.3 shows the resulting radius and volume of evaporating DIW drop on Si substrate as a function of time. In agreement with other works, we find linear decrease of volume for the considered time interval ([13, 15, 22, 33, 40]). We note that the experimental data that we have obtained, show no contact line pinning for any of the solid/liquid configurations considered. This confirms our modeling assumption that the drop contact line moves freely. It has been reported by other authors (e.g. [33, 40]) that pinning of the contact line of evaporating drops of water is to be expected. There are several possible explanations for this difference. First, in [33], each drop contains small tracer particles, which are deliberately injected in order to allow for visualization

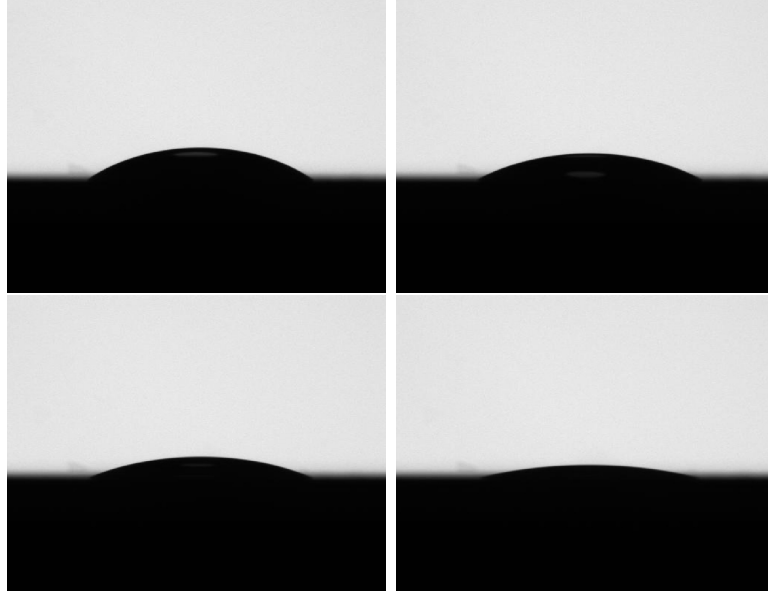


Figure 4.2 Snapshots of evaporating DIW drop on Si substrate, as recorded by the experimental setup at 56s (top left) , 256s (top right), 440s (bottom left), and 536s (bottom right).

of the drop profiles as evaporation proceeds. While these tracers are unlikely to affect the drop shape, they may enhance the pinning of contact line. Second, in [33] plain glass substrate is used, and therefore surface roughness is significantly larger than the one of solid substrates we have used (both Si and Cu wafers are semi-conductor grade of maximum surface roughness of $0.5nm$). Increased surface roughness is known to induce pinning of the contact line. In any case, our experiments support the argument that contact line pinning is not a generic feature of problems involving evaporating drops, and therefore, contact line should be allowed to move.

Using the collected data, we calculate the evaporation flux J^{tot}_k valid for each time interval $[t_k, t_{k+1}]$

$$J^{tot}_k = \frac{\rho \Delta V_k}{S^{avg}_k \Delta t_k}, \quad (4.1)$$

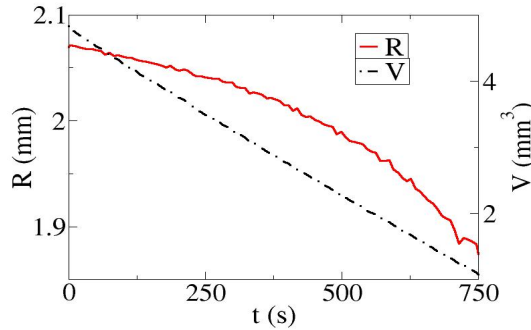


Figure 4.3 Evolution of volume and radius of a drop of DIW on a Si substrate.

where $\Delta V_k = V_k - V_{k+1}$, $\Delta t_k = t_{k+1} - t_k$, and $S^{avg}_k = (S_k + S_{k+1})/2$. The sequence $[J^{tot}_k]$ is used to estimate the values of volatility coefficients χ and α , as discussed next.

4.2 From Experimental Data to Volatility Coefficients

The volatility coefficients χ and α are crucial ingredients, without which comparison between experimental results and simulations of Eq. (2.36) cannot be undertaken. The estimation of the values of χ and α from experimental data is achieved in the following manner. The evaporation rate J^{rate}_k (for time interval $[t_k, t_{k+1}]$), which is estimated from experimental data ($J^{rate}_k = S^{avg}_k J^{tot}_k$), corresponds to the surface integral of $J(h)$ for particular evaporation model. We note that the integral is calculated over the surface recorded in the experiment at time instant t_{k+1} (the experimentally recorded values for H_{k+1} and R_{k+1} describe the spherical cap surface at time t_{k+1}). The validity of the spherical cap approximation has been confirmed by analyzing the experimental images.

The surface integrals of mass flux $J(h)$ are calculated using either expression for $J(h)$ given by Eq. (2.14) in case of “lens” model, or by Eq. (2.33) in case of NEOS model. We note that the divergence of expression for J given by Eq. (2.14) as $h \rightarrow 0$ (or equivalently as $r \rightarrow R(t_{k+1})$), causes singularity of the corresponding

surface integrals. Since we make use of precursor film for our theoretical (numerical) solution of the problem, the use of precursor film of same thickness in calculations of surface integrals of mass flux remedies not only the singularity of integrals for “lens” model, but also ensures that volatility coefficients correspond exactly to the set-up in numerical simulations of Eq. (2.36). In our choice of appropriate value for b , we are guided by the requirement that the mobility of the contact line and the rate of mass loss should not depend on b in any significant manner. We have found that for $d_0 b \leq 0.625 \mu m$ this requirement is satisfied. Coincidentally or not, this value is consistent with the equilibrium adsorbed film thickness $d_0 b_e$ for which evaporation stops due to attracting solid-liquid forces ([2]). For the appropriate parameters, we find $d_0 b_e \approx 0.5 \mu m$. We note that consideration of attractive solid-liquid forces automatically regularizes otherwise singular expression for J in the “lens” model ([66]). Without inclusion of these effects, an additional externally added regularization of J has to be included in order to correctly compute the total mass flux. We capture the presence of the adsorbed film in our experiments using the microscope/high-speed camera set-up, but we do not study its thickness.

The surface integral of the mass flux $J(h)$ (dimensional form) is given as

$$J^{rate}_k = \int_{S_{k+1}} J dS = \int \int_{T_{k+1}} J(\boldsymbol{\rho}) \left[\frac{\partial \boldsymbol{\rho}}{\partial x} \times \frac{\partial \boldsymbol{\rho}}{\partial y} \right] dx dy. \quad (4.2)$$

Here, S_k is the surface of the drop at time t_k . The quantity multiplying $J(\boldsymbol{\rho})$ in the double integral is a Jacobian, where $\boldsymbol{\rho} = (x, y, z)$ and $z = f_k(x, y) = \sqrt{B_k^2 - (x^2 + y^2)}$ — $d_k + b$ is the spherical cap at time t_k . Eq. (4.2) can be rewritten in the following form

$$J^{rate}_k = \int \int_{T_{k+1}} J(f_{k+1}) \sqrt{1 + \left(\frac{\partial f_{k+1}}{\partial x} \right)^2 + \left(\frac{\partial f_{k+1}}{\partial y} \right)^2} dx dy. \quad (4.3)$$

Similar expression for evaporation rate, involving surface integral of mass flux J has been used previously by other authors (e.g., see [15, 33]). On the other hand, in [8, 9, 25, 26, 27, 28, 59] and [61], volatility parameter is calculated from experimental data without using surface integrals of J ; they consider only integrals over circular base of the drop, which are non-singular.

For “lens” evaporation model, Eq. (2.14) is substituted into Eq. (4.3), which is then rewritten in polar coordinates as follows

$$J^{rate}_k = \int_0^{2\pi} \int_0^{R_{k+1}} \frac{J_{exp_k} r}{\left(\sqrt{B_{k+1}^2 - r^2} - d_{k+1} + b\right)^\psi} \sqrt{1 + \frac{r^2}{B_{k+1}^2 - r^2}} dr d\vartheta. \quad (4.4)$$

We note that a different approach is used in [33] in order to overcome the singularity of the integrand: instead of using a precursor film, the kernel $\sqrt{1 + r^2/(B_{k+1}^2 - r^2)}$ is approximated by an expansion, on a semi-empirical basis. We treat J_{exp_k} as constant for each time interval $[t_k, t_{k+1}]$ and finally arrive at expression for J_{exp_k}

$$J_{exp_k} = \frac{S^{avg}_k J^{tot}_k}{2\pi B_{k+1} I_{k+1}}, \quad (4.5)$$

where I_{k+1} is the following integral

$$I_{k+1} = \int_0^{R_{k+1}} \frac{r}{\sqrt{B_{k+1}^2 - r^2} \left(\sqrt{B_{k+1}^2 - r^2} - d_{k+1} + b\right)^\psi} dr, \quad (4.6)$$

which is calculated numerically for each $k = 1, \dots, N - 1$. We can therefore calculate the value of volatility coefficient χ , valid for time interval $[t_k, t_{k+1}]$: $\chi_k = J_{exp_k}/(d_0^\psi J_{sc})$. In order to obtain the value of χ valid for time interval $[t_k, t_{k+l}]$, we simply consider the average of values $\chi_k, \dots, \chi_{k+l-1}$. Finally, since ψ is a function of contact angle Θ , the value of contact angle used in calculating χ is the same as the

value which will be used for solving the Eq. (2.36) numerically. More details regarding the value of Θ are given in Section 4.3.

In the case when NEOS evaporation model is used, Eq. (2.33) is the appropriate expression for $J(h)$. We use a procedure similar to the one described for “lens” evaporation model, and obtain the following surface integral of J (dimensional form)

$$J^{rate}_k = \int_0^{2\pi} \int_0^{R_{k+1}} \frac{J_{sc} d_0 r \sqrt{1 + \frac{r^2}{B_{k+1}^2 - r^2}}}{\sqrt{B_{k+1}^2 - r^2 - d_{k+1} + b + (d_0 (\mathcal{K}(\alpha_k) + \mathcal{W}))}} dr d\vartheta, \quad (4.7)$$

where J_{sc} is the mass flux scale for the problem, defined in Section 2.3, and \mathcal{K} is given by Eq. (2.17). While it was easy to factor J_{exp_k} out of the integral in Eq. (4.4), the same does not hold for $\mathcal{K}(\alpha_k)$ in Eq. (4.7), making the calculation of α_k a bit more complex. A simple manipulation of terms in Eq. (4.7) yields

$$S^{avg}_k J^{tot}_k = 2\pi d_0 J_{sc} B_{k+1} \Xi_{k+1}(\alpha_k), \quad (4.8)$$

where $\Xi_{k+1}(\alpha)$ is the following integral

$$\Xi_{k+1}(\alpha_k) = \int_0^{R_{k+1}} \frac{r}{\sqrt{B_{k+1}^2 - r^2} (d_0 (\mathcal{K}(\alpha_k) + \mathcal{W}) - d_{k+1} + b) + B_{k+1}^2 - r^2} dr. \quad (4.9)$$

The problem of solving for α_k is recast into a minimization problem, where α_k minimizes the function

$$\Gamma(\alpha_k) = \left| \frac{S^{avg}_k J^{tot}_k}{2\pi d_0 J_{sc} B_{k+1}} - \Xi_{k+1}(\alpha_k) \right|, \quad (4.10)$$

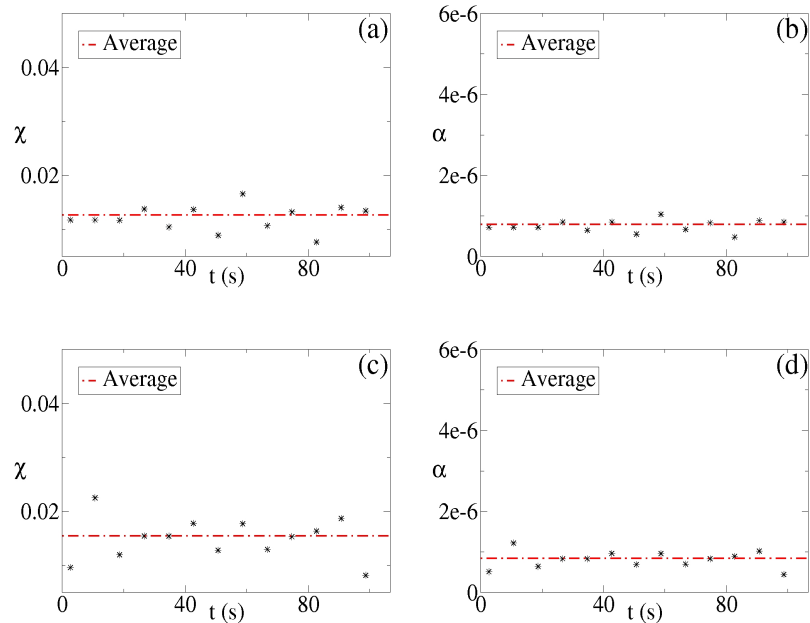


Figure 4.4 Time variation of volatility coefficients for the DIW/Si and DIW/Cu configurations for the first 106.7s. Stars indicate calculated values, dashed lines indicate corresponding average value. (a) DIW/Si, “lens” model: $\chi = (1.3 \pm 0.2) \cdot 10^{-2}$; (b) DIW/Si, NEOS model: $\alpha = (0.8 \pm 0.1) \cdot 10^{-6}$; (c) DIW/Cu, “lens” model: $\chi = (1.5 \pm 0.4) \cdot 10^{-2}$; (d) DIW/Cu, NEOS model: $\alpha = (0.8 \pm 0.2) \cdot 10^{-6}$.

which is solved numerically. Just as it has been the case with χ_k , α_k is valid for the interval $[t_k, t_{k+1}]$. In order to obtain the value of α valid for the time interval $[t_k, t_{k+l}]$, we simply consider the average of values $\alpha_k, \dots, \alpha_{k+l-1}$.

In view of arguments in Section 2.3 regarding ψ , we use $\psi = \lambda$ for DIW/Si configuration, and $\psi = 2\lambda$ for DIW/Cu. Note that the calculation of values of χ for both DIW/Si and DIW/Cu configurations is performed using the expression for λ given in [33].

We expect that the method for calculating volatility coefficients χ and α outlined in this Section is more accurate than simply using the measured dryout time to estimate the mass flux, since at late stages of evolution, evaporation rate may be reduced ([13, 40]).

Figure 4.4 shows the volatility parameters χ and α for DIW/Si and DIW/Cu configurations over a time interval of $106.7s$ (stars). We note that Figure 4.4 shows that, while there is some noise in our experimental data, the values of both volatility coefficients do not exhibit tendency for growth or decay as evaporation proceeds, and remain close to their respective mean values. Small values of α 's are consistent with the values given in [16] and [47], taking into account reasonable possibility of contamination of DIW by surfactants ([47]). The possibility of having very small accommodation coefficient α has also been suggested by other authors (see, e.g. [10]). Therefore, such small values are not surprising, although they are very different from some recent works (e.g. [70]). We note that the values of volatility coefficient χ which we have calculated are consistent with the ones obtained in [27]. The comparison of the calculated values of volatility coefficients for DIW/Si and DIW/Cu configurations indicates good agreement with recent experimental results reported in [11], which suggest that a liquid (DIW) experiences increased volatility on a solid characterized by larger heat conductivity (Cu).

Finally, we ensure the quality of our experimental data through comparison with the experimental results from [33]. In particular, we consider data regarding evaporation of a small water drop on a glass cover slip, with pinned contact line. We apply the same procedure to these experimental data and obtain $\chi = 1.2 \cdot 10^{-2}$ and $\alpha = 0.7 \cdot 10^{-6}$. These values are in excellent agreement with the results for χ and α obtained from our own experimental data. Therefore, we have independent confirmation that our experimental results are reasonably accurate.

4.3 Numerical Simulations, Comparison with the Experimental Results and Discussion

In order to compare the two evaporation models with the experimental results, we perform numerical simulations of Eq. (2.36). We utilize the numerical code developed

in Chapter 3. It is an extension of the one used in [24] to cylindrical geometry. All numerical simulations are performed using thin precursor film of thickness $d_0b = 0.625\mu m$.

The main goal of the present discussion is to point out differences between numerical results for the two evaporation models. Furthermore, by comparing the results to experimental data, we are able to indicate situations in which one evaporation model is more favorable than the other. First, we focus on DIW configurations and perform numerical simulations using volatility coefficients calculated in Section 4. We implement the expressions for λ from both [15] and [33]. Numerical results for evolution of contact line position and volume are compared directly to experimental data, while the results for interface temperatures are compared directly between the two models. Next, we consider IPA configurations and briefly describe the methods used to calculate corresponding volatility coefficients.

4.3.1 DIW Configurations

We perform numerical simulations for DIW/Si configuration using both “lens” and NEOS evaporation model. The simulations are carried out for the time interval for which we have calculated χ and α in Section 4.2 ($[0, 106.7s]$). First, we compare numerical results for evolution of volume and contact line position with the experimental data, in order to establish which evaporation model is more appropriate. Only at this stage, we use both available expressions for λ . We note that the value of χ calculated in Section 4.2 corresponds to use of λ from [33]. In order to utilize the expression from [15], it is necessary to use corresponding value of volatility coefficient. We apply the approach from Section 4.2 and obtain $\chi = 1.16 \cdot 10^{-2}$.

The initial condition for each simulation has the same radius and height as the experimentally measured data for corresponding drop at time $t = 0$ ($R(0) = 2.0695mm$ and $H(0) = 0.692mm$). The initial condition is developed from a spherical

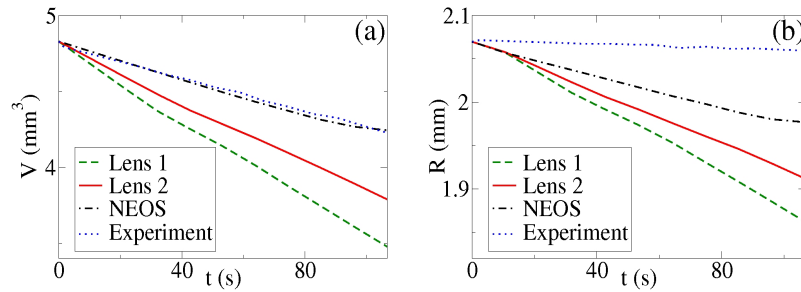


Figure 4.5 Comparison of numerical and experimental results for evaporating drop of DIW on Si substrate. “Lens 1” refers to case when λ from [15] is used; “Lens 2” when λ from [33] is used. (a) Evolution of drop volume; (b) Evolution of contact line position.

cap profile, which has been evolved for a short time with non-volatile version of our code (J set to 0), in order to insure smoothness of the initial profile. The volume corresponding to the initial condition developed in such a way is identical to the experimental volume at time $t = 0$ ($4.828\mu\text{l}$), while the contact angle is slightly larger than the experimental value at time $t = 0$ ($\Theta(0) = 42^\circ$ compared to experimentally measured 39°). Our numerical code makes use of the value for Θ which is identical to the contact angle of the initial profile ($\Theta(0) = 42^\circ$). Same value of Θ has been used in calculating volatility coefficient for “lens” model (χ). The validity of lubrication approximation even for such large values of contact angle Θ has been confirmed in [33].

Figure 4.5(a) shows results for volume of the evaporating drop as a function of time. We find very good agreement between experimental results and NEOS model, while the “lens” model overestimates the volume loss. In fact, it turns out that numerical result for volume of the drop at $t = 106.7\text{s}$ using NEOS model is within 0.4% of experimentally measured volume at the same time. Next, we find that the version of “lens” model which uses λ from [33] does better than the one which uses λ from [15] (within 10.4% compared to within 17.7% from the experimental data for volume at the final time, respectively). In Figure 4.5(b), we present the results for evolution of

contact line position for the three evaporation models and the experimental results for the first 106.7s. This time, the differences between evaporation models are smaller than in Figure 4.5(a). The NEOS model is still in much better agreement with experimental results compared to both variants of “lens” model, but all considered models overestimate the mobility of the contact line. As before, “lens” evaporation model based on [33] does better than the one based on [15]. Judging by the results shown in Figure 4.5, we conclude that at least for the DIW/Si configuration, NEOS model predicts better the volume loss compared to the “lens” model. The same is true for prediction of contact line position, but to a lesser degree. The reason why “lens” model performs worse than NEOS model can be connected to former’s tendency to predict increased mobility of the contact line. Calculation of volatility coefficients in Section 4.2 relies on assumption that the drop maintains spherical cap shape. We suspect that for “lens” evaporation model this assumption may not hold as well as for the NEOS model, due to increased mobility of contact line. This argument will be reexamined later in this section, when we compare temperature profiles for the two models. The results in Figure 4.5 also show that, at least for DIW/Si configuration, “lens” model based on [33] performs better than the one based on [15]. Hence, from this point on, we use only the model based on [33].

We proceed by offering further evidence of significant difference between “lens” and NEOS models. Figure 4.6 shows variation of the drop profile, where identical initial condition is evolved until $t = 106.7s$ using the two evaporation models. It is also of interest to examine the temperature distributions at the liquid-gas interface. Figure 4.7 shows numerical results for temperature profiles at the liquid-gas interface at $t = 106.7s$ for DIW/Si configuration. These results are obtained under the same conditions as the results shown in Figure 4.6. Clearly, the two evaporation models predict qualitatively different temperature profiles at the liquid-gas interface. We recall that the temperature of the liquid-gas interface is determined by the competition

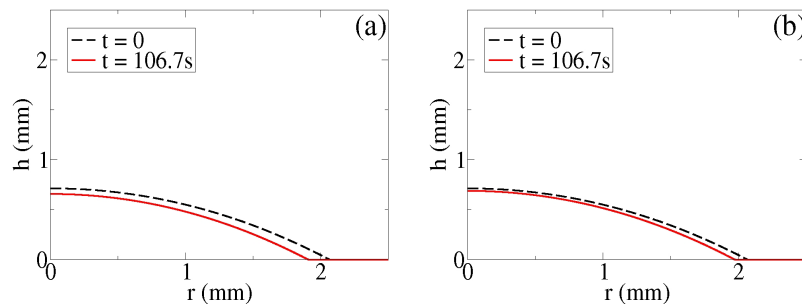


Figure 4.6 Numerical results for evaporating drop of DIW on Si substrate: evolution of drop profile during time interval $[0, 106.7s]$. The initial condition is indicated by a dashed line, while the profile at $t = 106.7s$ is indicated by a full line. (a) “Lens” evaporation model; (b) NEOS evaporation model.

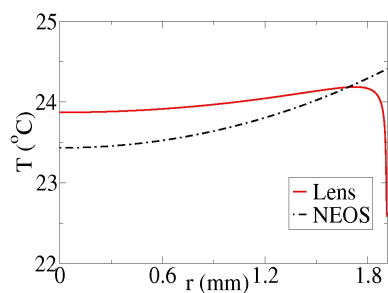


Figure 4.7 Numerical results for DIW/Si configuration: the temperature of liquid-gas interface at $t = 106.7s$ for “lens” and NEOS evaporation models.

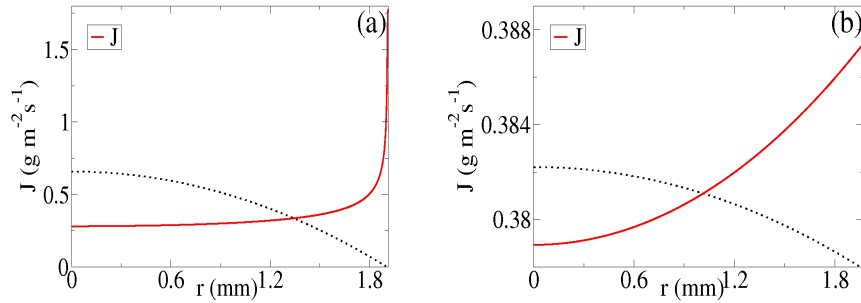


Figure 4.8 DIW/Si configuration: mass flux J as a function of radial coordinate r at $t = 106.7s$. Full lines represent J , dotted lines represent corresponding drop profile $t = 106.7s$. Note that vertical axes correspond to J only. (a) “Lens” evaporation model; (b) NEOS evaporation model.

between thermal conductivity through the liquid and solid, and evaporative cooling. Figure 4.7 shows that the outcome of this competition is very different for the two considered evaporation models. An increase of temperature as one moves from the center of the drop toward the contact line in the NEOS model is the consequence of the fact that the heat supplied from the solid in the contact line region exceeds the heat lost due to evaporation. We note that this result is supported by experimental results reported in [11], where miniature thermocouple was used for measuring interface temperature, and it was found that it is possible for temperature to be highest in the contact line region. Similar conclusion was drawn from experimental data reported in [49], where infra-red imaging technique was used for measuring interface temperature. The “lens” model, on the other hand, predicts significantly larger evaporative flux in the contact line region, leading to a sharp decrease of temperature there. This argument is supported by Figure 4.8, which shows mass flux J at $t = 106.7s$ as a function of radial coordinate r .

An increase of temperature as one moves away from the center of the drop toward the contact line is consistent with the results in [22, 31] and [64], obtained using “lens” evaporation model, and similar values of Θ , and liquid and solid thermal

conductivities, although under the assumption of pinned contact line (and in case of [22], heated solid substrate). However, the results presented in Figure 4.7 for “lens” model predict a ‘stagnation point’ at which temperature gradient changes sign. Although based on different physical grounds, the presence of a stagnation point was discussed in [15] as one of the necessary factors for formation of ring-like deposits occurring during evaporation of colloidal drops. We note that stagnation point in temperature profile disappears as contact angle Θ is decreased. Numerical simulations for “lens” evaporation model for smaller values of Θ lead to monotonically decreasing temperatures along the liquid-gas interface as one moves away from the drop center, in full agreement with the results in [31] and [64]. However, we note that the temperature drop for “lens” evaporation model in Figure 4.7 is $\sim 1^\circ C$, which is much larger than $0.02^\circ C$, reported in [31]. We expect that the reason for such a difference is in the size of drops. From [31] and [33], one finds that at the time when the temperature is reported the volume of the drops is $\approx 0.59\mu l$, therefore much smaller than the volume here. The difference in size translates to significantly larger surface area in our case, leading to larger overall mass loss. In addition, a larger drop implies larger variation in drop thickness between the center of the drop and the contact line, and hence results in larger temperature drop, in view of the dependence of the mass flux J on drop thickness h described by Eq. (2.14). Combination of these factors leads to a possibility that in [31], where the cooling is already smaller than in our case, the liquid thermal conductivity effect starts seriously hampering the cooling effects due to evaporation, to the point where top of the drop (which is further away from the liquid-solid interface) is cooler than the region close to the contact line (closer to the liquid-solid interface), even though the cooling due to evaporation is larger at the contact line. Finally, we note that in Section 2.3, where Eq. (2.14) has been derived, an assumption of small contact angle has been used in order to simplify

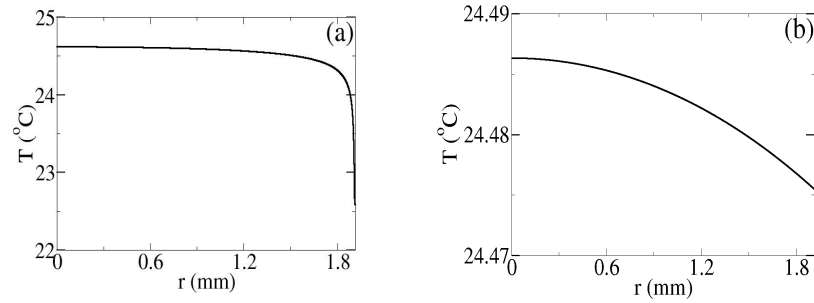


Figure 4.9 Numerical results for DIW/Si configuration: the temperature of liquid-solid interface at $t = 106.7s$. (a) “Lens” evaporation model; (b) NEOS evaporation model.

the complex expression in Eq. (2.13). The fact that we use $\Theta \sim 40^\circ$ here, possibly has some effect on our numerical results.

Figure 4.9 shows numerical results for temperature profiles at the liquid-solid interface for the two evaporation models. We note that the temperature gradients for these two models are in the same direction at this interface. This is in contrast to the liquid-gas interface, where they were oppositely directed (see Figure 4.7).

In order to further analyze the influence of the gas phase on evaporation, we have carried out additional experiments where mild air current is applied externally. Figure 4.10 shows the comparison of experimental results for evolution of J^{tot} and J^{rate} during the time interval $[0, 350s]$ for convection-free ((a) and (b)) and convected ((c) and (d)) configuration. The results shown in Figure 4.10 do not indicate any statistically significant increase in mass flux nor evaporation rate when convection of air is externally applied. This suggests that air convection in the gas does not affect strongly the regime in which evaporation proceeds, at least for the considered configuration. It is clear that convection could increase the rate at which vapor is being removed away from the liquid-gas interface, and as such, it is expected that the evaporation rate should increase if convection is significant. In light of

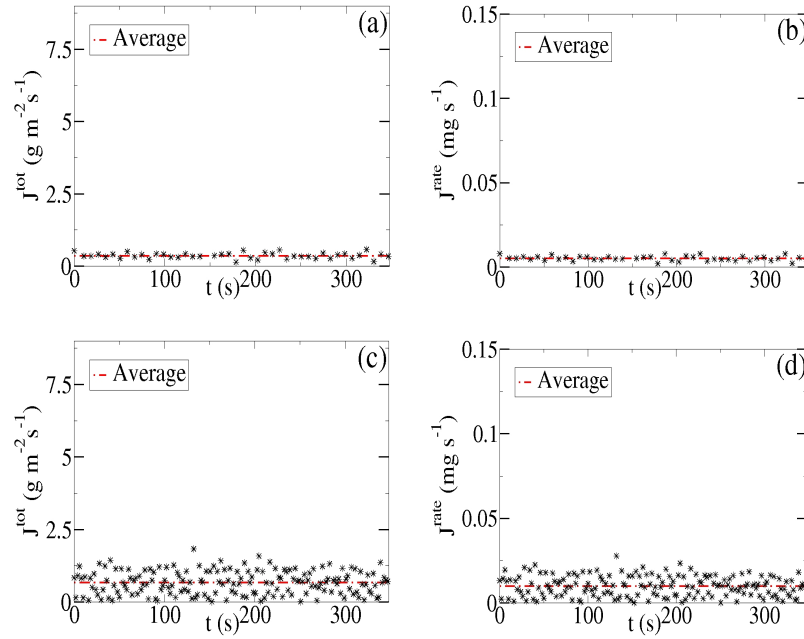


Figure 4.10 Influence of convection on experimentally measured evaporation fluxes J^{tot} and evaporation rates J^{rate} for DIW/Si configuration during the time interval $[0, 350s]$. Stars indicate experimental measurements, dashed lines indicate corresponding average values. (a) convection-free: $J^{tot} = 0.4 \pm 0.1 \text{g}/(\text{m}^2 \text{s})$; (b) convection-free: $J^{rate} = 5.1 \pm 1.4 \mu\text{g}/\text{s}$; (c) convected: $J^{tot} = 0.7 \pm 0.4 \text{g}/(\text{m}^2 \text{s})$; (d) convected: $J^{rate} = 9.5 \pm 5.9 \mu\text{g}/\text{s}$.

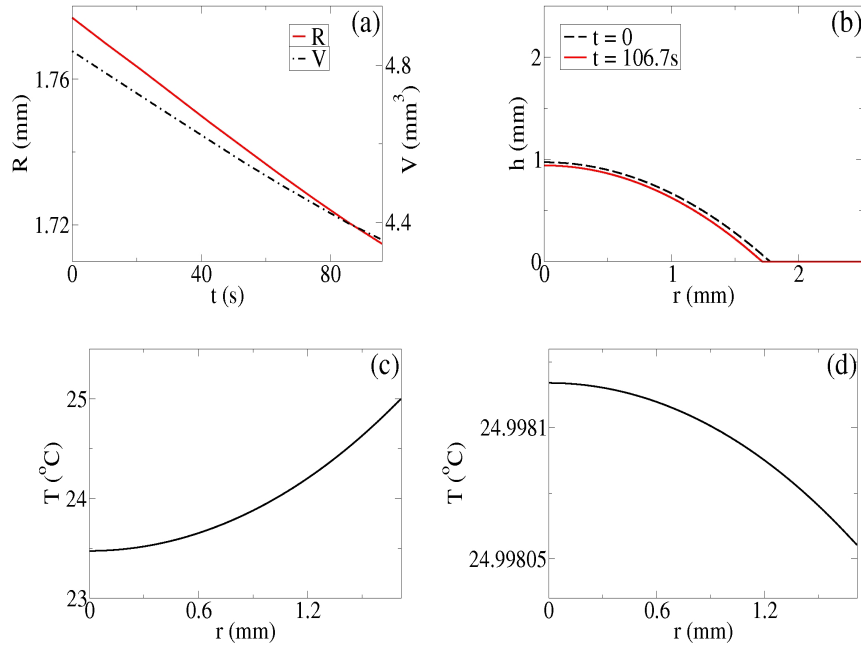


Figure 4.11 Numerical results for DIW/Cu configuration using “lens” evaporation model for the time interval $[0, 106.7\text{s}]$. (a) Contact line position R and volume V of the drop as functions of time; (b) Evolution of drop thickness; (c) Liquid-gas interface temperature at $t = 106.7\text{s}$; (d) Liquid-solid interface temperature at $t = 106.7\text{s}$.

the results shown in Figure 4.10, we conclude that the evaporation rate is rather insensitive to manner in which vapor moves away from the interface, and therefore, that vapor motion (diffusion, convection or combination of the two) is not limiting the evaporation process. Hence, it appears that the NEOS model is more appropriate to describe evaporation of DIW drops on silicon solid wafers ([53]).

Finally, in Figure 4.11, we present numerical results for evolution of drop thickness for for DIW/Cu configuration during the time interval $[0, 106.7\text{s}]$. In light of results for DIW/Si, we focus on NEOS evaporation model exclusively. We use the corresponding volatility coefficient α calculated in Section 4.2, while the initial condition is obtained from experimental data for DIW/Cu configuration. We note that the temperature gradients at both interfaces are qualitatively similar to the ones for DIW/Si configuration. The temperature drop at the liquid-gas interface is slightly larger than for DIW/Si, due to increased thermal conductivity of Cu compared to Si

solid. Hence, the inward flow (from the contact line toward the center of the drop) is somewhat more pronounced in the case of DIW/Cu, resulting in decrease in rate of mass loss when compared to DIW/Si.

4.3.2 IPA Configurations

Next, we apply these two evaporation models to a more volatile IPA drop, evaporating on a Si solid substrate. This configuration is characterized by a small contact angle ($\Theta \sim 6^\circ$). Since the two available expressions for λ become identical as $\Theta \rightarrow 0$, it does not matter which expression we use here. For simplicity, we continue using expression from [33]. Due to small contact angle, in our experiments we are unable to accurately follow the evolution in the manner it was possible for DIW/Si configuration, since the drop quickly becomes very thin. However, we can extract initial profiles and the dryout time with reasonable accuracy. For $V_0 = 3.2\mu l$, we find $t_{dry} = 135s$. We use this dryout time to obtain the required volatility coefficients: $\chi = 4.65 \cdot 10^{-2}$ and $\alpha = 2.5 \cdot 10^{-6}$. As expected, the volatility coefficients in this case are larger than their counterparts for DIW, due to increased volatility of IPA. Similar values of χ were obtained in experiments with pure alkanes in [27]. Implementing these values of χ and α , we perform numerical simulations of Eq. (2.36) using the parameters appropriate for IPA/Si configuration ([24, 44]). The results of numerical simulations are compared qualitatively with experimental results from [9, 25, 27] and [61] for alkanes (hexane through nonane).

The initial condition for our simulations corresponds to an experimentally measured profile soon after the deposition ($R = 3.723mm$, $H = 0.147mm$ and $\Theta = 6^\circ$). Smooth initial condition is developed in the same manner as for DIW/Si configuration. The initial volume in the simulations corresponds to the volume measured in the experiment immediately after the deposition ($3.2\mu l$).

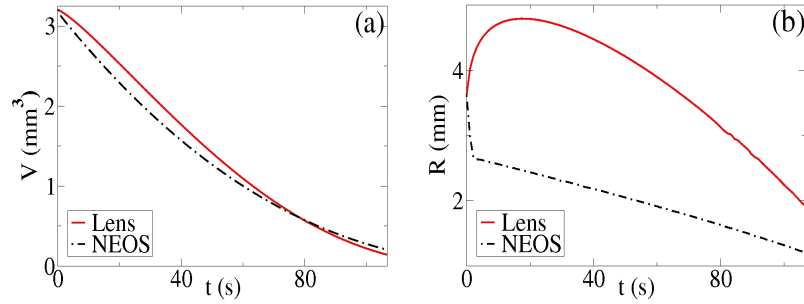


Figure 4.12 Comparison of numerical results for evaporating drop of IPA on Si substrate for “lens” and NEOS evaporation model. Time interval: $[0, 106.7\text{s}]$. (a) Evolution of drop volume; (b) Evolution of contact line position.

Figure 4.12(a) shows numerical results for the evolution of volume for the two evaporation models. The agreement between “lens” and NEOS model does not surprise, since volatility coefficients χ and α have been estimated from experimentally measured dryout time. On the other hand, Figure 4.12(b) shows dramatically different evolution of the contact line position $R(t)$ for the two models, which is discussed below. First, we note that the results for “lens” model in Figure 4.12(b) suggest two distinct phases in the evolution of the contact line position: swift spreading motion initially, followed by even more pronounced receding motion. Qualitatively similar behavior was seen previously in experiments with hexane, heptane, octane and nonane drops ([9]). In addition, in [25] and [61], series of experiments were performed with hexane, heptane and octane drops in order to examine dependence of maximum extent of spreading (R_{max}) on initial volume of the drop (V_0). Initial volumes in the range $[0.01\mu\text{l}, 10\mu\text{l}]$ were examined, and it was found that this dependence follows a power law of form $R_{max} = C_a V_0^{C_b}$, where $C_a \approx 3$ and $C_b = 0.4$ for all considered alkanes. In order to compare our evaporation models against these experimental data, we perform numerical simulation using the same parameter values as before, but now with hemispherical initial conditions ($\Theta(0) = 90^\circ$) of volume $1\mu\text{l}$, $3.2\mu\text{l}$, $6\mu\text{l}$ and $8\mu\text{l}$, and measure the maximum extent of spreading. The hemispherical initial conditions

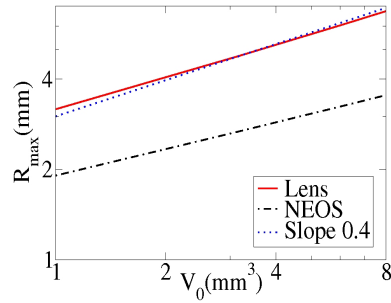


Figure 4.13 Numerical results for IPA drops: Maximum extent of spreading R_{max} as a function of initial drop volume V_0 . Line “Slope 0.4” corresponds to $R_{max} = 3V_0^{0.4}$.

are used in order to simulate more realistically the profiles at time $t = 0$ when the drops are deposited onto the solid substrate. Figure 4.13 compares our numerical results against a power law (the “Slope 0.4” line). It shows that both evaporation models exhibit a power law behavior with exponent ≈ 0.4 . In addition, the results for “lens” model can be fitted almost exactly to $R_{max} = 3V_0^{0.4}$, which is in excellent agreement with the experimental results in [25] and [61].

Motivated by the experimental results in [25] and [61], we use the microscope and high-speed camera set-up (see Chapter 5) to measure the diameter of IPA drops during the spreading stage. A syringe is used to manually deposit $\approx 7.9\mu l$ drops of IPA onto a Si solid, and the position of the contact line during the subsequent spreading motion is being tracked. Our experimental data indicates that the maximum diameter of $\approx 14mm$ is achieved 25s after the deposition. We perform numerical simulations for IPA/Si configuration, using the two evaporation models, in order to compare the numerical results with the experimental data. In order to realistically simulate the spreading motion from the moment of deposition, the initial condition is a hemisphere of volume $7.9\mu l$. The results are shown in Figure 4.14. The maximum radius $R_{max} = 6.72mm$ is achieved in 27s for “lens” model, which is in excellent agreement with the experimental data. On the other hand, NEOS model underestimates the mobility of the contact line.

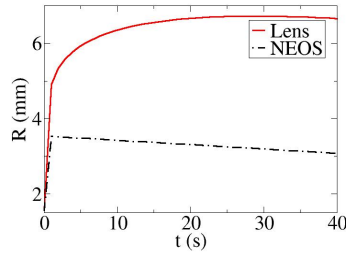


Figure 4.14 The contact line position R as a function of time for IPA/Si configuration using the two evaporation models. The initial condition is a $7.9\mu\text{l}$ hemisphere. $R_{max} = 6.72\text{mm}$ is achieved in 27s for “lens” model.

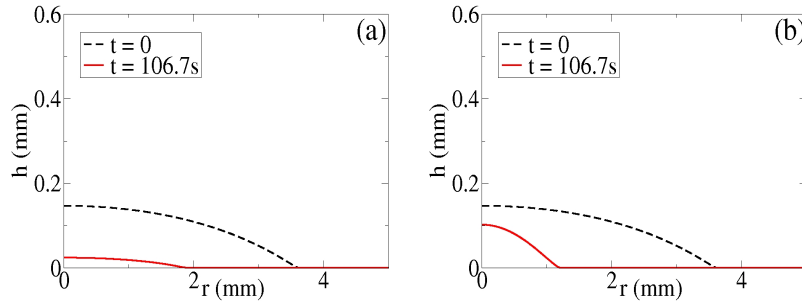


Figure 4.15 IPA/Si: evolution of drop profile during time interval $[0, 106.7\text{s}]$. The initial condition is indicated by a dashed line, while the profile at $t = 106.7\text{s}$ is indicated by a full line. (a) “Lens” evaporation model; (b) NEOS evaporation model.

Based on the results in Figure 4.12(b), it is clear that the drop profiles for the two evaporation models are very different. Figure 4.15 shows corresponding results.

Figure 4.16 shows temperature profiles at the liquid-gas interface for the two evaporation models, and provides immediate understanding of the results in Figure 4.12(b). The Marangoni forces act in opposing directions for “lens” and NEOS models, leading to a very different evolution, as seen in Figures 4.12(b) and 4.15. The Marangoni forces for “lens” model act outwards, leading to initial spreading (see Figure 4.12(b)), in spite of the mass loss due to evaporation. The difference between the temperature profiles for the two evaporation models is much more pronounced

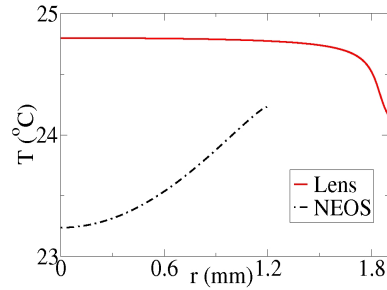


Figure 4.16 IPA/Si: the temperature of liquid-gas interface at $t = 106.7s$ for “lens” and NEOS evaporation model.

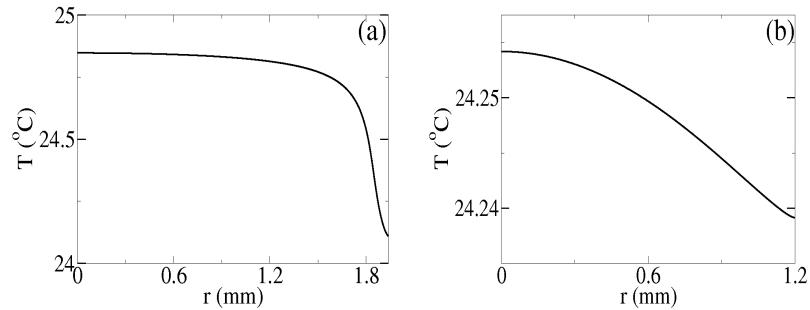


Figure 4.17 IPA/Si: the temperature of liquid-solid interface at $t = 106.7s$. (a) “Lens” evaporation model; (b) NEOS evaporation model.

in the case of IPA compared to DIW, due to its larger volatility. We also note that unlike for DIW, “lens” model for IPA exhibits monotonically decreasing temperatures along the liquid-gas interface. This is due to increased volatility of IPA and smaller value of contact angle Θ , in agreement with [31].

Figure 4.17 shows temperature profiles at the liquid-solid interface for the two evaporation models at $t = 106.7s$. Similarly to DIW configurations, we find that the temperature gradients for the two models are qualitatively alike at this interface, which is in contrast to the gradients at the liquid-gas interface (see Figure 4.16). In addition, Figure 4.17 indicates that the temperature gradient for the “lens” model is much larger than the one for NEOS model.

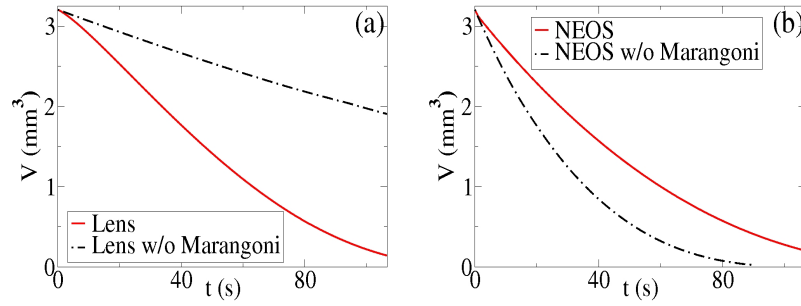


Figure 4.18 Volume evolution for IPA/Si configuration with and without Marangoni forces for time interval $[0, 106.7\text{s}]$. (a) “Lens” model; (b) NEOS model.

Next, we examine more precisely the influence of Marangoni forces on the evolution. For this purpose, we carry out simulations where Marangoni number is $M = 0$. Figures 4.18 and 4.19 show results for time evolution of volume and radius for the two models with and without Marangoni forces. The results in Figure 4.18 confirm that Marangoni forces have significant effect on mass loss for both models. Figure 4.18(a) shows that when $M = 0$ for “lens” model, the rate of mass loss is significantly decreased. On the other hand, for NEOS model, $M = 0$ causes the increase of evaporation rate, as shown in Figure 4.18(b). Exclusion of Marangoni forces, in general, reduces mobility of the contact line for “lens” model (Figure 4.19(a)): it completely suppresses initial spreading, and reduces the amount of receding motion. Figure 4.19(b) shows that for NEOS model, exclusion of Marangoni forces prevents initially swift receding motion.

For “lens” model, Marangoni forces enhance initial spreading, with the particularly strong outward flow in the region close to the contact line, due to large temperature gradient there (see Figure 4.16). The Marangoni induced outward flow in a region closer to the center of the drop is less pronounced and therefore cannot keep up with the fast flow close to the contact line. As a result, the liquid in the vicinity of the contact line is being propelled outward, forming a thin ‘stretching’ layer, which spreads faster than the bulk drop and ‘extends’ the contact line region.

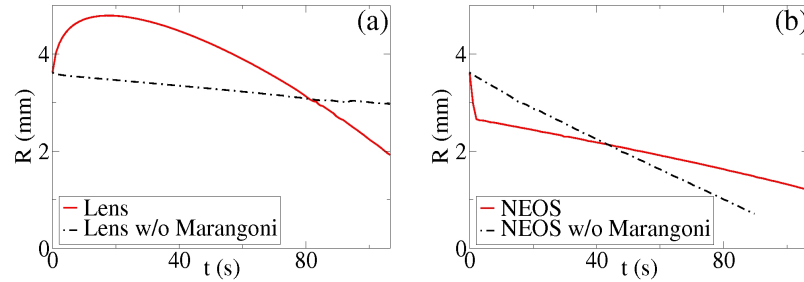


Figure 4.19 Radius evolution for IPA/Si configuration with and without Marangoni forces for time interval $[0, 106.7s]$. (a) “Lens” model; (b) NEOS model.

Figure 4.20 shows several drop profiles for the early (spreading) stage of the evolution ($[0, 10.67s]$) for “lens” evaporation model with $M \neq 0$. The stretching of the contact line region, which enhances mass loss, is clearly visible. Initially, the liquid lost from the ‘super’-volatile thin zone is being successfully replenished by the liquid from the bulk, and the spreading continues. At some stage of spreading, the liquid being lost in the stretching zone cannot be replenished any more, and due to ensuing mass loss, the receding phase sets in. When Marangoni forces are neglected, no spreading occurs, as shown in Figure 4.19(a). Without the described thin stretching layer, which accounts for the largest portion of mass loss, evaporation rate declines sharply, as shown in Figure 4.18(a). The receding motion is entirely due to mass loss, and therefore the decrease in evaporation rate causes slower receding motion.

For NEOS model, the Marangoni forces act in the opposing direction compared to the “lens” model (see Figure 4.16). Also, the temperature gradient is uniform, unlike for “lens” model, where it is compressed to a region close to the contact line. Therefore, the Marangoni induced flow along liquid-gas interface is inward and uniform. It causes rapid receding motion shown in Figure 4.19(b). As a result, the surface area of the drop is decreased, while the drop thickness is increased. The rate of mass loss is therefore smaller, due to dependence of the mass flux J on drop thickness h (see Eq. (2.33)). We note that this dependence is rather weak, as discussed in

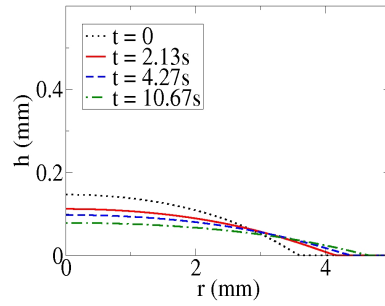


Figure 4.20 IPA/Si: the evolution of the drop thickness for time interval $[0, 10.67s]$ for “lens” evaporation model.

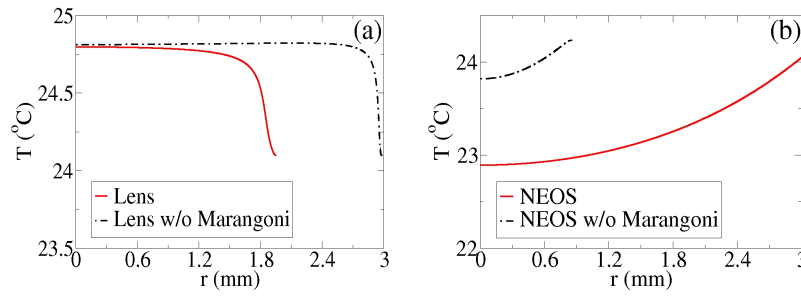


Figure 4.21 Liquid-gas interface temperature for IPA/Si configuration with and without Marangoni forces. (a) “Lens” evaporation model at $t = 106.7s$; (b) NEOS evaporation model at $t = 86.7s$ (\approx dryout time for NEOS model with $M = 0$).

Section 2.3. When $M = 0$, the swift initial receding motion is suppressed, as shown in Figure 4.19(b). This prevents the decrease of surface area and the increase in drop thickness. The resulting evaporation rate is increased compared to $M \neq 0$. The main driving mechanism for receding motion of contact line is mass loss, and therefore, when $M = 0$, the overall extent of receding motion is larger compared to $M \neq 0$.

Figure 4.21 shows temperature profiles at the liquid-gas interface for the two models with and without Marangoni forces. Qualitatively, the temperature gradients are not affected by exclusion of Marangoni effects. The quantitative differences, which are especially pronounced in Figure 4.21(b), are simply due to the effects that Marangoni forces have on both the contact line motion and the evaporation rate.

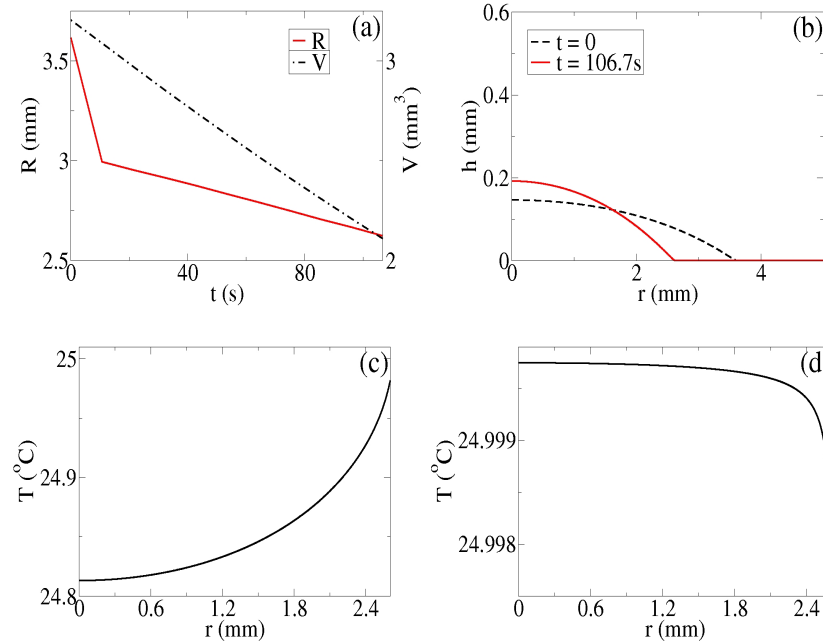


Figure 4.22 Numerical results for IPA/Cu configuration using “lens” evaporation model for the time interval $[0, 106.7s]$. (a) Contact line position R and volume V of the drop as functions of time; (b) Evolution of drop thickness; (c) Liquid-gas interface temperature at $t = 106.7s$; (d) Liquid-solid interface temperature at $t = 106.7s$.

In view of results presented thus far, we conclude that “lens” evaporation model performs better than NEOS model in situations when more volatile liquid (e.g. IPA) is considered. Such a conclusion is not surprising. First, Biot number for IPA/Si ($Bi \sim 10^{-1}$) is an order of magnitude larger than the one corresponding to DIW/Si case ($Bi \sim 10^{-2}$), making the $Bi \rightarrow 0$ limit (reaction-limited regime) less applicable for IPA/Si ([53]). Furthermore, increased volatility in case of IPA translates into increased vapor production. Finally, the density of IPA vapor is twice larger than the one for DIW, possibly hampering the rate at which vapor is being removed away from the evaporating interface. Combination of these factors may lead to evaporation which proceeds in the diffusion-limited regime instead of reaction-limited one, typical for NEOS model.

Finally, we also show results of numerical simulations for the IPA/Cu configuration in Figure 4.22. We focus on the “lens” model, which has been shown so far

to be more appropriate for IPA/Si case. The volatility parameter $\chi = 0.6 \cdot 10^{-2}$ and the contact angle $\Theta = 9^\circ$ which we use here are estimated from our experiments with the IPA/Cu configuration. The initial condition is obtained using the same procedure as in the case of IPA/Si configuration, and the simulations are performed for the time interval $[0, 106.7s]$. Figure 4.22(a) shows the time evolution of drop radius R and volume V . We find that the motion of the contact line is strictly receding, in contrast to the results obtained for IPA/Si-“lens” configuration. In addition, the overall mass loss during the given time interval is smaller than for the IPA/Si case (see Figure 4.12). Figure 4.22(b) shows how these two factors influence the drop profile at time $t = 106.7s$. The explanation for such a behavior is supplied by Figure 4.22(c), which shows that the temperature gradient at the liquid-gas interface is directed in the opposing direction when compared to IPA/Si configuration (see Figure 4.16). This change is caused by increased thermal conductivity of Cu substrate when compared to Si: $(k_s/k)_{IPA/Cu} \sim 10^3$ compared to $(k_s/k)_{IPA/Si} \sim 10$. Therefore, our results are in agreement with the results in [64], where a study of the contact line region was performed using asymptotic methods, and it was found that the drop is warmest at the contact line when the ratio k_s/k is large. As a result, the Marangoni flow along the liquid-gas interface is directed from the contact line toward the center of the drop. This enhances receding motion of the contact line, reduces the surface area of the interface, and hence, reduces the rate of mass loss.

CHAPTER 5

INSTABILITIES OF EVAPORATING FILMS AND DROPS

We devote this chapter to “octopus”-shaped instabilities which occur ahead of the contact line of evaporating IPA drops on Si solids substrates, and related instabilities which occur for volatile IPA-DIW mixtures. We start with the description of “octopi” experiments which have been performed by our collaborators and served as a motivation for this work. We proceed by presenting our own experimental data concerning “octopi” and other interesting instabilities. Finally, we conclude with theoretical exploration, involving linear stability analysis (LSA) and numerical simulations of Eqs. (2.35), (2.36) and (2.37) using the numerical codes from Chapter 3 and the evaporation models from Chapters 2 and 4, with an intention of gaining a better understanding of the mechanism responsible for these instabilities and recovering their main features.

5.1 Octopus-shaped Instabilities: Initial Experiments

The initial experiments were conducted at KLA-Tencor, San Jose, California. The drops of IPA or IPA-DIW mixtures of a typical size of $30 - 50mm^3$ are deposited on wafers of monocrystalline Si of thickness $0.75mm$ ([24]). The wafer surface is either bare or coated with copper (Cu) film. All of the materials used are of semiconductor grade quality. The solid surfaces are treated by chemical-mechanical polishing, producing surface roughness (rms) of $0.5nm$ for Si and $1nm$ for Cu surfaces ([24, 54]). The measurements were performed under clean room conditions at $25^\circ C$, using a Sony AL 100M microscope with a video camera attached to it. It has been verified that possible heating of the surface by microscope illumination does not influence the results ([24, 54]). Additionally, the presence of the microscope does not influence the

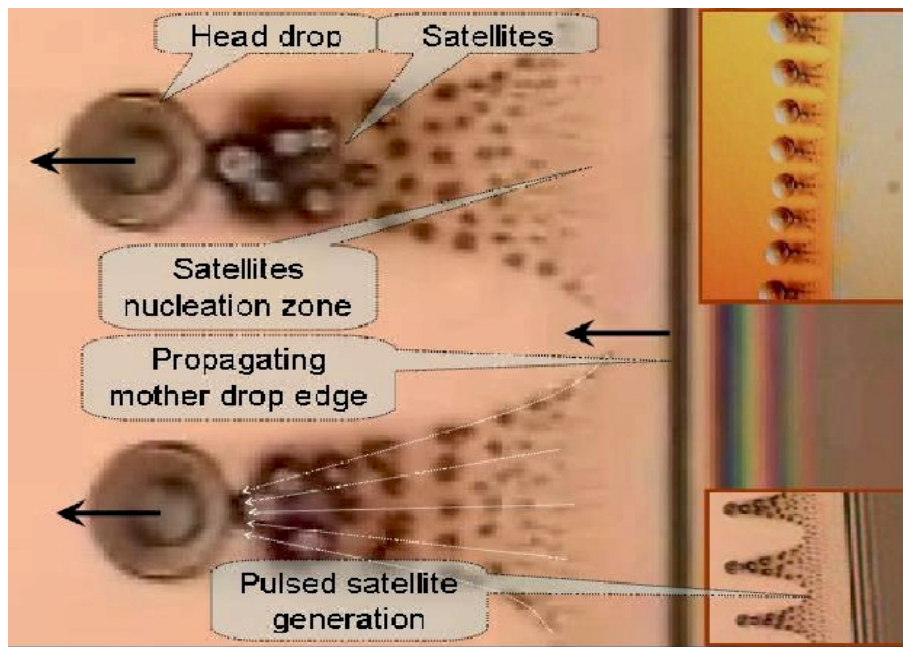


Figure 5.1 Formation of “octopi” during spreading of IPA on Si surface ([24]). The bands on the right-hand side are due to Newton interference fringes. White arrows indicate the path of the satellites. On the scale shown ($\approx 200 \times 300 \mu\text{m}$) the azimuthal curvature of the (mother) drop is invisible. The insets show uniformity of the “octopi” (top inset) and synchronous pulse-like emission of satellites (bottom inset).

state of the gas phase in the vicinity of liquid-gas interface. The temperature of the solid is not set, and is allowed to vary during the drying process.

Figure 5.1 illustrates the experimental observation, which is one of the motivations for this work. As a (mother) drop of IPA is deposited on a surface, it expands and ejects fluid ahead of its front. This material nucleates into smaller (head) drops all around its perimeter, followed by smaller (satellite) drops which travel along the paths already traversed by the head drops. These structures (nicknamed “octopi” since the head drop appears as an octopus body and streams of satellite drops as several tentacle arms) occur just for a particular liquid-solid configuration and belong in turn to a wider family of patterns which may form in evaporative systems ([24]). The octopi appear to be separated from the mother drop, bear no similarity to phenomena of droplet formation by re-condensation, and occur only for a pure surfactant-free

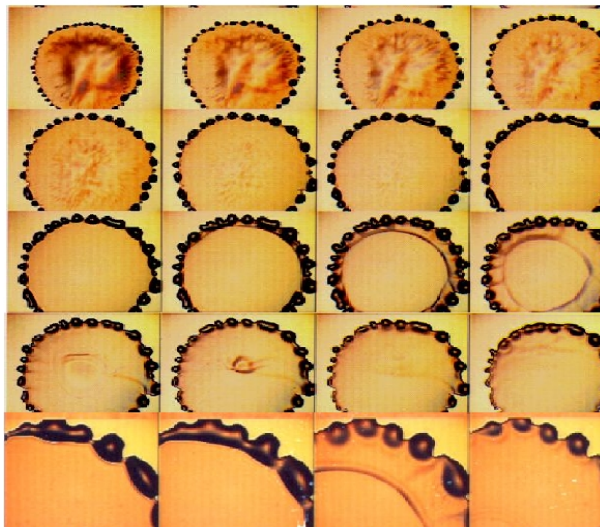


Figure 5.2 Spreading of 1:1 mix of DIW and IPA ([24]). Drop size is approximately $5mm$. The darker color indicates increased fluid thickness. Time progresses left to right and top to bottom, with the interval between the images $\approx 1.5s$. The bottom row illustrates the merge of individual cells just prior to wave generation (close to image 10). Note formation of radial ridges during early stages of instability development.

liquid. What further distances these instabilities from previously described types and makes them unique thus far, are features such as complexity of the octopi and the fact that they appear to function as a single object while actually consisting of multiple but disconnected parts.

Figure 5.1 shows “octopi” formation, which occurs (only) for one of the four configurations considered (two liquid and two solid types), and that is an IPA drop on Si surface. The “octopus”-shaped patterns are robust and have occurred consistently in all experiments involving this liquid-solid combination ([24]). During the initial period after deposition, the drop front spreads, the drop quickly reaches the thickness of few fractions of a millimeter, and the fluid is ejected through the front, forming the head drops spaced regularly around the perimeter. Behind the head drops, satellites propagate, which are either emitted by the front itself or nucleated at some distance

ahead. These satellites increase in size by merging and/or picking up some material from the prewetted trail left by the head drops. This prewetted trail leads to faster motion of satellites and to their focusing toward the head drops. It seems likely that both effects are due to enhanced satellite motion on this prewetted trail. Eventually, the satellites catch up with the head drops and merge, returning the mass and kinetic energy lost to the interaction with the substrate, formation of prewetted trail, and evaporation ([24]). This eventually leads to perhaps surprising fact that the head drops move with exactly the same speed as the drop front itself. Therefore, the structures shown in Figure 5.1 are steady in the moving frame translating with the speed of the front ([24]). Note that the satellites are often generated in temporal pulses during which a radial wave of satellites is emitted all around the perimeter (viz. Figure 5.1, lower inset). A possible explanation of this effect can be reached by considering IPA-DIW mixture, discussed in what follows.

So far, the attention has been focused on the first, expanding part of the drop evolution. This part, which lasts $\approx 40-50s$, is followed by contraction phase ($\approx 5-7s$) during which the remaining film quickly retracts toward the center, evaporating and disintegrating into multitude of swiftly evaporating micro-droplets. The head drops move forward for a while longer, and then stop. The fact that the “octopi” do not retreat together with the film edge additionally shows that there is no physical link between the “octopi” and the mother drop.

The spreading of IPA-DIW mixture drops also leads to instabilities, but of different types. Figure 5.2 shows that in case of 1 : 1 mixture, the drop front develops unsteady patterns (cells). At some stage of evolution, the individual cells start to converge and form a peripheral ridge (viz. the bottom row of Figure 5.2). This ridge propagates or collapses toward the center of the drop and then rebounds inducing global oscillatory motion. A similar effect is expected to be responsible for global synchronous emission of satellites for pure IPA drop. It is important to note that

propagation of the waves across the drop surface may lead to a variety of effects, including formation of dry spots.

5.2 Literature Review

The problem of stability of evaporating thin films has been under continuous attention of scientific community for the past three decades, with abundance of experimental results becoming available only recently due to the advancement of nano-technology, and other areas of possible application. It has become apparent that certain advanced nano-devices are very sensitive to the residues, called watermarks, which appear on the semiconductor wafer surfaces when liquid micro-drops or thin films are left to dry. The formation of watermarks has been analyzed (e.g. see [14, 23]), however the clarification of their origin is still lacking. This particularly refers to settings which are relevant to industrial applications ([62]). Additional features, such as the formation of dry spots resulting from film integrity breakage, are of considerable relevance as well, and these have often been connected to various hydrodynamic instabilities which occur in evaporative films ([23]).

Curiously shaped instabilities, appearing close to the contact line of volatile drops, have been reported previously. Note that the “octopus” shapes, which are the focus of the attention, appear to be separated from the mother drop. In contrast, most previously observed patterns, such as “festoons” ([63]), “fingers” ([8, 23]), or the drops in electric fields ([52]), are connected to the main fluid body. Furthermore, the instabilities reported here are clearly very different from the droplet formation which results in re-condensation ([59]). Also notice that “octopus” shapes appear for pure liquids, in contrast to instabilities in the presence of surfactants ([50]).

Possible mechanism which explains the early phase of the drop evolution, where satellites are accelerating along the prewetted trail and focusing toward the head drops has been introduced in connection to controlling instabilities arising in

thin film flows ([43]). The formation of ridges which is observed for configurations involving both IPA and its mixtures, has been reported in connection to thermally driven thin films, where temperature difference along the solid has been imposed ([37]). The ridges have been reported to collapse toward the center of the drop and then rebound, inducing global oscillatory motion ([38]).

5.3 Experiments Carried Out at NJIT

Motivated by the experiments described in Section 5.1, we set out to perform similar experiments, using solid wafers supplied by our collaborators. The experiments are carried out in the Capstone Laboratory of the Department of Mathematical Sciences, NJIT. The recording equipment consists of Photron 1024PCI high-speed camera mounted on top of Nikon Eclipse LV100P polarizing microscope, so that a view from the top is established and microscope's mobile stage allows for accurate tracking of the contact line. Two different magnifications are used: 20x which provides a $2.5mm \times 1.75mm$ viewing window, and 40x which provides a $0.6mm \times 0.4mm$ view. All experiments are performed in room conditions ($1atm$, 50% relative humidity, $25^\circ C$). Volatile drops of initial volume of $\approx 8\mu l$ are deposited onto a solid substrate manually, using a Hamilton gas-tight syringe. The set up is shown in Figure 5.3.

Series of experiments are performed in a short time span of only a few hours, with each experiment repeated multiple times. Various liquid-solid combinations were examined. The liquids used were either aqueous solution of IPA, with varying IPA content (70% IPA or 91% IPA), or pure semiconductor grade IPA. The substrates which we use are either semiconductor grade silicon wafers (thickness $0.5mm$, surface roughness $0.5nm$) or plain microscope glass slides (thickness $1.1mm$, pre-cleaned). The temperature of the substrate is not controlled.



Figure 5.3 The microscope/high-speed camera set-up.

A collage of movie files presenting the most interesting features of these experiments has been showcased in [55]. We note that a larger collection of movie files of the experiments, along with numerous images can be viewed at [1].

First, we show several results where the solid type is fixed, while IPA-DIW mixtures of varying IPA content are used. We intend to show how change in concentration of the more volatile component in the mixture influences the size and shape of instabilities which occur at the contact line. The solid is a glass slide.

Figure 5.4 shows the beautiful mushroom-shaped instabilities which occur when a drop of 70% IPA mixture spreads on a glass slide. The view is $2.5\text{mm} \times 1.75\text{mm}$. The mushroom-like features appear uniformly (both in size and shape) along drop's perimeter. Figure 5.4 shows an early stage in evolution. As the drop spreads, neighboring mushroom-like features coarsen and form larger and larger mushroom heads. Eventually, as spreading subdues, remaining large mushroom heads collide to form a perimeter ring. Figure 5.5 shows the typical instability which occurs when concentration of IPA in the mixture is increased to 91%. The size of the features which

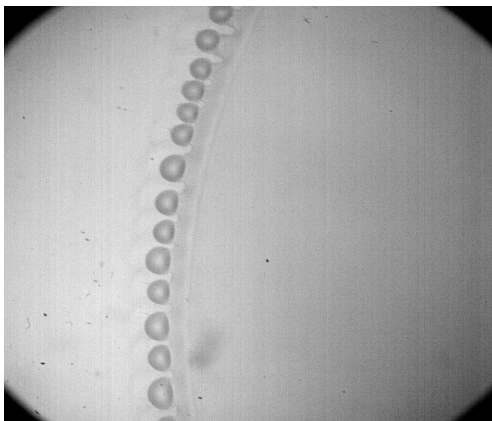


Figure 5.4 $2.5\text{mm} \times 1.75\text{mm}$ viewing window: spreading of a drop of 70% IPA mixture on a glass slide.

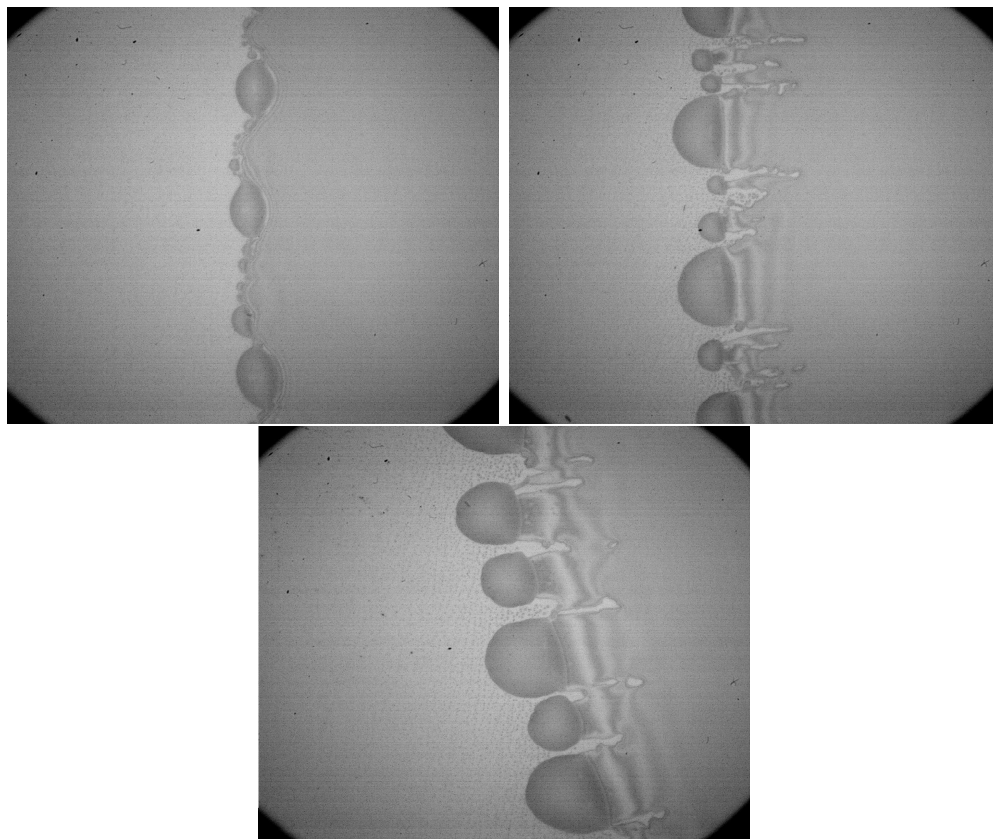


Figure 5.5 $0.6\text{mm} \times 0.4\text{mm}$ view: three distinct stages in spreading of a drop of 91% IPA mixture on a glass slide. The time progress is shown left to right and top to bottom.

appear at the contact line is now significantly smaller when compared to mushroom-shaped instabilities in Figure 5.4. The view in Figure 5.5 is hence reduced to 0.6mm x 0.4mm . In addition, the increase of IPA content causes more rapid spreading. At first, bumps of various sizes appear on (and not ahead of) the contact line, as can be seen on the top left picture in Figure 5.5. Soon, as the spreading continues, the film between neighboring bumps ruptures, which is seen in the top right picture in Figure 5.5. These bumps then break away ahead of the contact line, becoming either mushroom-like (bottom picture in Figure 5.5) or finger-like patterns of wide range of sizes, all smaller than the features seen in Figure 5.4. Neighboring patterns do not coarsen as before, but instead a ridge forms along the perimeter of the drop, some distance behind. As the spreading of the main body of drop stops, the patterns continue their forward motion for a short while. Eventually, as this forward motion subdues, rupture occurs in the thin valley behind the ridge, leaving the patterns stranded as the main body of the drop recedes in a dramatic fashion.

Finally, as concentration of IPA increases to 100% (Figure 5.6), the nature of the instability changes yet again. The size of the features is similar to those in Figure 5.5 and smaller than those in Figure 5.4. The view is 0.6mm x 0.4mm . Small comet-like circular objects appear ahead of the spreading contact line (top pictures in Figure 5.6). These are mostly uniform in shape and size along the perimeter, and, from the very start, each appears to be connected to the main body of the drop only through a very narrow tail, which becomes less visible as spreading motion proceeds. Eventually, as the spreading of the main drop stops, the comet-like objects are pushed some distance ahead of the contact line (bottom picture in Figure 5.6), lose their tails completely, and remain stranded as the main body of the drop shrinks to complete dry-out.

The recording of images in figures shown in this section requires tracking of the contact line position. Although this tracking is performed with an utmost care, we

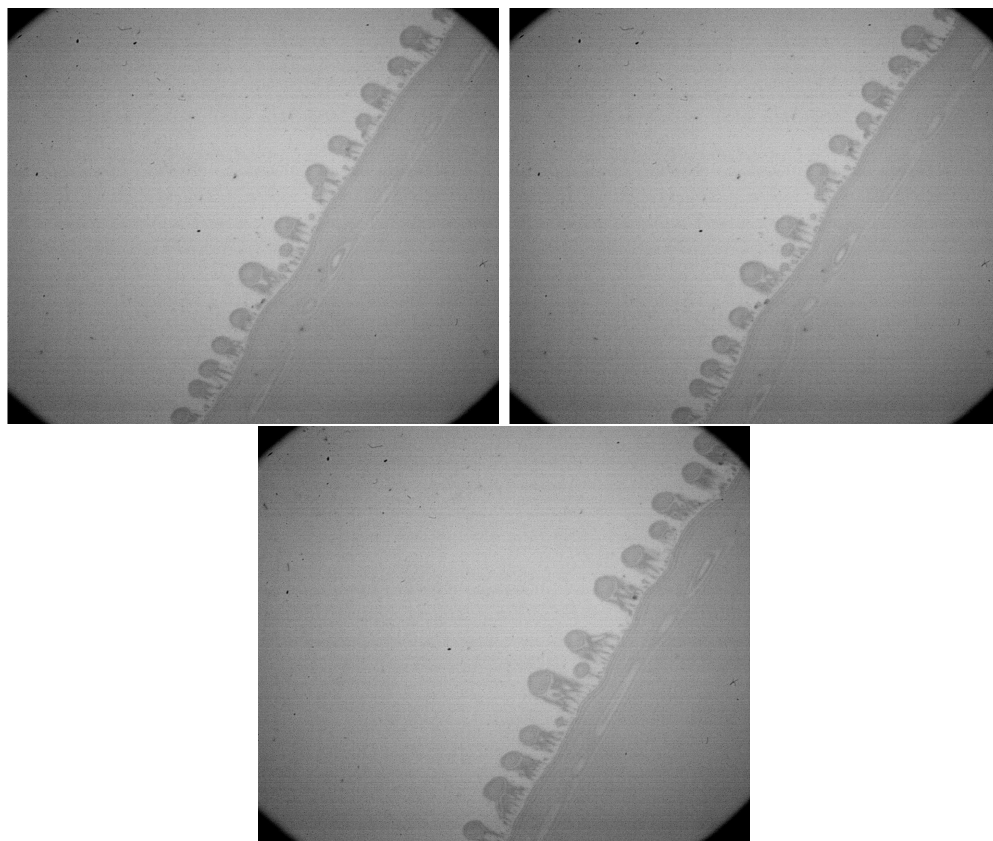


Figure 5.6 $0.6\text{mm} \times 0.4\text{mm}$ view: the spreading of a drop of pure IPA on a glass slide. The time progress is shown left to right and top to bottom.

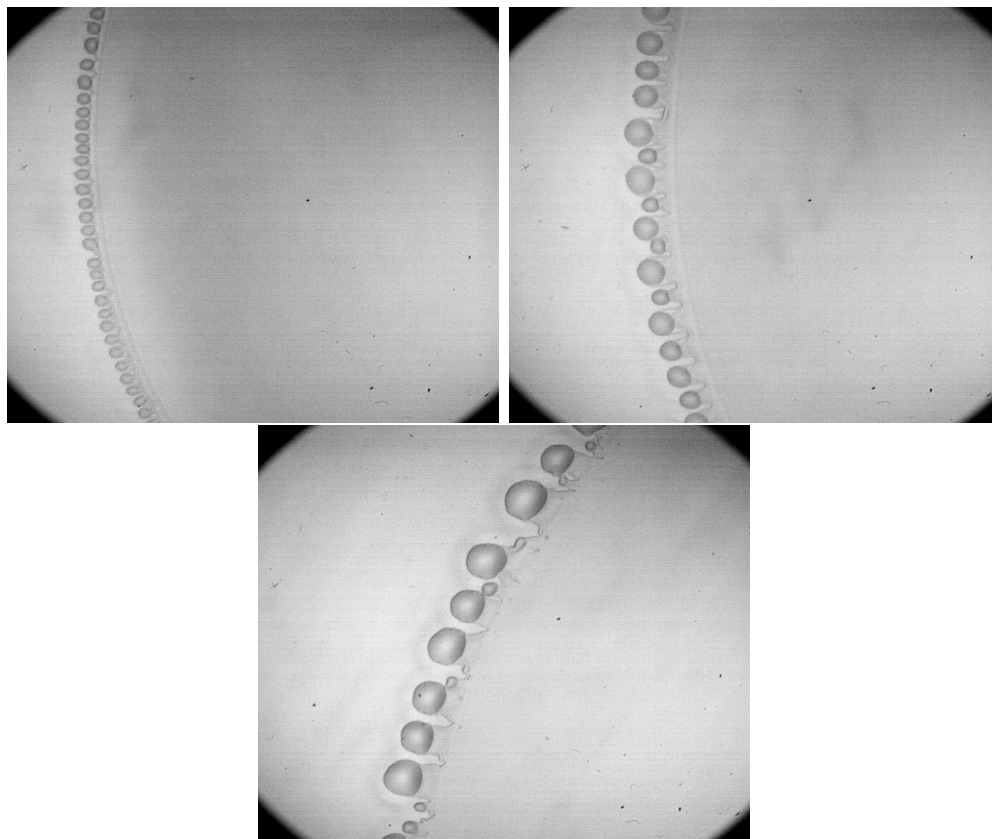


Figure 5.7 $2.5\text{mm} \times 1.75\text{mm}$ viewing window: spreading of a drop of 70% IPA mixture on a glass slide, with externally induced convection in the gas phase.

are concerned that the motion of the microscope stage in order to follow the spreading motion of a drop disturbs the gas phase above. Therefore, we perform an experiment with 70% IPA mixture on a glass slide, where we introduce external air current in order to examine the sensitivity of the size and shape of the instabilities on convection in the gas phase. Mild air current is provided using a ventilator. The results are shown in Figure 5.7. Even though the convection is applied, the evolution proceeds in a manner similar to the situation where no external convection is considered. The mushroom-shaped instabilities which occur are identical in size, shape and distribution to the instabilities shown in Figure 5.4. In addition, the evaporation rate is not altered in any significant manner. We conclude that, at least for this specific configuration (70%

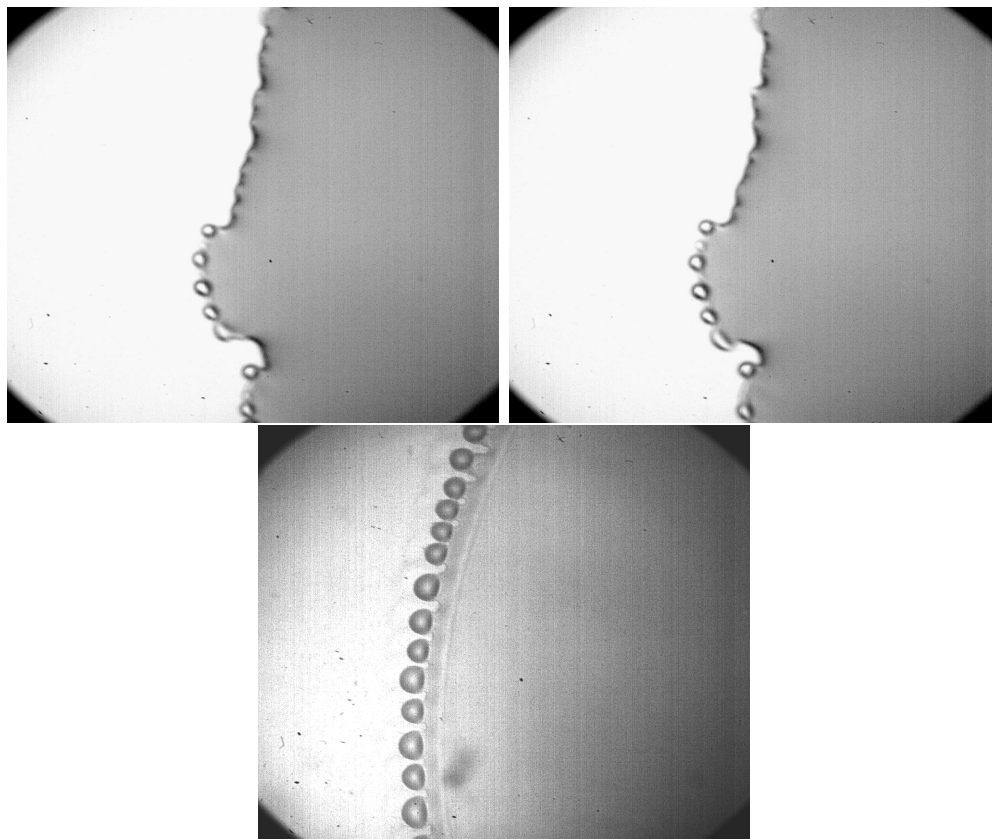


Figure 5.8 $2.5\text{mm} \times 1.75\text{mm}$ viewing window: spreading of a drop of 70% IPA mixture on a Si wafer.

IPA mixture on a glass slide), convection in the gas phase does not play a significant role on the dynamics of drop spreading.

Next, we focus on Si solid and perform a similar study, where influence of IPA concentration in mixtures on the size and shape of the instabilities is examined. The most significant difference between Si wafers and glass slides is surface roughness. We begin with 70% IPA mixture. The results are shown in Figure 5.8. The spreading of the drop is less rapid than in case when glass slide is considered, and we are able to capture the early stage of instability formation. This fascinating beading process (pictures on top in Figure 5.8) occurs in isolated zones ahead of the expanding contact line. The beads appear simultaneously in quartets, quintets or sextets and eventually grow into mushroom-like features, resembling those from Figure 5.4 (bottom picture

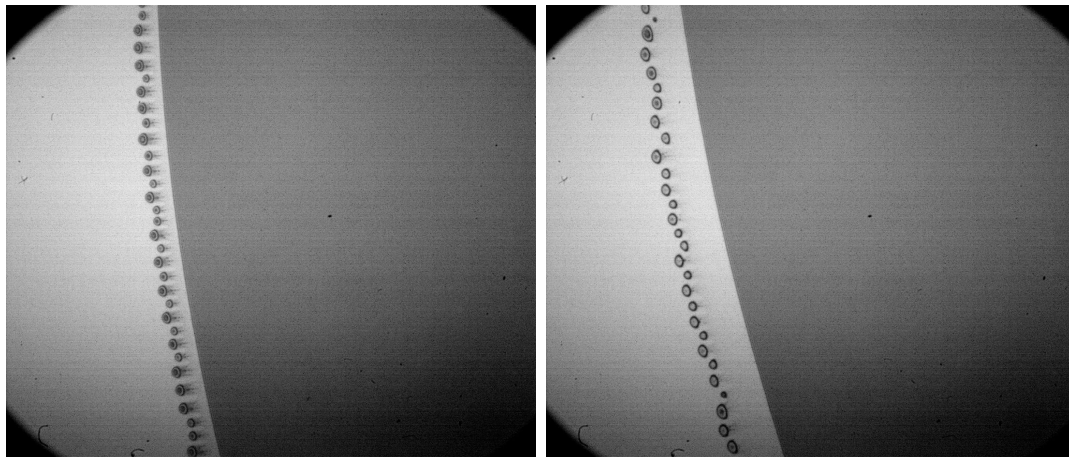


Figure 5.9 $0.6\text{mm} \times 0.4\text{mm}$ viewing window: spreading of a drop of pure IPA mixture on a Si wafer. Notice the “octopus” shaped instabilities similar to the ones in Figure 5.1.

in Figure 5.8). These mushrooms are not uniform and grow in a variety of shapes and sizes. Neighboring mushrooms interact and coarsen to form larger mushrooms, making the late stages of this process similar to those for the case when glass slide is used. Next, we increase the IPA content in the mixture to 91%. The evolution proceeds in a manner which is indistinguishable to the one described for same liquid on a glass slide. Hence, we omit these results and move on to pure IPA drops spreading on Si wafers. The results are shown in Figure 5.9. Elliptical objects appear ahead of the contact line of a spreading drop. These objects are smaller than the ones seen in other figures in this section, and appear to be perfectly uniform in both size and shape. A steady stream of smaller satellite drops (several tentacle arms) connects each elliptical head to the main body of the drop. The appearance of these objects is identical to “octopi” captured in the experiments described in Section 5.1, showing the robustness of this instability process. As before, the neighboring “octopi” do not coarsen, and, as spreading continues, they maintain uniform distance ahead of the contact line (the picture on the left in Figure 5.9). As the spreading motion of the main drop is brought to a halt, the “octopi” continue spreading ahead of the contact line a while longer (the picture on the right in Figure 5.9).

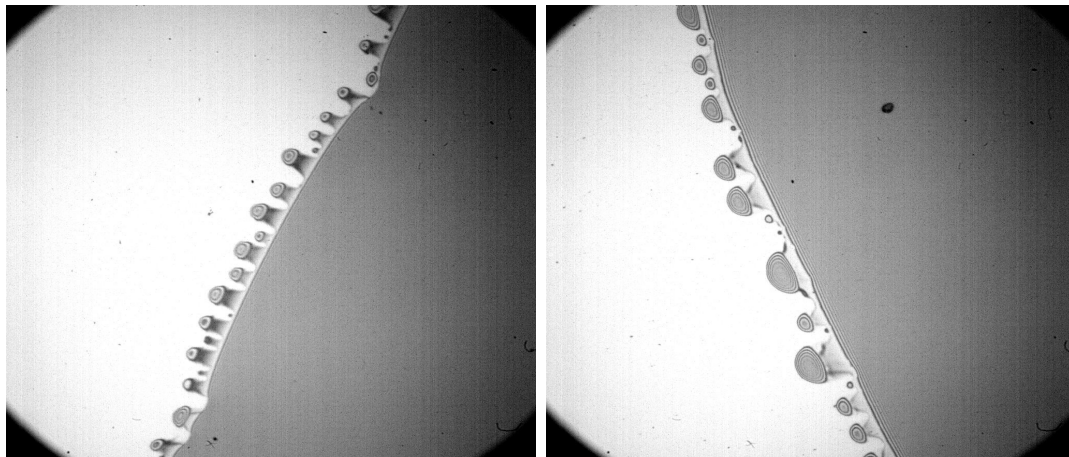


Figure 5.10 $0.6\text{mm} \times 0.4\text{mm}$ viewing window: spreading of a drop of pure IPA mixture on a Si wafer in an enclosed environment (saturated gas phase).

Finally, we examine the influence of the saturation of the gas phase on the appearance of “octopi”. For this purpose, we perform experiments with spreading drops of pure IPA on a Si wafer in an enclosed environment heavily doped with IPA vapor. The results are shown in Figure 5.10. Although the saturation of the gas phase has some influence on the evaporation rate, the “octopi” still appear, and their dynamics are in many ways identical to the case when experiment is performed in open air. One noticeable difference is in the size of “octopi”, which appear to be somewhat larger than before, and exhibit slight non-uniformity in shape and size (see picture on the right in Figure 5.10). Our discussion in Chapter 4 suggests that the “lens” evaporation model is more appropriate for IPA/Si configuration. The situation where gas phase is saturated with vapor certainly makes the evaporation process lean toward the diffusion-limited regime.

The experimental results presented in this section provide an excellent motivation to consider the combination of thermal and ‘solutal’ Marangoni effects, such that surface tension depends both on temperature and concentration gradients. This approach may provide explanation for the transition in the shape and size of the instability as the concentration of IPA in the mixture is varied.

5.4 Theory and Computations

In this section, we use our evaporation models developed in Chapter 2, and employ the numerical codes from Chapter 3 and volatility coefficients from Chapter 4 in order to perform numerical simulations of Eqs. (2.35), (2.36) and (2.37) for pure liquid films and drops. We wish to recover the main features of the “octopus”-shaped instability seen in experiments and described in Sections 5.1 and 5.3. First, we start with linear stability analysis (LSA) of Eq. (2.35) for thin film configuration to determine which liquid-solid set-up is most vulnerable to perturbations. We proceed by confirming the LSA predictions with numerical results for both 2d and 3d films. Next, we consider simulations for 2d planar and radial volatile drops and obtain instabilities, which are compared with the experimental data. Finally, we perform quasi-3d simulation of volatile drops, and explore the stability of a particular liquid-solid configuration to azimuthal perturbations.

5.4.1 Linear Stability Analysis

The analysis of the governing equation is to continue in two different directions. In the first direction, the linear stability analysis (LSA) of a flat infinite film is considered, exploring whether instability can be expected for the relevant physical parameters in this simplified geometry. In second, the focus switches to fully nonlinear numerical simulations, which are discussed in the following section. Even though the governing equation (2.35) is strongly nonlinear, the hope is that the use of linear theory will clarify the influence of different physical mechanisms on the stability of the interface. We note that only NEOS evaporation model is appropriate here. The values of parameters are in accordance with the discussion in Chapter 4.

The scaling is employed before proceeding any further, in order to simplify Eq. (2.35) by removing parameters A and S : $X = (A/S)^{1/2}x$ and $T = (A^2/S)t$ ([7]). The rescaled Eq. (2.35) becomes

$$\begin{aligned}
& \frac{\partial h}{\partial T} + \frac{\mathcal{E}}{h + \mathcal{K} + \mathcal{W}} + (h^3 h_{XXX})_X \\
& + \left[\left(\frac{\mathcal{D}h^3}{(h + \mathcal{K} + \mathcal{W})^3} + \frac{\mathcal{K}\mathcal{M}h^2}{(h + \mathcal{K} + \mathcal{W})^2} \right) h_X \right]_X \\
& + [h^3 ((b/h)^3 - (b/h)^2)]_X + \mathcal{G}(h^3 h_X)_X = 0,
\end{aligned} \tag{5.1}$$

where $\mathcal{E} = ES/A^2$, $\mathcal{D} = E^2/(DA)$, $\mathcal{M} = M/(PA)$, and $\mathcal{G} = G/A$. The LSA is performed by perturbing a flat film by a harmonic perturbation of a given wavelength λ , i.e., the disturbance h' will be assumed to have normal modes of the form $h' = H(T)e^{ikX}$, where k is disturbance wavenumber (not to be confused with thermal conductivity), and $H(T)$ is assumed to be of form $H(T) = \delta e^{\omega T}$, where δ is a small number, and ω is referred to as the growth rate of the disturbance; λ is given by $(2\pi)/k$. It is of interest to obtain the expression for $\omega(k)$. Positive (negative) growth rate will result in instability (stability). The value of k for which $\omega(k) = 0$ will be referred to as a critical wavenumber k_c . Corresponding critical wavelength will be denoted as λ_c .

Due to the presence of the evaporation, the base state is a thinning liquid layer. Therefore, it is necessary to consider small perturbations of a base state, which depends on T , but is X -independent ([7])

$$\bar{h} = -(\mathcal{K} + \mathcal{W}) + [(\mathcal{K} + 1)^2 - 2\mathcal{E}T]^{\frac{1}{2}}. \tag{5.2}$$

Next, $h = \bar{h} + h'$ is substituted into Eq. (5.1) and linearized, neglecting all but linear terms in h' . The resulting expression for $\omega(k)$ is

$$\begin{aligned}
\omega(k) = & \frac{\mathcal{E}}{R} \\
& + k^2 \left[k^2 \left[3R(\mathcal{K} + \mathcal{W}) + (\mathcal{K} + \mathcal{W})^3 - R^{\frac{3}{2}} - 3R^{\frac{1}{2}}(\mathcal{K} + \mathcal{W})^2 \right] \right. \\
& + \mathcal{D} + \mathcal{K}\mathcal{M} - \mathcal{G}(\mathcal{K} + \mathcal{W})^3 - 3R\mathcal{G}(\mathcal{K} + \mathcal{W}) + 3R^{\frac{1}{2}}\mathcal{G}(\mathcal{K} + \mathcal{W})^2 \\
& + R^{\frac{3}{2}}\mathcal{G} - \frac{(\mathcal{K} + \mathcal{W})}{R^{\frac{1}{2}}} (3\mathcal{D} + 2\mathcal{K}\mathcal{M}) + \frac{(\mathcal{K} + \mathcal{W})^2}{R} (3\mathcal{D} + \mathcal{K}\mathcal{M}) \\
& - \frac{\mathcal{D}(\mathcal{K} + \mathcal{W})^3}{R^{\frac{3}{2}}} + \frac{b^2}{(R^{\frac{1}{2}} - (\mathcal{K} + \mathcal{W}))^3} \left(2R^{\frac{3}{2}} - 6R(\mathcal{K} + \mathcal{W}) \right. \\
& + 6R^{\frac{1}{2}}(\mathcal{K} + \mathcal{W})^2 - 2(\mathcal{K} + \mathcal{W})^3 - \frac{3bR^{\frac{3}{2}}}{R^{\frac{1}{2}} - (\mathcal{K} + \mathcal{W})} + \frac{9bR(\mathcal{K} + \mathcal{W})}{R^{\frac{1}{2}} - (\mathcal{K} + \mathcal{W})} \\
& \left. \left. - \frac{9bR^{\frac{1}{2}}(\mathcal{K} + \mathcal{W})^2}{R^{\frac{1}{2}} - (\mathcal{K} + \mathcal{W})} + \frac{3b(\mathcal{K} + \mathcal{W})^3}{R^{\frac{1}{2}} - (\mathcal{K} + \mathcal{W})} \right) \right], \tag{5.3}
\end{aligned}$$

where $R = (\mathcal{K} + 1)^2 - 2\mathcal{E}T$. We note that according to Eq. (5.3), $\omega(0) > 0$, indicating instability at zero wavenumber. This is an artifact arising due to consideration of an unsteady base state (Eq. (5.2)). In particular, the mass loss effect enters the right-hand side of Eq. (5.3) algebraically through term \mathcal{E}/R . The comparison of the perturbation growth rate with the rate of change of the unsteady base state (e.g., see [7]) allows us to neglect this spurious term in further discussion.

In order to verify the complicated growth rate expression (Eq. (5.3)), it is cast into different forms corresponding to special regimes, which will be described in what follows. This will allow for comparison of the results which have been obtained so far with those from the previous works (e.g. [7]). Note that Eq. (5.3) is a growth rate expression which incorporates the influences of all relevant physical effects.

First, we consider the isothermal regime. The corresponding expression for growth rate ω is obtained from Eq. (5.3) by letting $\mathcal{K} = 0$ and neglecting evaporation ($\mathcal{E} = 0$). Furthermore, gravity effects and substrate heat conduction effects are ignored as well. The expression for growth rate is thus greatly simplified: the thin

liquid layer is now subject to capillary and disjoining pressure effects only. Hence, the base state is simply $\bar{h} = 1$. The resulting expression for growth rate ω is

$$\omega(k) = -k^4 + b^2(2 - 3b)k^2. \quad (5.4)$$

Maintaining the non-dimensionality, $k_c^2 = 1.97 \cdot 10^{-4}$ is obtained, corresponding to $k_c^2 = 1.97$ if scaling used in [7] is employed here. This is close to $k_c^2 = 1$, obtained in [7]. The results differ slightly due to different disjoining pressure model.

The quasi-equilibrium evaporation regime is obtained by setting $\mathcal{K} = 0$ in Eq. (5.3), while maintaining evaporation effect. As before, gravity effects and substrate heat conduction effects are neglected. In this case the time-dependent base state of the form $\bar{h} = (1 - 2\mathcal{E}T)^{\frac{1}{2}}$ is obtained. The growth rate is now given by

$$\omega(k) = -k^4(1 - 2\mathcal{E}T)^{\frac{3}{2}} + k^2 \left[\mathcal{D} + 2b^2 - \frac{3b^3}{(1 - 2\mathcal{E}T)^{\frac{1}{2}}} \right]. \quad (5.5)$$

Note once more that the growth rate is time-dependent. Therefore, further investigation of this expression is performed in two limits: ‘early times’ ($\mathcal{E}T \rightarrow 0$), and ‘late times’ ($\mathcal{E}T \rightarrow \mathcal{E}T_d$), where T_d is dryout time (such that $\bar{h}(T_d) = 0$), given by $T_d = 1/(2\mathcal{E})$.

Applying early time limit to Eq. (5.5), yields the following expression for the growth rate

$$\omega(k) = -k^4 + k^2(\mathcal{D} + 2b^2 - 3b^3). \quad (5.6)$$

From here, the critical wavenumber is calculated as $k_c^2 \approx 1.97 \cdot 10^{-4}$. This corresponds to $k_c^2 \approx 1.97$, when scaling as in [7] is used. This result agrees well with $k_c^2 = 1 + \mathcal{D} \approx 1$ from [7]. Once more, we note that the slight difference is due to different disjoining

pressure model. The value of k_c obtained here is approximately equal to the one for the isothermal case. This is due to the fact that \mathcal{D} is small, which reduces Eq. (5.6) to Eq. (5.4).

Applying the formal limit $\mathcal{E}T \rightarrow \mathcal{E}T_d$ to Eq. (5.5) is more involved: some terms in Eq. (5.5) become large in this limit. Therefore, we resort to integrating Eq. (5.5) with respect to T . This procedure yields the expression for the average growth rate

$$\omega_{avg}(k) = k^2 \left(-\frac{2}{5}k^2 + \mathcal{D} + 2b^2 - 6b^3 \right). \quad (5.7)$$

This results (after absorbing the factor b^2 into the definition of \mathcal{A}) in $k_c^2 = 4.85$, which is again very close to the result in [7]: $k_c^2 = 5(1 + \frac{1}{2}D) \approx 5$.

Therefore, we conclude that the growth rate ω given by Eq. (5.3) agrees well with the previous results in the considered regimes.

Clearly, the fact that the growth rate given by Eq. (5.3) is time dependent makes the analysis difficult. In order to simplify, we use the quasi-steady linear stability theory, also known as ‘frozen base state’ approach, where it is supposed that even though the base state is time-dependent, it varies slowly compared with the growth rate of the perturbations. Therefore, we are allowed to ‘freeze’ the base state at a particular time instant and analyze its stability as it were a steady state (e.g., see [7]). Since the early stages of the evolution of the instability are of particular interest, the limit $\mathcal{E}T \rightarrow 0$ is considered. Formal application of this limit to Eq. (5.3) yields

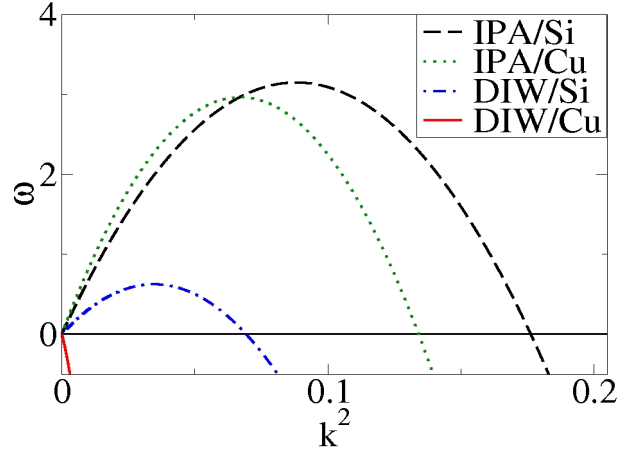


Figure 5.11 Growth rates versus k^2 for four considered configurations.

$$\begin{aligned}
\omega(k) = k^2 & \left[k^2 \left[3(\mathcal{K} + 1)^2(\mathcal{K} + \mathcal{W}) + (\mathcal{K} + \mathcal{W})^3 - (\mathcal{K} + 1)^3 \right. \right. \\
& - 3(\mathcal{K} + 1)(\mathcal{K} + \mathcal{W})^2 \left. \right] + \mathcal{D} + \mathcal{K}\mathcal{M} - \mathcal{G}(\mathcal{K} + \mathcal{W})^3 + (\mathcal{K} + 1)^3 \mathcal{G} \\
& - 3(\mathcal{K} + 1)^2 \mathcal{G}(\mathcal{K} + \mathcal{W}) + 3(\mathcal{K} + 1) \mathcal{G}(\mathcal{K} + \mathcal{W})^2 - \frac{(\mathcal{K} + \mathcal{W})}{(\mathcal{K} + 1)} (3\mathcal{D} + 2\mathcal{K}\mathcal{M}) \\
& + \frac{(\mathcal{K} + \mathcal{W})^2}{(\mathcal{K} + 1)^2} (3\mathcal{D} + \mathcal{K}\mathcal{M}) - \frac{\mathcal{D}(\mathcal{K} + \mathcal{W})^3}{(\mathcal{K} + 1)^3} + \frac{b^2}{(1 - \mathcal{W})^3} (2(\mathcal{K} + 1)^3 \\
& - 6(\mathcal{K} + 1)^2(\mathcal{K} + \mathcal{W}) + 6(\mathcal{K} + 1)(\mathcal{K} + \mathcal{W})^2 - 2(\mathcal{K} + \mathcal{W})^3 - \frac{3b(\mathcal{K} + 1)^3}{1 - \mathcal{W}} \\
& \left. \left. + \frac{9b(\mathcal{K} + 1)^2(\mathcal{K} + \mathcal{W})}{1 - \mathcal{W}} - \frac{9b(\mathcal{K} + 1)(\mathcal{K} + \mathcal{W})^2}{1 - \mathcal{W}} + \frac{3b(\mathcal{K} + \mathcal{W})^3}{1 - \mathcal{W}} \right) \right]. \quad (5.8)
\end{aligned}$$

Using Eq. (5.8) with parameter values corresponding to four liquid-solid configurations (IPA/Si, IPA/Cu, DIW/Si, and DIW/Cu), we plot the growth rate ω vs. k^2 in Figure 5.11. Note, that even though the LSA was performed in scaled coordinates X and T , these results represent growth rate ω vs. k^2 in original unscaled coordinates x and t from Eq. (2.35). The critical wavenumber k_c for each configuration is found, such that the flow is unstable for $k < k_c$. For Si substrate, $\lambda_c \approx 7.4 \text{ mm}$ for IPA is obtained, and a larger value $\lambda_c \approx 1.19 \text{ cm}$ for DIW. On a Cu substrate, $\lambda_c \approx 8.8 \text{ mm}$ for IPA; DIW on Cu is stable. Although the values of λ_c 's are larger than the patterns

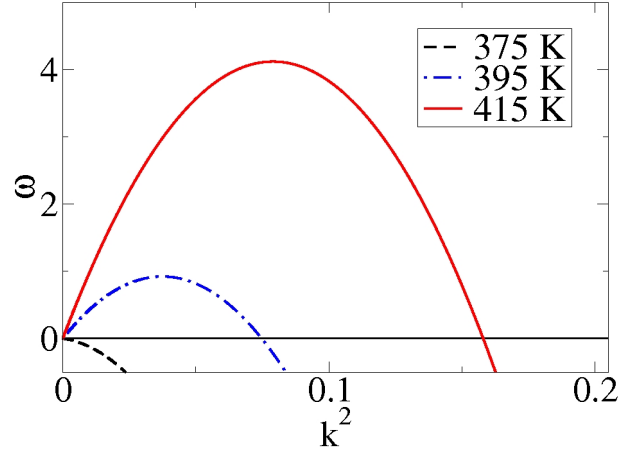


Figure 5.12 Growth rates versus k^2 for IPA/Si configuration with heated solid for several different values of T_{heater} . The configuration is stable when $T_{heater} = 375K$. As T_{heater} is increased, the transition to unstable regime is achieved.

occurring in the experiments, the results are encouraging since they show that the resulting λ_c 's are much smaller for IPA compared to DWI, and the corresponding growth rates are larger. Also, LSA results suggest that the instability is more likely to take place for IPA on Si than on Cu, again in agreement with the experiments.

Finally, we note that Eq. (2.35) can easily be modified to model a case when solid substrate is maintained at a prescribed temperature, instead of being thermally conductive. This is achieved by letting $\mathcal{W} = 0$, and using the solid temperature T_{heater} and the boiling temperature T_{boil} instead of T_0 and T_{sat} respectively in the definition of the temperature scale (see Chapter 2). We perform LSA for IPA/Si configuration, for which we use $T_{boil} = 355K$. We examine the variation of the the growth rate ω and critical wavenumber k as T_{heater} is varied. The results for $T_{heater} = 375K$, $395K$ and $415K$ are shown in Figure 5.12. The configuration is stable when $T_{heater} = 375K$, but it becomes unstable as T_{heater} is increased. Further increase in T_{heater} results in increase of both k_c and ω_{max} .

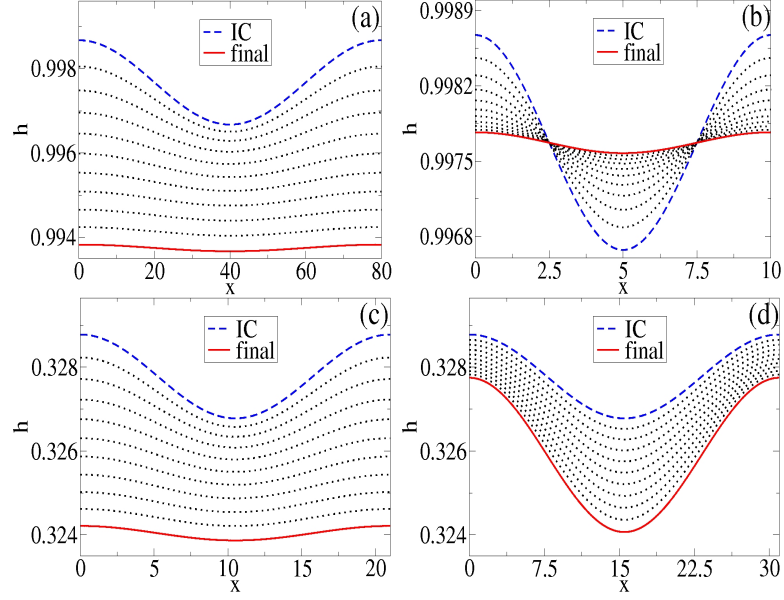


Figure 5.13 Time evolution of perturbed thin films for DIW/Cu and DIW/Si configurations. Dashed lines indicate the initial conditions, the full lines indicate the final profile, while dotted lines indicate the film profiles for times between $t = 0$ and the final time t_{final} . (a) DIW/Cu, $k = 0.08$: stable ($t_{final} = 2$); (b) DIW/Cu, $k = 0.63$: stable ($t_{final} = 10^{-3}$); (c) DIW/Si, $k = 0.3 > k_c$: stable ($t_{final} = 2$); (d) DIW/Si, $k = 0.2 < k_c$: unstable ($t_{final} = 1$).

5.4.2 Verification of the Linear Stability Analysis Predictions

Next, we perform series of simulations of Eqs. (2.35) and (2.37) using our numerical code developed in Chapter 3, in order to verify LSA predictions. We numerically study the stability of thin films of pure liquid subject to perturbations of given wavenumber k . As in Section 5.4.1 we only use NEOS evaporation model.

First, we consider 2d films and perform numerical simulations of Eq. (2.35). The initial condition considered here is a thin film of thickness $\bar{h} = 1 - \mathcal{W}$, with a small perturbation of prescribed wavenumber k applied. The parameter values used correspond to four liquid-solid configurations (DIW/Cu, DIW/Si, IPA/Cu and IPA/Si). The values of the wavenumbers k are chosen such that for each configuration the numerical simulations are performed with both $k < k_c$ and $k > k_c$, where k_c is the critical wavenumber (if it exists) for the particular configuration, predicted by the LSA in Section 5.4.1. In particular, LSA gives: $k_c \approx 0.26$ for DIW/Si, $k_c \approx 0.37$ for

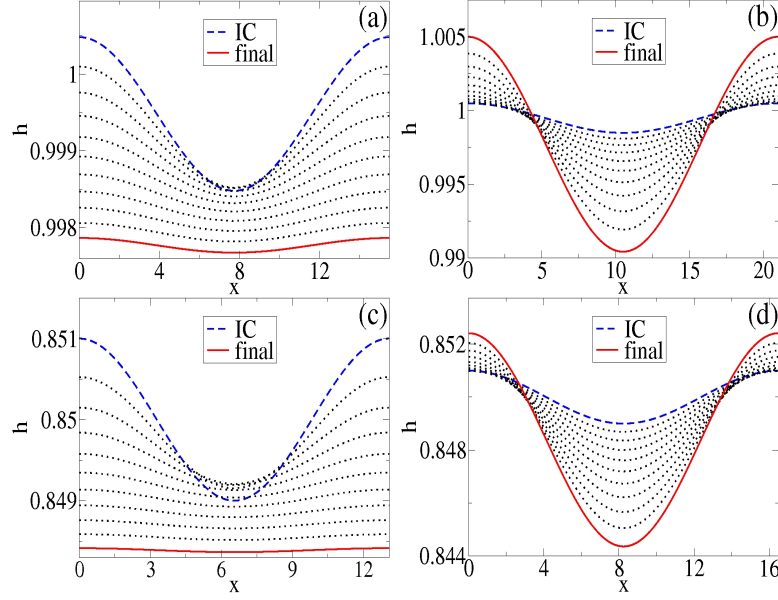


Figure 5.14 Time evolution of perturbed thin films for IPA/Cu and IPA/Si configurations. Dashed lines indicate the initial conditions, the full lines indicate the final profile, while dotted lines indicate the film profiles for times between $t = 0$ and the final time t_{final} . (a) IPA/Cu, $k = 0.4 > k_c$: stable ($t_{final} = 0.73$); (b) IPA/Cu, $k = 0.3 < k_c$: unstable ($t_{final} = 0.75$); (c) IPA/Si, $k = 0.48 > k_c$: stable ($t_{final} = 0.75$); (d) IPA/Si, $k = 0.38 < k_c$: unstable ($t_{final} = 0.75$).

IPA/Cu, $k_c \approx 0.42$ for IPA/Si, while DIW/Cu is stable to perturbations of all wave numbers. Figures 5.13 and 5.14 show the results of numerical simulations, which are in full agreement with the LSA predictions for all considered liquid-solid configurations.

Figure 5.15 shows the comparison of the numerical results and the LSA prediction for maximum growth rate for the IPA/Si configuration ($k_{max} = 0.297$ and $\omega_{max} = 3.148$). The dashed-and-dotted line is the LSA prediction (slope ω_{max}); the solid line is the numerical result: $\ln[(h_{max}(t) - \bar{h})/\delta]$ vs. time t . Figure 5.15 implies excellent agreement between the numerical results and the LSA prediction. Similar agreement has been confirmed for the other two, potentially unstable configurations (IPA/Cu and DIW/Si).

Before we proceed further, we examine the long-time evolution of the same IPA/Si thin film configuration disturbed by the perturbation with $k = k_{max}$. The goal here is to capture the moment when the film ruptures, as well as the subsequent

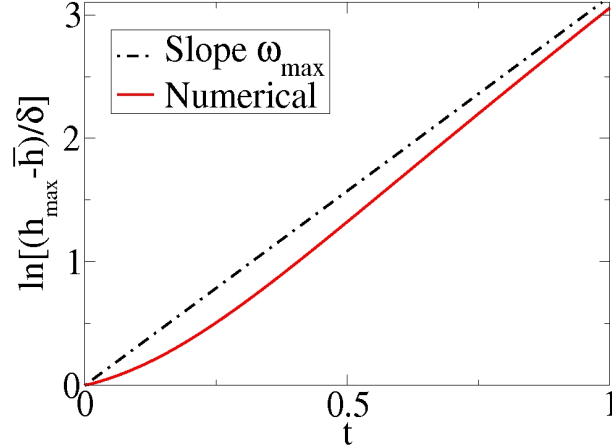


Figure 5.15 Maximum growth rate of perturbation: the comparison of numerical results and LSA prediction for IPA/Si configuration; $k_{max} = 0.297$, $\omega_{max} = 3.148$, $\bar{h} = 1 - \mathcal{W} = 0.85$, and $\delta = 10^{-3}$.

dewetting dynamics. Figure 5.16 shows the results of these simulations. Note that the initial disturbance is not clearly visible on the scale shown. The disturbance grows rapidly, eventually leading to film ‘rupture’, which is clearly seen. The film collapses into several smaller drops in the center of the domain, while the bulk of the film recedes (left and right). We note that this is not a true rupture: due to the presence of disjoining pressure, stable film remains and it connects the individual drops and the bulk of the film. The results shown in Figure 5.16 are reminiscent of the results obtained by other researchers for similar set-ups (see, e.g. [56]).

Next, we perform numerical simulations to confirm the LSA predictions for the case when the solid is maintained at a fixed temperature. We focus on the IPA/Si configuration with $T_{heater} = 415K$. Thin film of thickness $\bar{h} = 1$ is perturbed by a small perturbations with either $k < k_c$, or $k > k_c$, where $k_c \approx 0.4$ has been obtained by LSA in Section 5.4.1. The results of these simulations are shown in Figure 5.17. We conclude that the numerical results are in excellent agreement with the LSA predictions for the heated solid configuration.

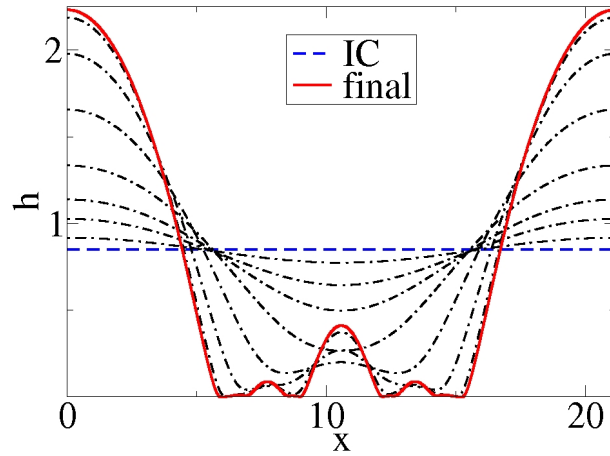


Figure 5.16 The longer-time evolution, thin film ‘rupture’ and subsequent dewetting: IPA/Si thin film configuration disturbed by a small perturbation ($\delta = 10^{-3}$) with $k = k_{max}$; $t_{final} = 30$

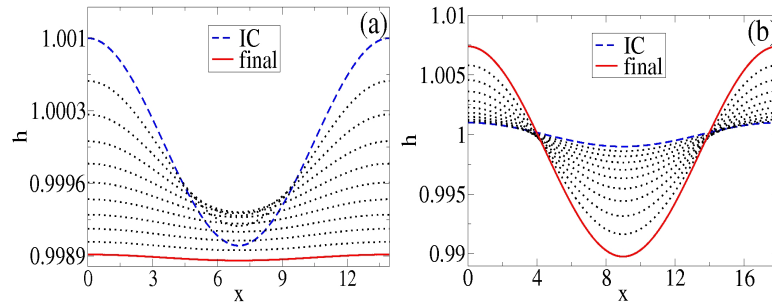


Figure 5.17 Time evolution of perturbed thin films for IPA/Cu and IPA/Si configurations for heated solid case, where $T_{heater} = 415K$. Dashed lines indicate the initial conditions, the full lines indicate the final profile, while dotted lines indicate the film profiles for times between $t = 0$ and the final time t_{final} . (a) IPA/Si, $k = 0.45 > k_c$: stable ($t_{final} = 0.6$); (b) IPA/Si, $k = 0.35 < k_c$: unstable ($t_{final} = 0.75$).

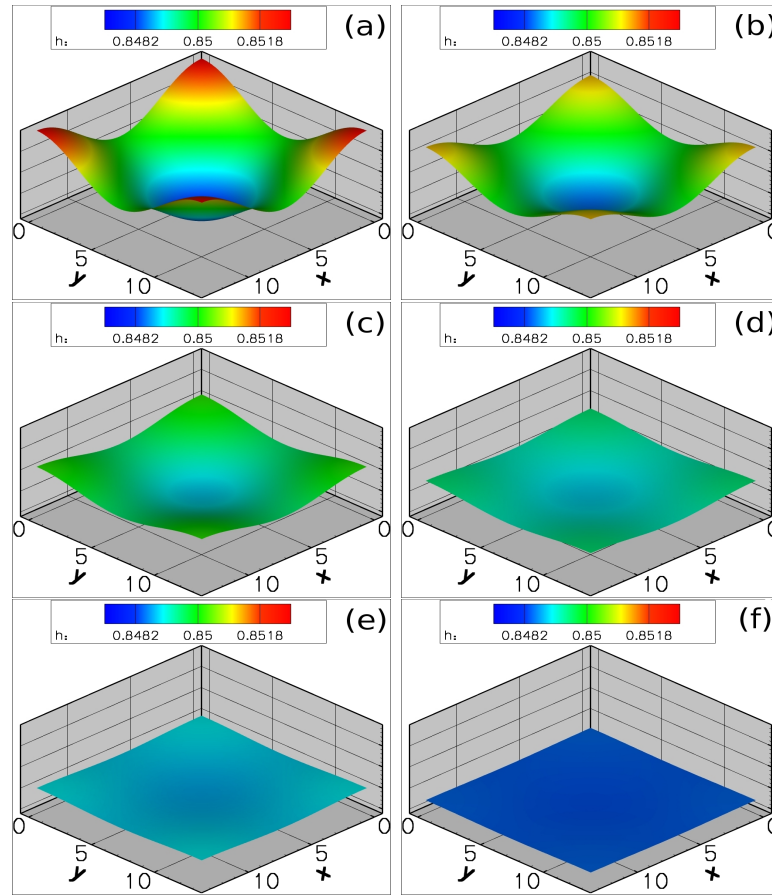


Figure 5.18 Time evolution of IPA/Si thin film disturbed by perturbation with $k = 0.48 > k_c$. Time evolves left to right, and top to bottom: (a) $t = 0$; (b) $t = 0.15$; (c) $t = 0.3$; (d) $t = 0.45$; (e) $t = 0.6$; (f) $t = 0.75$. The configuration is stable.

Finally, we perform 3d numerical simulations for film, using similar approach as the one used for 2d films: a flat film is perturbed (in both x - and y - direction) using perturbations with wavelengths suggested by LSA and its subsequent stability is examined. We focus only on the IPA/Si configuration with thermally conductive solid. The numerical results for $k = 0.48 > k_c$ and $k = 0.38 < k_c$ are shown in Figures 5.18 and 5.19 respectively, and are in excellent agreement with the LSA predictions.

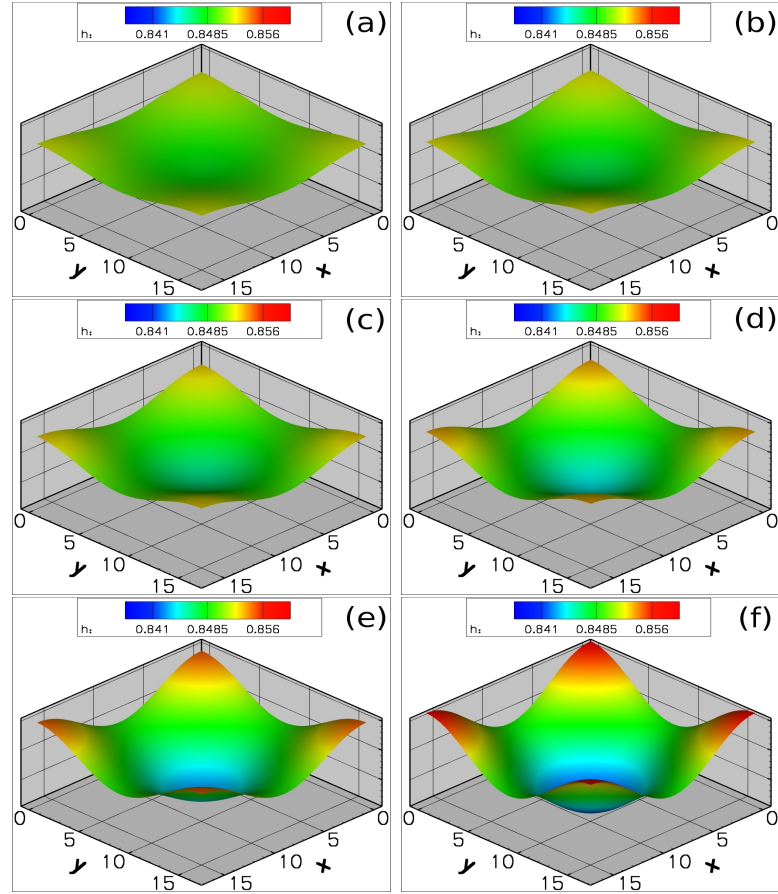


Figure 5.19 Time evolution of IPA/Si thin film disturbed by perturbation with $k = 0.38 < k_c$. Time evolves left to right, and top to bottom: (a) $t = 0$; (b) $t = 0.15$; (c) $t = 0.3$; (d) $t = 0.45$; (e) $t = 0.6$; (f) $t = 0.75$. The configuration is unstable.

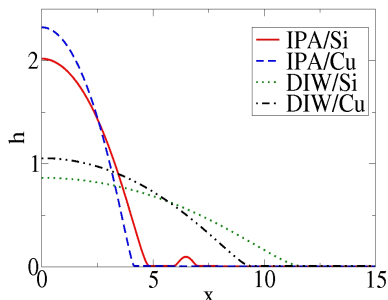


Figure 5.20 Planar drop profiles at $t = 1$ for 4 considered configurations (IC is not shown). Notice the instability which occurs ahead of the contact line for IPA/Si configuration.

5.4.3 Numerical Simulations for Volatile 2d Planar and Radial Drops

Next, we perform numerical simulations of drops, considering only the thermally conductive solid case. We first solve Eq. (2.35) for a spherical cap initial condition. In this case, we are focusing on a cross section of a planar drop. The simulations are performed using NEOS evaporation model and material parameters corresponding to 4 liquid-solid configurations (IPA/Si, IPA/Cu, DIW/Si and DIW/Cu). Figure 5.20 shows numerical results for all considered cases at dimensionless time $t = 1$ (corresponding to $t = 0.3s$). The most interesting result in Figure 5.20 is the instability which appears for IPA/Si configuration just ahead of the contact line. The shape of the instability resembles the “octopi” which we see in the experiments. It is especially important to note that instability occurs only for IPA/Si configuration. A configuration with the solid characterized by larger heat conductivity (Cu), or less volatile but more (heat) conductive liquid (DIW) is stable. Therefore, we conclude that thermal properties of the particular liquid-solid configuration, and the resulting temperature gradients which induce Marangoni forces, are responsible for occurrence of “octopus”-shaped instabilities.

Keeping this conclusion in mind, we proceed by considering evaporation of 2d radial drops. We perform numerical simulations of Eq. (2.36) for IPA/Si configuration. The initial condition for all simulations is obtained in a manner similar to the one

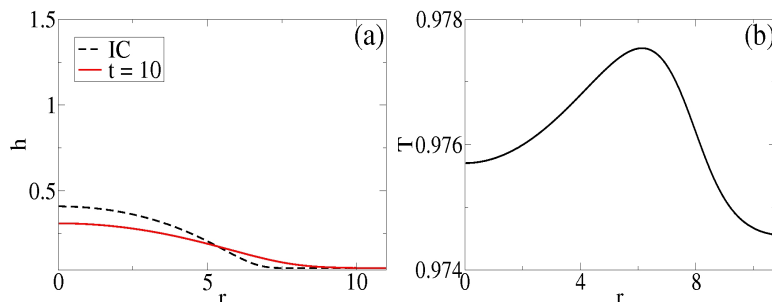


Figure 5.21 IPA/Si: numerical results for a 2d radial drop using “lens” evaporation model. (a) Evolution of drop thickness from $t = 0$ (dashed line) to $t = 5$ (solid line): note stretching of the contact line region; (b) Temperature profile at the liquid-gas interface at $t = 5$: notice the temperature maximum.

used to produce the initial profile for IPA/Si simulations discussed in Chapter 4: it is a smooth spherical cap with volume $3.2\mu\text{l}$. Both “lens” and NEOS models are considered. The physical parameters correspond to IPA/Si configuration, with the exception of volatility parameters α and χ : larger values $\alpha = 8 \cdot 10^{-5}$ and $\chi = 3 \cdot 10^{-1}$ are used here, in order to make the main features of the dynamics more obvious. In particular, the increase in volatility results in larger temperature gradients when compared to the ones shown in Chapter 4 for IPA/Si configuration. As a result, Marangoni forces, which act in opposing directions for “lens” and NEOS models, are going to be stronger. Therefore, we expect more pronounced stretching of the contact line region for “lens” model, and more pronounced receding motion for NEOS model.

Figure 5.21 shows numerical result for evolution of drop thickness (a) and the temperature at liquid-gas interface (b) for IPA/Si configuration using “lens” evaporation model. The stretching of the contact line is clearly visible in Figure 5.21(a). At the same time, the drop remains relatively thick at the center. This behavior has been expected, and the reason for it lies in Marangoni forces. Figure 5.21(b) provides immediate support for such a claim. It indicates that there is a temperature maximum some distance away from the contact line. The Marangoni forces associated with the outer temperature gradient induce outward flow along the interface, which tends to stretch the contact line region and enhances spreading. On the other hand,

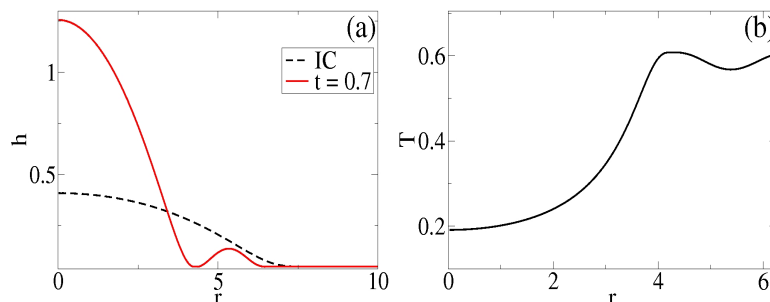


Figure 5.22 IPA/Si: numerical results for a 2d radial drop using NEOS evaporation model. (a) Evolution of drop thickness from $t = 0$ (dashed line) to $t = 0.7$ (solid line): notice the instability which occurs ahead of the contact line and resembles the “octopus”-shaped instability; (b) Temperature profile at the liquid-gas interface at $t = 0.7$.

the Marangoni forces associated with the inner temperature gradient result in inward flow, responsible for maintaining relatively large thickness of the drop at the center. The outward flow is clearly more pronounced at the stage shown in Figure 5.21.

Figure 5.22 shows numerical result for evolution of drop thickness (a) and the temperature at liquid-gas interface (b) for IPA/Si configuration using NEOS evaporation model. The most interesting detail in Figure 5.22(a) is the instability which occurs during the receding motion of the drop. The appearance of this instability is reminiscent of the “octopi” which we see in experiments. We note that “octopi” occur during the spreading stage of the evolution, in contrast to the results in Figure 5.22(a). Strong Marangoni forces (Figure 5.22(b)), which induce inward flow along the interface from the contact line toward the center of the drop, are responsible for such a behavior. This flow enhances rapid receding motion of the drop, which destabilizes the contact line region and results in the instability seen in Figure 5.22(a).

We note that the temperature gradient in Figure 5.22(b) is significantly larger than the one in Figure 5.21(b) for “lens” model, making the (inward) Marangoni force for NEOS much larger than the (outward) one for “lens” model. Hence, the simulations for “lens” model have been carried out until $t = 5$ in order to obtain

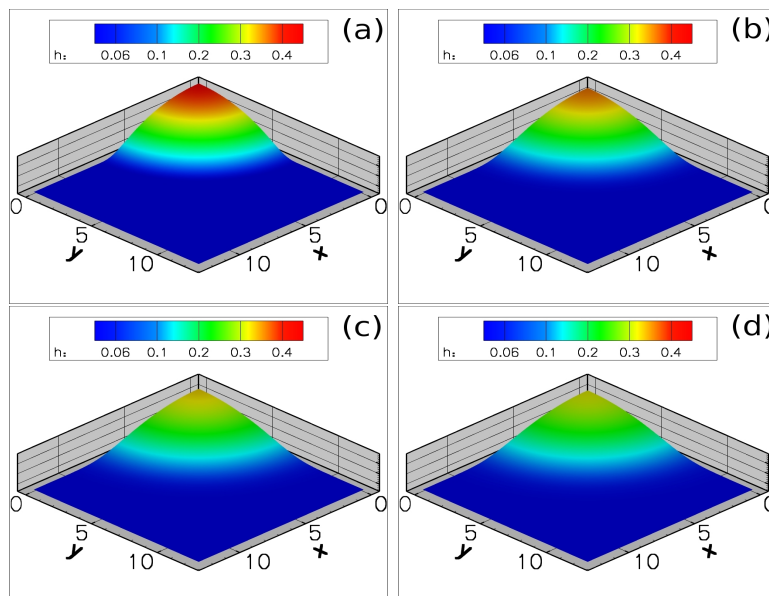


Figure 5.23 IPA/Si: evolution of a 3d drop using “lens” evaporation model. (a) $t = 0$: the initial condition; (b) $t = 1.5$: the onset of the spreading motion; (c) $t = 3.5$: the stretching of the contact line region is evident; (d) $t = 5$: the final state.

clearly visible traits of the dynamics, while for NEOS model much shorter simulations ($t = 0.7$) have been sufficient.

5.4.4 Numerical Simulations for Volatile 3d Drops

We conclude this Chapter with the results of quasi-3d simulations for drops. We solve Eqs. (2.37) using the code developed in Chapter 3 for IPA/Si configuration, using both evaporation models. We consider only the case where solid is thermally conductive. The parameter values are identical to those used in Section 5.4.3 for 2d radial drops. We also use the same procedure for creating the initial condition for our simulations as the one used for 2d radial drops.

Figure 5.23 shows the numerical result for “lens” model. These results are 3d equivalent of the 2d results which have been shown in Figure 5.21(a): the Marangoni forces act outward in the narrow region close to the contact line, and inward for the rest of the liquid-gas interface, which leads to stretching of the contact line region into a thin layer. Figure 5.24 shows results for NEOS model, and these are equivalent

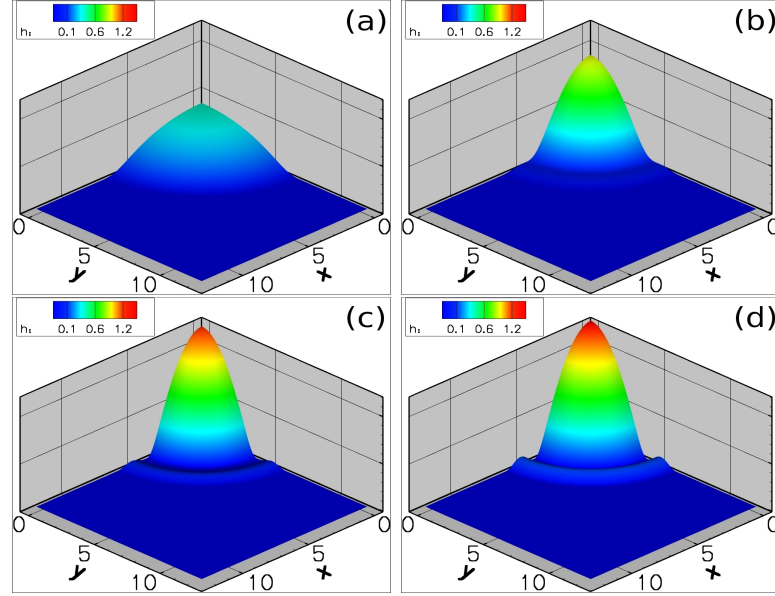


Figure 5.24 IPA/Si: evolution of a 3d drop using NEOS evaporation model. (a) $t = 0$: the initial condition; (b) $t = 0.1$: receding motion; (c) $t = 0.3$: the ‘ring’ appears; (d) $t = 0.7$: the final state – full blown ‘ring’ ahead of the contact line.

to the results which have been shown in Figure 5.22(a) for 2d radial drop with NEOS model: due to strong inward Marangoni forces, the contact line recedes swiftly and the interface becomes unstable, leaving a thin ring of fluid behind.

5.4.5 Azimuthal Perturbations of 3d Drops

Encouraged by the results in Figures 5.23 and 5.24, we examine the stability of IPA/Si drops using both evaporation models to azimuthal perturbations of the contact line region. The parameters and the basic initial profile are identical to those used in Section 5.4.4. The basic initial condition is perturbed using a harmonic perturbation of a given wavelength λ , i.e., the disturbance is of the form $\delta e^{ik\varphi}$, where k is the disturbance wavenumber ($\lambda = 2\pi/k$), δ is the magnitude of the perturbation (we use $5 \cdot 10^{-3}$), and φ is the azimuthal angle ($0 \leq \varphi \leq \pi/2$ in the first quadrant). The azimuthal perturbations considered here amount to displacing the contact line position of the basic initial profile by a small amount. We note that the number of full periods of the perturbation which are visible in the first quadrant is $k/4$.

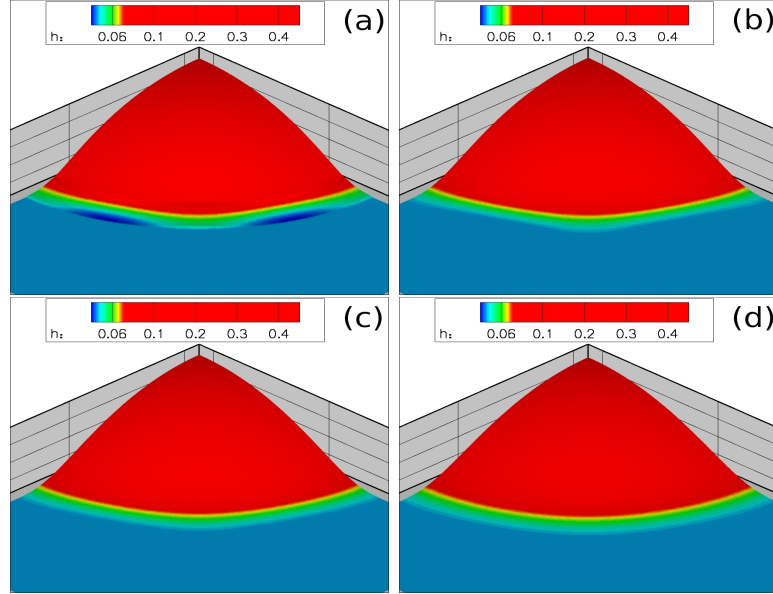


Figure 5.25 Evolution of azimuthal perturbation for IPA/Si configuration using “lens” model. (a) $t = 0$: the contact line region is perturbed using an azimuthal perturbation with $k = 8$ (2 full wavelengths are visible); (b) $t = 0.1$: the perturbation decays, and is not visible in (c) at $t = 0.3$; (d) $t = 0.5$: the spreading proceeds in a manner similar to that seen in Figure 5.23. The configuration is stable.

In Figure 5.25 we show the results for the “lens” model with azimuthal perturbation with $k = 8$. The drop spreads and the perturbation rapidly decays. Almost identical evolution occurs when perturbation with $k = 12$ is used (Figure 5.26). Furthermore, Figure 5.27 shows that the configuration is also stable when $k = 64$ is considered; the profile stabilizes even faster than for $k = 8$ and $k = 12$ cases. Finally, we have confirmed the stability for the case when $k = 4$ is used (the results are omitted), and are confident that the configuration is stable to perturbations with shorter wavelengths than the ones considered here ($k > 64$). The stability of the configuration which uses “lens” model to azimuthal perturbations of all wavelengths is explained as follows. As discussed in Sections 5.4.3 and 5.4.4, Marangoni forces are responsible for both the rapid spreading motion of the drop and the ‘stretching’ of the contact line region when “lens” model is considered. Therefore, if the perturbation with wavenumber k is applied, and if two cross-sections of the drop are considered,

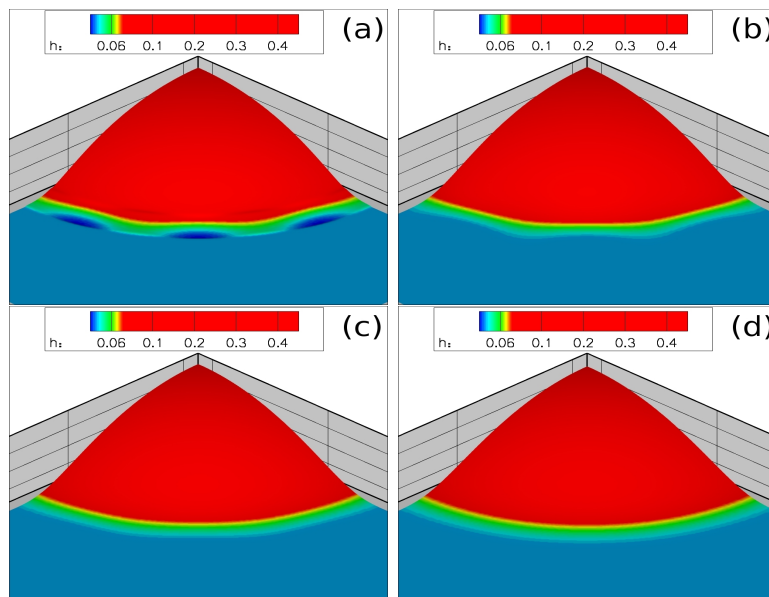


Figure 5.26 IPA/Si configuration using “lens” model: evolution of azimuthal perturbations. (a) $t = 0$: the contact line region is perturbed using an azimuthal perturbation with $k = 12$ (3 full wavelengths are visible), which decays ($t = 0.1$ in (b)), until it is no longer visible at $t = 0.2$ in (c); (d) $t = 0.5$: the spreading proceeds in a manner similar to that seen in Figure 5.23. The configuration is stable.

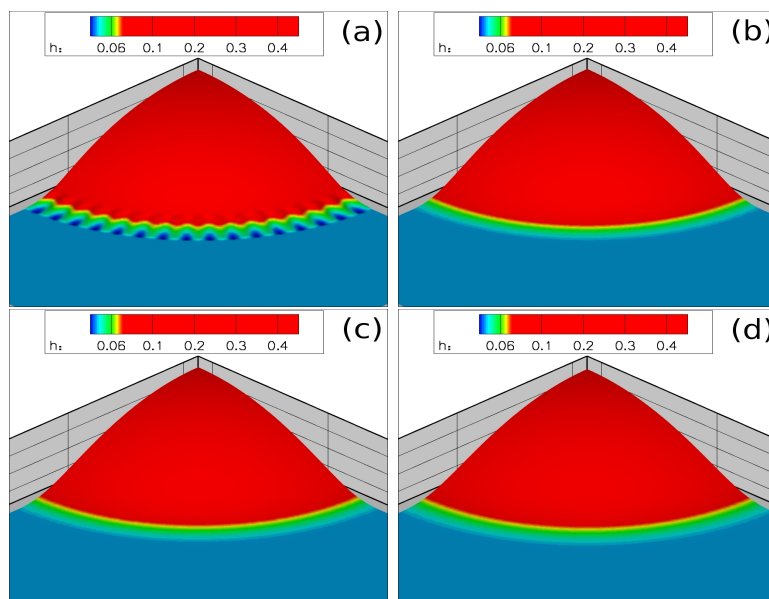


Figure 5.27 Evolution of azimuthal perturbation for IPA/Si configuration using “lens” model. (a) $t = 0$: the contact line region is perturbed using an azimuthal perturbation with $k = 64$ (16 full wavelengths are visible); (b) the decay is so rapid that the perturbation is no longer visible at $t = 0.05$. The spreading proceeds in a manner similar to that seen in Figure 5.23 ($t = 0.5$ in (d)). The configuration is stable.

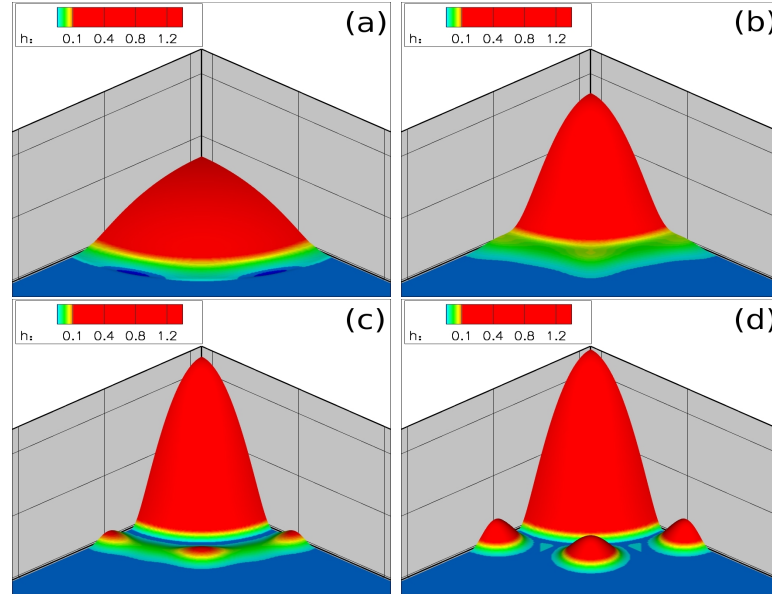


Figure 5.28 Evolution of azimuthal perturbation for IPA/Si configuration using NEOS model. The contact line region is perturbed at $t = 0$ (a), using an azimuthal perturbation with $k = 8$ (2 full wavelengths are visible in (a)). The drop recedes and the ‘ring’ seen in Figure 5.24 begins to take shape immediately ($t = 0.07$ in (b)); the ‘ring’ rapidly destabilizes and its dissolution into drops ensues ($t = 0.21$ in (c)); eventually, the ‘ring’ collapses into individual drops ($t = 0.7$ in (d)). The configuration is unstable; note the resemblance of the instability to the “octopi” seen in experiments.

e.g. one for $\varphi = \varphi_1$, and the other for $\varphi = \varphi_2$ (such that $\cos k\varphi_1 \neq \cos k\varphi_2$), one finds that they have the same thickness at the center, but different radii. As a result, the temperature drop between the center and the contact line for these two cross-sections is identical. However, the temperature gradient and the resulting Marangoni force are larger for the cross-section with smaller radius. This causes faster spreading for this cross-section when compared to the one with larger radius, and inevitably, the decay of the perturbation.

Next, we focus on the NEOS evaporation model. Figure 5.28 shows the results for $k = 8$. The drop recedes as in Figure 5.24, and the ring instability develops (b). However, the azimuthal perturbation leads to destabilization of the ring, so that its collapse into individual drops begins in (c). Finally, as the receding motion continues,

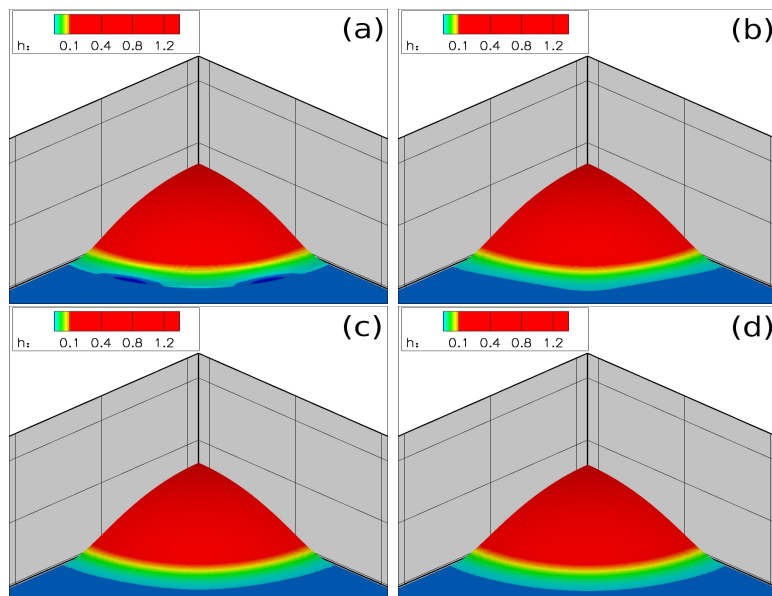


Figure 5.29 Evolution of the azimuthal perturbation for IPA/Si configuration using NEOS model with $M = 0$ (Marangoni forces are neglected). (a) $t = 0$: the contact line region is perturbed using an azimuthal perturbation with $k = 8$ as in Figure 5.28; (b) $t = 0.07$: the drop spreads and the perturbation decays rapidly; (c) $t = 0.21$ and (d) $t = 0.7$: the spreading continues – there is no ‘ring’ ahead of the contact line. The configuration is stable.

the ring evolves into isolated drops, which remain ahead of the contact line (d). This development bears similarity to the “octopi” which we see in the experiments. The mechanism, however, appears to be different, since the “octopi” in Figure 5.28 are associated with dewetting. As described in Sections 5.4.3 and 5.4.4, the instability in Figure 5.28 is due to receding motion caused by Marangoni forces which act inward (from the contact line toward the drop center) along the liquid-gas interface. To confirm this statement, we perform a simulation using the same parameters and perturbation as in Figure 5.28, but now with $M = 0$ (Marangoni forces are neglected). The results of this simulation are shown in Figure 5.29. We find, as expected, that with the Marangoni forces neglected, the drop spreads under gravity and surface tension, and the perturbation decays. In addition, with the absence of Marangoni forces, the ‘ring’ instability seen in Figure 5.24 is also eliminated.

It is of interest to compare the wavelength λ of the perturbation which we use in Figure 5.28, with the predictions of LSA for the film configuration, discussed in Section 5.4.1. We note that for IPA/Si configuration, the critical (dimensionless) wavelength predicted by LSA is $\lambda_c = 14.8$, where the length scale is the typical film thickness $d_0 = 0.5\text{mm}$ (corresponding to $h = 1$). The length scale relevant to the destabilization process in Figure 5.28 is clearly shorter – some thickness between the drop thickness at the center, $h = h_{max} = 0.5$, and $h = 0$ at the contact line seems more appropriate. We calculate the wavelength of the perturbation in Figure 5.28 using $h_{max}/2$ as the relevant length scale, and obtain $\lambda \approx 20.4$, which, according to the LSA results, is in the unstable range. Therefore, it appears that the result in Figure 5.28 is in agreement with the LSA prediction for the film configuration. To test this agreement further, we also consider perturbations with $k = 4$, $k = 12$ and $k = 64$, with corresponding wavelengths $\lambda \approx 40.8$, $\lambda \approx 15.6$ and $\lambda \approx 2.8$ respectively. First, the configuration with $k = 4$ has been found to be unstable (we omit the results). Further, we find that the configuration with $k = 12$ is also unstable, as shown in Figure 5.30. The evolution proceeds in a manner similar to the one when $k = 12$; however, now the number of drops to which the ‘ring’ collapses is increased accordingly. Finally, the configuration with $k = 64$ is found to be stable and the results are shown in Figure 5.31.

In summary, we have found that the configuration using “lens” model is stable to all considered azimuthal perturbations. We have explained this behavior using an argument based on Marangoni forces. In addition, for the NEOS model, we have found interesting instabilities, which occur when azimuthal perturbations of certain wavelengths are applied. The unstable wavelengths are in good agreement with the predictions of the linear stability analysis. The instabilities bear strong resemblance to the “octopi” seen in the experiments. However, the details of the instability development are different: in our simulations, these develop during the receding part of

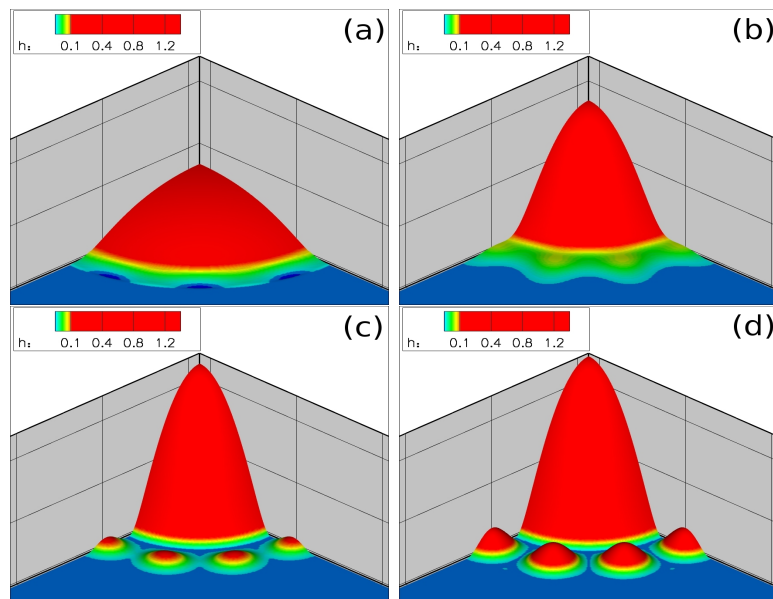


Figure 5.30 Evolution of azimuthal perturbation for IPA/Si configuration using NEOS model. (a) $t = 0$: the contact line region is perturbed with azimuthal perturbation with $k = 12$ (3 full wavelengths are visible); (b) $t = 0.07$: the drop recedes and the ‘ring’ forms; (c) $t = 0.21$: the ‘ring’ destabilizes; (d) $t = 0.7$: finally, the ‘ring’ collapses into individual drops. The configuration is unstable.

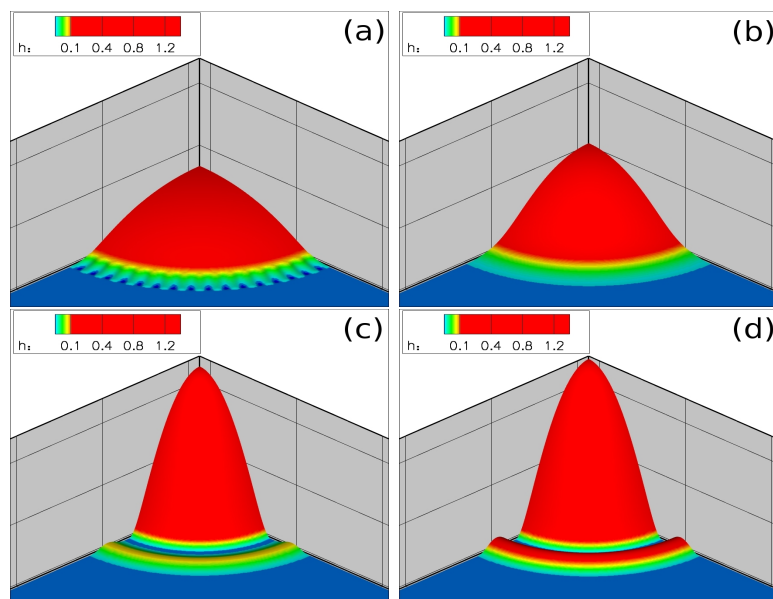


Figure 5.31 Evolution of azimuthal perturbation for IPA/Si configuration using NEOS model. (a) $t = 0$: the contact line region is perturbed with azimuthal perturbation with $k = 64$ (16 full wavelengths are visible); (b) $t = 0.07$: the drop recedes, the perturbation decays, and the ‘ring’ forms; (c) $t = 0.21$: the ‘ring’ becomes larger as the receding motion continues; (d) $t = 0.7$: the ‘ring’ remains intact. The configuration is stable.

the droplet motion, while in the experiments the instabilities are observed during the spreading stage.

There are few possible explanation for the differences between the simulations and experiments. For example, the initial condition that we use in the simulations presented here is clearly different from the experimental one: in the experiment, the initial drop profile is characterized by large gradients where lubrication approximation may not apply. In addition, we have considered only one family of azimuthal perturbations. Other types of perturbations could be justified on physical grounds, such as perturbations of the thickness of a drop, or of the wetting properties of the substrate. We hope that future work will resolve the questions which are still left open. The results presented here show clearly how important are the evaporation models in determining the stability of evaporating drops.

CHAPTER 6

CONCLUSIONS AND FUTURE WORK

The experiments, in which an interesting “octopus”-shaped instability was observed during the evaporation of sessile drops, have served as the motivation for this work. The instability was found to appear only for pure drops of volatile isopropyl alcohol (IPA) evaporating on silicon (Si) solid substrate. A liquid with larger thermal conductivity and decreased volatility, e.g. water (DIW), or a solid with larger thermal conductivity, e.g. copper (Cu), were found to suppress the “octopi”. We have set out to explain this instability, and soon discovered that the critical component necessary for achievement of this goal is the use of evaporation model most appropriate for the physical situation considered. The variety of evaporation models which have been used previously by other researchers, and in particular, the sometimes questionable physical arguments on which certain choice of a model was based, have led us to consider a couple of commonly used ones. We have derived the corresponding mathematical models for evaporation of drops and films, resulting in governing equations for liquid thickness. We have also developed a numerical code for solving these equations, and used it to compare our theoretical results directly to our experimental data, in order to identify the evaporation model appropriate for a particular physical situation. Using these evaporation models, we have performed quasi-3d simulations for both drops and films and examined their stability. In addition, we have carried out experiments with volatile mixtures and examined the influence of the state of the gas phase and the composition of the mixture, among other factors, on the shape and the size of instabilities which occur.

First, we have reviewed various models used for describing evaporation of liquid drops from solid substrates. We have also reviewed various assumptions one can

make in order to simplify the complicated two-sided model to various less complex ones. The critical difference between these models is the manner in which evaporation process is included. Finally, we focus on two relatively simple and commonly used models: the “lens” evaporation model and the non-equilibrium one-sided (NEOS) evaporation model. The physical arguments which lead to each model are discussed. We have stressed the fact that these two models are mutually exclusive. The parameters which determine which model is more appropriate are difficult to measure experimentally. Therefore, we have developed a mathematical model which includes both evaporation models and compared the results against our experimental data. The critical volatility parameters are estimated directly from the experimental results. The governing equation for drop thickness includes the mass flux J explicitly (Eq. (2.36)). Therefore, either evaporation model can be used, simply by substituting the appropriate expression for J . We have also developed a finite-difference based numerical code for solving the governing equation for both drops and films. The time discretization has been handled using the Crank-Nicholson scheme, and the 3d code has been developed using the ADI scheme. The governing equation is solved numerically and the results are compared to the experimental data. Two different liquids have been considered, DIW and IPA. For the case of DIW, it has been found that NEOS evaporation model performs better than the “lens” model. This is additionally supported by further experiments in which external convection has been applied to the gas phase, and which have shown that the evaporation process is mostly insensitive to the manner in which vapor is being removed from the evaporating interface. In the case of IPA, the volatility coefficients have been estimated from the experimentally measured dryout time. The comparison of our numerical results for the two models against the experimental data ([9, 25, 27, 61]) has revealed that in the case of IPA, “lens” model performs better than NEOS model. The factors which contribute to a change in evaporation regime from reaction-limited (NEOS) in the case of DIW, to

diffusion-limited (“lens”) in case of IPA, are increased volatility and vapor density for IPA when compared to DIW. Finally, we have examined the influence of Marangoni forces on evolution of contact line position and evaporation rate for the case of IPA. We conclude that for “lens” model, Marangoni forces induce spreading and increase the evaporation rate. We also note the prospects of using these two evaporation models for resolving an interesting problem of “octopus”-shaped instabilities, which appear ahead of the contact line of spreading IPA drops.

Having compared the performance of the two evaporation models against the experimental data, and having made conclusions regarding appropriateness of these models for a particular physical situation, we have performed experiments with volatile drops of IPA-DIW mixtures evaporating on Si wafers and glass slides. These experiments have been geared toward better understanding of the “octopi” instability, its robustness and sensitivity to state of the gas phase in the experimental set-up, as well as the concentration of IPA in the mixtures. We have found that the instability is very robust – we have been able to obtain the “octopus”-shaped instabilities for pure IPA drops in our lab. Furthermore, we have found that this instability is mostly insensitive to the state of the gas phase: the “octopi” have been seen readily even when the gas phase has been saturated by the vapor, or when externally applied convection of air has been introduced. Finally, we have found curiously shaped instabilities for all liquid mixtures evaporating on both considered solid substrates; we have examined the dependence of the shape and the size of the instabilities on the IPA concentration, and the transition from relatively large mushroom-shaped instabilities (70% IPA) to “octopi” (pure IPA).

Next, we have focused on the “octopi” instability and performed linear stability analysis (LSA) for the thin film configuration using the NEOS model in order to determine which one of several considered liquid-solid configurations is most likely to become unstable. We have found that IPA/Si is most unstable, in direct agreement

with the experiments. In addition, we have used our numerical code to confirm the LSA predictions for both 2d and 3d cases. After obtaining these results, we have performed a series of numerical simulations for volatile drops in various geometries: 2d planar and radial, as well as 3d simulations. The results of our simulations for 2d planar drops using NEOS model have indicated that IPA/Si configuration is the only unstable one among 4 liquid-solid configurations considered, again in agreement with the experiments. Next, we have performed the numerical simulations for 2d radial drops for IPA/Si configuration only, using both evaporation models. We have found spreading motion and ‘stretching’ of the contact line region for “lens” model, and receding motion for NEOS model, which is so rapid that it destabilizes the contact line region and leads to occurrence of a ‘ring’ of fluid which remains ahead of the contact as the drop recedes. In order to further examine these results, we have carried out the 3d simulations of volatile drops of IPA on Si solid using both evaporation models, and have found good agreement with our results for 2d radial drops. Finally, we have applied azimuthal perturbations to the contact line region for both evaporation models, in order to determine the stability. We have found that when “lens” model is used, the configuration is stable to all considered azimuthal perturbations. This behavior has been explained using an argument based on Marangoni forces, which (in the contact line region) act outward for “lens” model. Next, we have found that when NEOS model is used, the instability occurs for azimuthal perturbations of certain wavelengths – the ‘ring’ of liquid which forms ahead of the contact line becomes unstable and collapses into individual drops. We have noted the strong resemblance between this instability and the “octopi” seen in experiments. Finally, we have compared the wavelengths used for azimuthal perturbations for NEOS model with the LSA predictions for volatile films and found qualitative agreement.

Future Work

The fact that two commonly used evaporation models, such as “lens” and NEOS, produce results which are so qualitatively different is intriguing. In particular, the difference in temperature profiles at the liquid-gas interface for the two models, implies that the resulting Marangoni forces may be oppositely directed. For particular situations considered, we find that NEOS model is more appropriate for DIW, while “lens” model is more appropriate for IPA configurations. More elaborate experiments, involving measurement of the temperature at the liquid-gas interface, are therefore necessary, as they will provide an ultimate criterion for selection of appropriate evaporation model.

Next, our experimental results regarding instabilities which occur for IPA-DIW mixtures of varying IPA concentration (Chapter 5) provide an excellent motivation for future theoretical work: it is of interest to pursue the understanding of the transition of the instability types as the IPA concentration is increased. In order to achieve this, one may modify the mathematical model we have developed in order to include the ‘solutal’ Marangoni effects, which introduces the dependence of surface tension on the concentration of the more volatile component in the mixture. In particular, the surface tension becomes function of both temperature T and IPA concentration in the mixture Υ : $\sigma(T, \Upsilon) = \sigma_0 - \gamma(T - T_0) - \gamma_s(\Upsilon - \Upsilon_0)$, where $\gamma_s = -d\sigma/d\Upsilon$. We note that $\gamma_s > 0$, since σ decreases with IPA concentration in the mixture. Only few details concerning the inclusion of ‘solutal’ Marangoni effect into our mathematical model are described here. The parameter values which may be used correspond to a particular mixture of interest at time $t = 0$. The scale for IPA concentration in the mixture which one may employ follows the same logic as the temperature scale we have used so far: the difference between Υ and some reference concentration Υ_{ref} may be scaled against $\Delta\Upsilon = \Upsilon_0 - \Upsilon_{ref}$. This approach leads to ‘solutal’ Marangoni number M_s , which accompanies the (thermocapillary) Marangoni number M and is defined

as $M_s = \gamma_s \Delta \Upsilon d_0 / (2\rho\nu\kappa)$. The complexity of the model will be further increased since it would also be necessary to solve the problem for Υ in the liquid phase. This would involve a convection-diffusion equation for Υ , along with appropriate boundary conditions (no flux at the liquid-solid interface, and a relation between mass flux J and the IPA concentration flux at the liquid-gas interface). As we have done for temperature T , one may solve for Υ as a function of J , and hence, incorporate the additional term corresponding to the ‘solutal’ Marangoni forces into the governing equation (e.g. Eq. (2.36)) while maintaining the current framework (J is explicit). We expect an interesting outcome of this project, since our preliminary estimates indicate the possibility that the two Marangoni effects may operate in synergy for certain configurations/initial values of Υ , while competition between them is anticipated for other situations. We hope that this variation of regime will provide explanation for our experimental result.

In addition, the understanding of the phenomena of deposit formation for evaporative drops, and the manner in which it affects the contact line pinning is also of great interest. This field of research is particularly inviting, due to numerous applications for which this phenomena is essential, such as semi-conductor fabrication and the analysis of DNA/RNA arrays, among others. It is clear that the deposit patterns are consequences of Marangoni forces. Both experiments and theoretical modeling are required in order to achieve better understanding of the phenomena of deposit formation. We anticipate that the antecedent conclusions regarding which evaporation model is appropriate for a particular physical situation may be of critical importance for understanding of this phenomena.

Finally, one may also examine the mesoscopic structures which develop during the process of drying of highly volatile very thin films. Such films are used as resist films in lithographic applications and they develop both surface instabilities (striations and polygonal cells) and internal structuring. These instabilities are connected

to performance degradation, and hence, their understanding would be of significant practical importance.

REFERENCES

- [1] [Online]. Available: http://web.njit.edu/~nm44/octopi_experiments.html, April 23, 2008.
- [2] V. Ajaev, "Spreading of thin volatile liquid droplets on uniformly heated surfaces," *J. Fluid Mech.*, vol. 528, p. 279, 2005.
- [3] D. M. Anderson and S. H. Davis, "The spreading of volatile liquid droplets on heated surfaces," *Phys. Fluids*, vol. 7, p. 248, 1995.
- [4] G. I. Barenblatt, *Scaling, Self-similarity, and Intermediate Asymptotics*. New York: Cambridge University Press, 1996.
- [5] G. T. Barnes, "Insoluble monolayers and the evaporation coefficient for water," *J. Colloid Interface Sci.*, vol. 65, p. 5666, 1978.
- [6] R. Blossey, "Self-cleaning surfaces - virtual realities," *Nature Materials*, vol. 2, p. 301, 2003.
- [7] J. P. Burelbach, S. G. Bankoff, and S. H. Davis, "Nonlinear stability of evaporating/condensing liquid films," *J. Fluid Mech.*, vol. 195, p. 463, 1988.
- [8] M. Cachile, O. Benichou, and A. Cazabat, "Evaporating droplets of completely wetting liquids," *Langmuir*, vol. 18, p. 7985, 2002.
- [9] M. Cachile, O. Benichou, C. Poulard, and A. Cazabat, "Evaporating droplets," *Langmuir*, vol. 18, p. 8070, 2002.
- [10] P. Colinet, J. Legros, and M. Velarde, *Nonlinear dynamics of surface-tension-driven instabilities*. Berlin: Wiley-VCH, 2001.
- [11] S. David, K. Sefiane, and L. Tadrif, "Experimental investigation of the effect of thermal properties of the substrate in the wetting and evaporation of sessile drops," *Colloids Surf. A*, vol. 298, p. 108, 2007.
- [12] P. G. de Gennes, "Wetting: Statics and dynamics," *Rev. Mod. Phys.*, vol. 57, p. 827, 1985.
- [13] R. Deegan, "Pattern formation in drying drops," *Phys. Rev. E*, vol. 61, p. 475, 2000.
- [14] R. Deegan, O. Bakajin, T. Dupont, G. Huber, S. Nagel, and T. Witten, "Capillary flow as the cause of ring stains from dried liquid drops," *Nature*, vol. 389, p. 827, 1997.
- [15] R. Deegan, O. Bakajin, T. Dupont, G. Huber, S. Nagel, and T. Witten, "Contact line deposits in an evaporating drop," *Phys. Rev. E*, vol. 62, p. 756, 2000.

- [16] B. Deryagin, L. Leonov, S. Mogilat, and V. Borisova, "Dependence of water condensation coefficient on degree of interface coverage by cetyl alcohol monolayers," *Colloid J. USSR*, vol. 44, p. 775, 1982.
- [17] J. Diez and L. Kondic, "Computing three-dimensional thin film flows including contact lines," *J. Comp. Phys.*, vol. 183, p. 274, 2002.
- [18] J. Diez, L. Kondic, and A. L. Bertozzi, "Global models for moving contact lines," *Phys. Rev. E*, vol. 63, p. 011208, 2001.
- [19] M. Dondlinger, J. Margerit, and P. Dauby, "Weakly nonlinear study of marangoni instabilities in an evaporating liquid layer," *J. Colloid Interface Sci.*, vol. 283, p. 522, 2005.
- [20] B. Fischer, "Particle convection in an evaporating colloidal droplet," *Langmuir*, vol. 18, p. 60, 2002.
- [21] D. Gil, T. A. Brunner, C. Fonseca, N. Seong, B. Streefkerk, C. Wagner, and M. Stavenga, "Immersion lithography: New opportunities for semiconductor manufacturing," *J. Vac. Sci. Technol. B*, vol. 22, p. 3431, 2004.
- [22] F. Girard, M. Antoni, S. Faure, and A. Steinchen, "Evaporation and marangoni driven convection in small heated water droplets," *Langmuir*, vol. 22, p. 11085, 2006.
- [23] M. Gonuguntla and A. Sharma, "Polymer patterns in evaporating droplets on dissolving substrates," *Langmuir*, vol. 20, p. 3456, 2004.
- [24] Y. Gotkis, I. Ivanov, N. Murisic, and L. Kondic, "Dynamic structure formation at the fronts of volatile liquid drops," *Phys. Rev. Lett.*, vol. 97, p. 186101, 2006.
- [25] G. Guena, P. Allancon, and A. M. Cazabat, "Receding contact angle in the situation of complete wetting: Experimental check of a model used for evaporating droplets," *Colloids Surf. A*, vol. 300, p. 307, 2007.
- [26] G. Guena, C. Poulard, and A. M. Cazabat, "The leading edge of evaporating droplets," *J. Colloid Interface Sci.*, vol. 312, p. 164, 2006.
- [27] G. Guena, C. Poulard, and A. M. Cazabat, "Evaporating drops of alkane mixtures," *Colloids Surf. A*, vol. 298, p. 2, 2007.
- [28] G. Guena, C. Poulard, M. Voue, J. D. Coninck, and A. M. Cazabat, "Evaporation of sessile liquid droplets," *Colloids Surf. A*, vol. 291, p. 191, 2006.
- [29] B. Haut and P. Colinet, "Surface-tension-driven instabilities of a pure liquid layer evaporating into an inert gas," *J. Colloid Interface Sci.*, vol. 285, p. 296, 2005.
- [30] L. Hocking, "On contact angles in evaporating liquids," *Phys. Fluids*, vol. 7, p. 2950, 1995.

- [31] H. Hu and R. G. Larson, "Analysis of the effects of marangoni stresses on the microflow in an evaporating sessile droplet," *Langmuir*, vol. 21, p. 3972, 2005.
- [32] H. Hu and R. G. Larson, "Marangoni effect reverses coffee-ring deposition," *J. Phys. Chem. B*, vol. 110, p. 7090, 2006.
- [33] H. Hu and R. Larson, "Evaporation of a sessile droplet on a substrate," *J. Phys. Chem. B*, vol. 106, p. 1334, 2002.
- [34] H. Hu and R. Larson, "Analysis of the microfluid flow in an evaporating sessile droplet," *Langmuir*, vol. 21, p. 3963, 2005.
- [35] J. N. Israelachvili, *Intermolecular and surface forces*. New York: Academic Press, 1992.
- [36] J. D. Jackson, *Classical Electrodynamics*. New York: Wiley, 1962.
- [37] D. E. Kataoka and S. M. Troian, "A theoretical study of instabilities at the advancing front of thermally driven coating films," *J. Colloid Interface Sci.*, vol. 192, p. 350, 1997.
- [38] P. Kavehpour, B. Ovrzyn, and G. McKinley, "Evaporatively-driven marangoni instabilities of volatile liquid films spreading on thermally conductive substrates," *Colloids Surf. A*, vol. 206, p. 409, 2002.
- [39] E. Kennard, *Kinetic Theory of Gases with an Introduction to Statistical Mechanics*. New York and London: McGraw-Hill Book Company, Inc., 1938.
- [40] J. Kim, S. I. Ahn, J. H. Kim, and W. Zin, "Evaporation of water droplets on polymer surfaces," *Langmuir*, vol. 23, p. 6163, 2007.
- [41] I. Kliakhandler, S. Davis, and S. Bankoff, "The effect of heat conduction in the vapor on the dynamics of downflowing condensate," *Phys. Fluids*, vol. 14, p. 150, 2002.
- [42] L. Kondic, "Instability in the gravity driven flow of thin liquid films," *SIAM Review*, vol. 45, p. 95, 2003.
- [43] L. Kondic and J. Diez, "Flow of thin films on patterned surfaces: Controlling the instability," *Phys. Rev. E*, vol. 65, p. 045301, 2002.
- [44] L. Kondic and N. Murisic, "On modeling evaporation," *Proceedings of the 5th Conference on Applied Mathematics and Scientific Computing (ApplMath 07), Brijuni Islands, Croatia, July 9-13, 2007*, 2008.
- [45] D. Lide, Ed., *Handbook of Chemistry and Physics, 78th Edition*. New York: CRC Press, Inc., 1997.
- [46] C. A. Mack, "Charting the future (and remembering the past) of optical lithography simulation," *J. Vac. Sci. Tech.*, vol. 23, p. 2601, 2005.

- [47] R. Marek and J. Straub, “Analysis of the evaporation coefficient and the condensation coefficient of water,” *Int. J. Heat Mass Transfer*, vol. 44, p. 39, 2001.
- [48] J. Margerit, M. Dondlinger, and P. Dauby, “Improved 1.5-sided model for the weakly nonlinear study of bnard-marangoni instabilities in an evaporating liquid layer,” *J. Colloid Interface Sci.*, vol. 290, pp. 220–230, 2005.
- [49] O. Matar, R. Moffat, and K. Sefiane, “Interfacial instabilities in evaporating drops,” in *Program of the 60th Annual DFD Meeting*, ser. Bulletin of the American Physical Society, G. Sprouse, Ed., vol. 52. APS, 2007, p. 160.
- [50] O. K. Matar and S. M. Troian, “Growth of nonmodal transient structures during the spreading of surfactant coated films,” *Phys. Fluids*, vol. 10, p. 1234, 1998.
- [51] S. J. S. Morris, “Contact angles for evaporating liquids predicted and compared with existing experiments,” *J. Fluid Mech.*, vol. 432, p. 1, 2001.
- [52] F. Mugele and S. Herminghaus, “Electrostatic stabilization of fluid microstructures,” *Appl. Phys. Lett.*, vol. 81, p. 2303, 2002.
- [53] N. Murisic and L. Kondic, “How do drops evaporate?” *submitted to Phys. Rev. Lett.*, February 2008.
- [54] N. Murisic and L. Kondic, “Octopus-shaped instabilities of evaporating drops,” *Proceedings of the 6th International Congress on Industrial and Applied Mathematics (ICIAM 07), Zurich, Switzerland, July 16-20, 2007*, 2008.
- [55] N. Murisic, L. Kondic, and Y. Gotkis, “Curiously shaped instabilities at the fronts of volatile drops,” in *Gallery of Fluid Motion, 60th Annual DFD Meeting*. APS, November 2007.
- [56] A. Oron and S. Bankoff, “Dewetting of a heated surface by an evaporating liquid film under conjoining/disjoining pressures,” *J. Colloid Interface Sci.*, vol. 218, p. 152, 1999.
- [57] A. Oron, S. H. Davis, and S. G. Bankoff, “Long-scale evolution of thin liquid films,” *Rev. Mod. Phys.*, vol. 69, p. 931, 1997.
- [58] Y. O. Popov, “Evaporative deposition patterns: Spatial dimensions of the deposit,” *Phys. Rev. E*, vol. 71, p. 036313, 2005.
- [59] C. Poulard, O. Benichou, and A. Cazabat, “Freely receding evaporating droplets,” *Langmuir*, vol. 19, p. 8828, 2003.
- [60] C. Poulard and P. Damman, “Control of spreading and drying of a polymer solution from marangoni flows,” *Europhys. Lett.*, vol. 80, p. 64001, 2007.
- [61] C. Poulard, G. Guena, A. M. Cazabat, A. Boudaoud, and M. B. Amar, “Rescaling the dynamics of evaporating drops,” *Langmuir*, vol. 21, p. 8226, 2005.

- [62] J. Prasad, "Front-end wafer cleaning challenges," *Semicond. Int.*, vol. 27, p. 61, 2004.
- [63] C. Redon, F. Brochard-Wyart, and F. Rondelez, "Festoon instabilities of slightly volatile liquids during spreading," *J. Phys. II France*, vol. 2, p. 1671, 1992.
- [64] W. Ristenpart, P. Kim, C. Domingues, J. Wan, and H. Stone, "Influence of substrate conductivity on circulation reversal in evaporating drops," *Phys. Rev. Lett.*, vol. 99, p. 234502, 2007.
- [65] M. Rothschild, T. M. Bloomstein, R. R. Kunz, V. Liberman, M. Switkes, S. T. Palmacci, J. H. C. Sedlacek, D. Hardy, and D. Grenville, "Liquid immersion lithography: Why, how and when?" *J. Vac. Sci. Technol. B*, vol. 22, p. 2877, 2004.
- [66] S. Saritha and P. Neogi, "Wetting kinetics of a thin film evaporating in air," *Phys. Fluids*, vol. 19, p. 112104, 2007.
- [67] R. Schrage, *A Theoretical Study of Interphase Mass Transfer*. New York: Columbia University Press, 1953.
- [68] L. W. Schwartz, R. V. Roy, R. R. Eley, and S. Petrash, "Simulation of droplet motion on low-energy and heterogeneous surfaces," *J. Colloid Interface Sci.*, vol. 234, p. 363, 2001.
- [69] O. E. Shklyaev and E. Fried, "Stability of an evaporating thin film," *J. Fluid Mech.*, vol. 584, p. 157, 2007.
- [70] E. Sultan, A. Boudaoud, and M. B. Amar, "Evaporation of a thin film: Diffusion of the vapor and marangoni instabilities," *J. Fluid Mech.*, vol. 543, p. 183, 2005.
- [71] T. Witelski and M. Bowen, "ADI schemes for higher-order nonlinear diffusion equations," *Applied Numer. Math.*, vol. 45, p. 331, 2003.